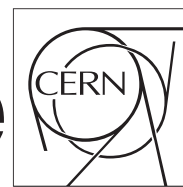


The Compact Muon Solenoid Experiment

# CMS Draft Note

Mailing address: CMS CERN, CH-1211 GENEVA 23, Switzerland



2021/02/25

Archive Hash: 1878afa

Archive Date: 2021/02/25

## Measurements of Higgs differential cross section and interpretations in $H \rightarrow ZZ \rightarrow 4\ell (\ell = e, \mu)$ channel

M. Bonanomi<sup>2</sup>, M.S. Chen<sup>1</sup>, Q.Y. Guo<sup>1,4</sup>, T. Javaid<sup>1,4</sup>, P. Milenovic<sup>5</sup>, V. Milosevic<sup>5</sup>, M. Ahmad<sup>7</sup>, C. Ochando<sup>2</sup>, G. Ortona<sup>2</sup>, R. Salerno<sup>2</sup>, R. Sharma<sup>1</sup>, T. Sculac<sup>3</sup>, and D. Sperka<sup>6</sup>

<sup>1</sup> IHEP, Beijing<sup>2</sup> Laboratoire Leprince-Ringuet<sup>3</sup> University of Split<sup>4</sup> Beihang University<sup>5</sup> University of Belgrade<sup>6</sup> Boston University<sup>7</sup> Tsinghua University

### Abstract

Properties of the Higgs boson are measured in the  $H \rightarrow ZZ \rightarrow 4\ell (\ell = e, \mu)$  decay channel. A data sample of proton-proton collisions at a center-of-mass energy of 13 TeV is used, corresponding to an integrated luminosity of  $137 \text{ fb}^{-1}$  recorded by the CMS detector at the LHC. The fiducial cross section is measured with respect to several observables sensitive to production and decay of Higgs where the observed results are compared with POWHEG, MADGRAPH5 and NNLOPS theory predictions. The possible interpretations of the results are reported.

This box is only visible in draft mode. Please make sure the values below make sense.

PDFAuthor:	Tahir Javaid
PDFTitle:	Measurements of Higgs differential cross section and interpretations in HZZ4 "(=e,") channel
PDFSubject:	CMS
PDFKeywords:	CMS, your topics

Please also verify that the abstract does not use any user defined symbols



## Acknowledgments

## Contents

1	Introduction . . . . .	2
2	EFT interpretations . . . . .	2
3	Datasets, simulation samples and theoretical predictions . . . . .	4
6	3.1 Triggers and Datasets . . . . .	4
7	3.2 Simulation samples and theoretical predictions . . . . .	7
8	4 Objects . . . . .	9
9	4.1 Electrons . . . . .	9
10	4.2 Muons . . . . .	9
11	4.3 Photons for FSR recovery . . . . .	10
12	4.4 Jets . . . . .	10
13	5 Signal Modelling . . . . .	15
14	6 Background Estimation . . . . .	16
15	6.1 Estimation of ZZ normalization from Data . . . . .	16
16	7 Analysis Strategy . . . . .	17
17	7.1 Event Selection . . . . .	17
18	7.2 Fiducial Volume Significance and Definition . . . . .	18
19	7.3 Binning strategy for differential observables . . . . .	19
20	7.4 Unfolding . . . . .	20
21	7.5 Acceptance and other correction factors . . . . .	20
22	7.6 Statistical Procedure . . . . .	21
23	7.7 Extraction of differential $H \rightarrow 4\ell$ cross section . . . . .	24
24	7.8 Interpretations . . . . .	28
25	8 Systematic uncertainties . . . . .	30
26	8.1 Systematic uncertainties treatment when combining the data sets . . . . .	31
27	9 Results . . . . .	36
28	9.1 Yields and distributions . . . . .	36
29	9.2 Differential Cross Sections measurement results . . . . .	40
30	9.3 Double differential cross section measurements . . . . .	44
31	9.4 Interpretations . . . . .	44
32	A Signal Shapes and Efficiencies . . . . .	45
33	A.1 Differential bins - Higgs boson transverse momentum . . . . .	45
34	A.2 Differential bins - rapidity of the Higgs boson . . . . .	63
35	A.3 Signal fits in differential bins - number of jets . . . . .	66

## 36 1 Introduction

37 The ATLAS and CMS collaborations first reported the discovery of a new boson in 2012 [1,  
 38 2] consistent with the standard model (SM) Higgs boson [3–8] based on proton-proton (pp)  
 39 collisions delivered by the CERN LHC at a center-of-mass energy of  $\sqrt{s} = 7\text{ TeV}$  in years 2011  
 40 and 8 TeV in 2012. Subsequent studies by CMS using the full LHC Run 1 data set in various  
 41 decay channels and production modes and combined measurements from ATLAS and CMS  
 42 [9–12] showed that the properties of the new boson are so far consistent with expectations for  
 43 the SM Higgs boson.

44 The  $H \rightarrow ZZ \rightarrow 4\ell$  decay channel ( $\ell = e, \mu$ ) has a large signal-to-background ratio due to the  
 45 complete reconstruction of the final state decay products and excellent lepton momentum res-  
 46 olution and is one of the most important channels for studies of the Higgs boson’s properties.  
 47 Measurements performed using this decay channel and the Run 1 data set include the deter-  
 48 mination of the mass and spin-parity of the new boson [13–15], its width [16, 17] and fiducial  
 49 cross sections [18], as well as tests for anomalous HVV couplings [15, 17].

50 In this document we present measurements of the differential fiducial cross sections for the  
 51 Higgs boson production in the  $H \rightarrow ZZ \rightarrow 4\ell$  decay channel at  $\sqrt{s} = 13\text{ TeV}$  using  $137\text{ fb}^{-1}$  of  
 52 pp collision data collected with the CMS experiment at the LHC in 2016, 2017 and 2018. Differ-  
 53 ential measurements for Higgs production variables have already been studied and published  
 54 under [19]. In this analysis, in addition, the full available dataset has been fully re-analyzed,  
 55 with several improvements:

- 56 • Analysis Ultra Legacy data.
- 57 • Revised measurement of lepton scale factors (Section 4.2.3)
- 58 • several additional (production and as well as decay) observables studied with opti-  
 59 mized binning.
- 60 • in addition to POWHEG and NNLOPS, MADGRAPH5\_AMC@NLO-FxFx is used as  
 61 additional theory prediction to for comparision of the observed results.
- 62 • Effective Field Theory (EFT) interpretations of differential measurements are also  
 63 presented.

## 64 2 EFT intereprations

65 Effective Field Theory (EFT) is an model independent way to parametrize the high enregy scale  
 66 effects in the enregy scale available to us. The general form of the lagrangian is:

$$\mathcal{L} = \mathcal{L}_{SM} + \mathcal{L}^5 + \mathcal{L}^6 + \mathcal{L}^7 + \dots, \quad \mathcal{L}^{(d)} = \sum_{i=1}^{n_d} \frac{C_i^{(d)}}{\Lambda^{d-4}} Q_i^{(d)} \quad \text{for } d > 4, \quad (1)$$

67 Where  $\Lambda$  is the New Physics (NP) enregy scale, the parameter  $C_i(d)$  are the Wilson Coefficients.

68 One of most promissing EFT model is the SMEFT [20, 21]. Since the operators  $Q_i^{(d)}$  are sur-  
 69 presssed by the power of cutoff scale  $\Lambda$ , so we will work with dimension-6 operators only.

70 Currently, we are trying to produce the Leading Order (LO) ggH process with additional jets  
 71 upto 2 jets. Like:

72 `import model SMEFTsim_A_general_MwScheme_UFO_v2`

```
73 #import model SMEFTsim_A_general_alphaScheme_UFO_v2
74 generate p p > h QED=1 NP<=1 @0
75 add process p p > h j QED=1 NP<=1 @1
76 add process p p > h j j QED=1 NP<=1 @2
```

77 Our plan with this is following:

- 78 • Generate SM from the SMEFT model and compare it with the NNNLOPS official  
79 samples (from HIG-19-001).
- 80 • Decide the set of parameter for which our analysis is sensitive.
- 81 • Validate the reweight method for our model.
- 82 • After finalizing previous step we will try to submit for official full CMSSW simula-  
83 tion.



### 84 3 Datasets, simulation samples and theoretical predictions

#### 85 3.1 Triggers and Datasets

86 This analysis uses a ultra legacy data sample recorded by the CMS experiment during 2016,  
 87 2017 and 2018, corresponding to  $137 \text{ fb}^{-1}$  of data.

88 The datasets used for 2016, 2017 and 2018 data taking are listed in Tables 1, 3, and 5, respec-  
 89 tively, along with the integrated luminosity. The analysis relies on four different primary  
 90 datasets (PDs), *DoubleMuon*, *MuEG*, *EGamma* (or *DoubleEG* and *SingleElectron* for 2016 and  
 91 2017), and *SingleMuon*, each of which combines a certain collections of HLT paths. To avoid  
 92 duplicate events from different primary datasets, events are taken:

- 93 • from EGamma if they pass the diEle or triEle or singleElectron triggers,
- 94 • from DoubleMuon if they pass the diMuon or triMuon triggers and fail the diEle  
   and triEle triggers,
- 95 • from MuEG if they pass the MuEle or MuDiEle or DiMuEle triggers and fail the  
   diEle, triEle, singleElectron, diMuon and triMuon triggers,
- 96 • from SingleMuon if they pass the singleMuon trigger and fail all the above triggers.

99 The HLT paths used for 2016, 2017 and 2018 collision data are listed in Tables 2, 4 and 6, respec-  
 100 tively.

Run-range	Dataset	Integrated luminosity
272007-275376	/DoubleMuon/Run2016C-21Feb2020_UL2016.HIPM-v1/MINIAOD /DoubleMuon/Run2016B-21Feb2020_ver1_UL2016.HIPM-v1/MINIAOD /MuonEG/Run2016B-21Feb2020_ver1_UL2016.HIPM-v1/MINIAOD /SingleElectron/Run2016B-21Feb2020_ver1_UL2016.HIPM-v1/MINIAOD /SingleMuon/Run2016B-21Feb2020_ver1_UL2016.HIPM-v1/MINIAOD	$5.892 \text{ fb}^{-1}$
275657-276283	/DoubleMuon/Run2016C-17Jul2018-v1/MINIAOD /DoubleEG/Run2016C-21Feb2020_UL2016.HIPM-v1/MINIAOD /MuonEG/Run2016C-21Feb2020_UL2016.HIPM-v1/MINIAOD /SingleElectron/Run2016C-21Feb2020_UL2016.HIPM-v1/MINIAOD /SingleMuon/Run2016C-21Feb2020_UL2016.HIPM-v1/MINIAOD	$2.646 \text{ fb}^{-1}$
276315-276811	/DoubleEG/Run2016D-21Feb2020_UL2016.HIPM-v1/MINIAOD /DoubleMuon/Run2016D-21Feb2020_UL2016.HIPM-v1/MINIAOD /MuonEG/Run2016D-21Feb2020_UL2016.HIPM-v1/MINIAOD /SingleElectron/Run2016D-21Feb2020_UL2016.HIPM-v1/MINIAOD /SingleMuon/Run2016D-21Feb2020_UL2016.HIPM-v1/MINIAOD	$4.353 \text{ fb}^{-1}$
276831-277420	/DoubleEG/Run2016E-21Feb2020_UL2016.HIPM-v1/MINIAOD /DoubleMuon/Run2016E-21Feb2020_UL2016.HIPM-v1/MINIAOD /MuonEG/Run2016E-21Feb2020_UL2016.HIPM-v1/MINIAOD /SingleElectron/Run2016E-21Feb2020_UL2016.HIPM-v1/MINIAOD /SingleMuon/Run2016E-21Feb2020_UL2016.HIPM-v1/MINIAOD	$4.117 \text{ fb}^{-1}$
277772-278808	/DoubleEG/Run2016F-21Feb2020_UL2016-v1/MINIAOD /DoubleMuon/Run2016F-21Feb2020_UL2016.HIPM-v1/MINIAOD /MuonEG/Run2016F-21Feb2020_UL2016-v1/MINIAOD /SingleElectron/Run2016F-21Feb2020_UL2016-v1/MINIAOD /SingleMuon/Run2016F-21Feb2020_UL2016-v1/MINIAOD	$3.186 \text{ fb}^{-1}$
278820-280385	/DoubleEG/Run2016G-21Feb2020_UL2016-v1/MINIAOD /DoubleMuon/Run2016G-21Feb2020_UL2016-v1/MINIAOD /MuonEG/Run2016G-21Feb2020_UL2016-v1/MINIAOD /SingleElectron/Run2016G-21Feb2020_UL2016-v1/MINIAOD /SingleMuon/Run2016G-21Feb2020_UL2016-v1/MINIAOD	$7.721 \text{ fb}^{-1}$
280919-284044	/DoubleEG/Run2016H-21Feb2020_UL2016-v1/MINIAOD /DoubleMuon/Run2016H-21Feb2020_UL2016-v1/MINIAOD /MuonEG/Run2016H-21Feb2020_UL2016-v1/MINIAOD /SingleElectron/Run2016H-21Feb2020_UL2016-v2/MINIAOD /SingleMuon/Run2016H-21Feb2020_UL2016-v1/MINIAOD	$8.857 \text{ fb}^{-1}$

Table 1: Datasets used in the 2016 analysis.

HLT path	prescale	primary dataset
HLT_Ele17_Ele12_CaloIdL_TrackIdL_IsoVL_DZ	1	DoubleEG
HLT_Ele23_Ele12_CaloIdL_TrackIdL_IsoVL_DZ	1	DoubleEG
HLT_DoubleEle33_CaloIdL_GsfTrkIdVL	1	DoubleEG
HLT_Ele16_Ele12_Ele8_CaloIdL_TrackIdL	1	DoubleEG
HLT_Mu17_TrkIsoVVL_Mu8_TrkIsoVVL	1	DoubleMuon
HLT_Mu17_TrkIsoVVL_TkMu8_TrkIsoVVL	1	DoubleMuon
HLT_TripleMu_12_10_5	1	DoubleMuon
HLT_Mu8_TrkIsoVVL_Ele17_CaloIdL_TrackIdL_IsoVL	1	MuonEG
HLT_Mu8_TrkIsoVVL_Ele23_CaloIdL_TrackIdL_IsoVL	1	MuonEG
HLT_Mu17_TrkIsoVVL_Ele12_CaloIdL_TrackIdL_IsoVL	1	MuonEG
HLT_Mu23_TrkIsoVVL_Ele12_CaloIdL_TrackIdL_IsoVL	1	MuonEG
HLT_Mu23_TrkIsoVVL_Ele8_CaloIdL_TrackIdL_IsoVL	1	MuonEG
HLT_Mu8_DiEle12_CaloIdL_TrackIdL	1	MuonEG
HLT_DiMu9_Ele9_CaloIdL_TrackIdL	1	MuonEG
HLT_Ele25_eta2p1_WPTight	1	SingleElectron
HLT_Ele27_WPTight	1	SingleElectron
HLT_Ele27_eta2p1_WPLoose_Gsf	1	SingleElectron
HLT_IsoMu20 OR HLT_IsoTkMu20	1	SingleMuon
HLT_IsoMu22 OR HLT_IsoTkMu22	1	SingleMuon

Table 2: Trigger paths used in 2016 collision data.

Run-range	Dataset	Integrated luminosity
297046-299329	/DoubleMuon/Run2017B-UL2017_MiniAODv2-v1/MINIAOD /DoubleEG/Run2017B-09Aug2019_UL2017-v1/MINIAOD /MuonEG/Run2017B-UL2017_MiniAODv2-v1/MINIAOD /SingleElectron/Run2017B-UL2017_MiniAODv2-v1/MINIAOD /SingleMuon/Run2017B-09Aug2019_UL2017-v1/MINIAOD	4.792 fb <sup>-1</sup>
299368-300676	/DoubleMuon/Run2017C-UL2017_MiniAODv2-v1/MINIAOD /DoubleEG/Run2017C-UL2017_MiniAODv2-v2/MINIAOD /MuonEG/Run2017C-UL2017_MiniAODv2-v1/MINIAOD /SingleElectron/Run2017C-UL2017_MiniAODv2-v1/MINIAOD /SingleMuon/Run2017C-09Aug2019_UL2017-v1/MINIAOD	9.755 fb <sup>-1</sup>
302030-303434	/DoubleMuon/Run2017D-UL2017_MiniAODv2-v1/MINIAOD /DoubleEG/Run2017D-UL2017_MiniAODv2-v1/MINIAOD /MuonEG/Run2017D-UL2017_MiniAODv2-v1/MINIAOD /SingleElectron/Run2017D-09Aug2019_UL2017-v1/MINIAOD /SingleMuon/Run2017D-09Aug2019_UL2017-v1/MINIAOD	4.319 fb <sup>-1</sup>
303824-304797	/DoubleMuon/Run2017E-09Aug2019_UL2017-v1/MINIAOD /DoubleEG/Run2017E-UL2017_MiniAODv2-v1/MINIAOD /MuonEG/Run2017E-UL2017_MiniAODv2-v1/MINIAOD /SingleElectron/Run2017E-UL2017_MiniAODv2-v1/MINIAOD /SingleMuon/Run2017E-09Aug2019_UL2017-v1/MINIAOD	9.424 fb <sup>-1</sup>
305040-306462	/DoubleMuon/Run2017F-UL2017_MiniAODv2-v1/MINIAOD /DoubleEG/Run2017F-09Aug2019_UL2017-v1/MINIAOD /MuonEG/Run2017F-UL2017_MiniAODv2-v1/MINIAOD /SingleElectron/Run2017F-UL2017_MiniAODv2-v1/MINIAOD /SingleMuon/Run2017F-09Aug2019_UL2017-v1/MINIAOD	13.50 fb <sup>-1</sup>
278820-280385	/DoubleMuon/Run2017G-09Aug2019_UL2017-v1/MINIAOD /DoubleEG/Run2017G??_MINIAOD /MuonEG/Run2017G??_MINIAOD /SingleElectron/Run2017G??_MINIAOD /SingleMuon/Run2017G?_MINIAOD	7.721 fb <sup>-1</sup>
281207-284068	/DoubleMuon/Run2017H-UL2017_MiniAODv2-v1/MINIAOD /DoubleEG/Run2017??_MINIAOD /MuonEG/Run2017H??_MINIAOD /SingleElectron/Run2017H??_MINIAOD /SingleMuon/Run2017H??_MINIAOD	8.857 fb <sup>-1</sup>

Table 3: Datasets used in the 2017 analysis.

HLT path	prescale	primary dataset
HLT_Ele23_Ele12_CaloIdL_TrackIdL_IsoVL_*	1	DoubleEG
HLT_DoubleEle33_CaloIdL_GsfTrkIdVL	1	DoubleEG
HLT_Ele16_Ele12_Ele8_CaloIdL_TrackIdL	1	DoubleEG
HLT_Mu17_TrkIsoVVL_Mu8_TrkIsoVVL_DZ_Mass3p8	1	DoubleMuon
HLT_Mu17_TrkIsoVVL_Mu8_TrkIsoVVL_DZ_Mass8	1	DoubleMuon
HLT_TripleMu_12_10_5	1	DoubleMuon
HLT_TripleMu_10_5_5_D2	1	DoubleMuon
HLT_Mu23_TrkIsoVVL_Ele12_CaloIdL_TrackIdL_IsoVL	1	MuonEG
HLT_Mu8_TrkIsoVVL_Ele23_CaloIdL_TrackIdL_IsoVL_DZ	1	MuonEG
HLT_Mu12_TrkIsoVVL_Ele23_CaloIdL_TrackIdL_IsoVL_DZ	1	MuonEG
HLT_Mu23_TrkIsoVVL_Ele12_CaloIdL_TrackIdL_IsoVL_DZ	1	MuonEG
HLT_DiMu9_Ele9_CaloIdL_TrackIdL_DZ	1	MuonEG
HLT_Mu8_DiEle12_CaloIdL_TrackIdL	1	MuonEG
HLT_Mu8_DiEle12_CaloIdL_TrackIdL_DZ	1	MuonEG
HLT_Ele35_WPTight_Gsf_v*	1	SingleElectron
HLT_Ele38_WPTight_Gsf_v*	1	SingleElectron
HLT_Ele40_WPTight_Gsf_v*	1	SingleElectron
HLT_IsoMu27	1	SingleMuon

Table 4: Trigger paths used in 2017 collision data.

Run-range	Dataset	Integrated luminosity
315252-316995	/DoubleMuon/Run2018A-UL2018_MiniAODv2-v1/MINIAOD /MuonEG/Run2018A-12Nov2019_UL2018_rsb-v1/MINIAOD /EGamma/Run2018A-12Nov2019_UL2018-v2/MINIAOD /SingleMuon/Run2018A-UL2018_MiniAODv2-v1/MINIAOD	X.XXX fb <sup>-1</sup>
317080-319310	/DoubleMuon/Run2018B-UL2018_MiniAODv2-v2/MINIAOD /MuonEG/Run2018B-12Nov2019_UL2018-v1/MINIAOD /EGamma/Run2018B-UL2018_MiniAODv2-v1/MINIAOD /SingleMuon/Run2018B-12Nov2019_UL2018-v2/MINIAOD	X.XXX fb <sup>-1</sup>
319337-320065	/DoubleMuon/Run2018C-12Nov2019_UL2018-v2/MINIAOD /MuonEG/Run2018C-12Nov2019_UL2018-v1/MINIAOD /EGamma/Run2018C-UL2018_MiniAODv2-v1/MINIAOD /SingleMuon/Run2018C-12Nov2019_UL2018-v2/MINIAOD	X.XXX fb <sup>-1</sup>
320673-325175	/DoubleMuon/Run2018D-UL2018_MiniAODv2-v1/MINIAOD /MuonEG/Run2018D-12Nov2019_UL2018_rsb-v1/MINIAOD /EGamma/Run2018D-UL2018_MiniAODv2-v1/MINIAOD /SingleMuon/Run2018D-12Nov2019_UL2018-v4/MINIAOD	X.XXX fb <sup>-1</sup>

Table 5: Datasets used in the 2018 analysis.

HLT path	prescale	primary dataset
HLT_Ele23_Ele12_CaloIdL_TrackIdL_IsoVL_v*	1	DoubleEG
HLT_DoubleEle25_CaloIdL_MW_v*	1	DoubleEG
HLT_Mu17_TrkIsoVVL_Mu8_TrkIsoVVL_DZ_Mass3p8_v*	1	DoubleMuon
HLT_Mu23_TrkIsoVVL_Ele12_CaloIdL_TrackIdL_IsoVL_v*	1	MuonEG
HLT_Mu8_TrkIsoVVL_Ele23_CaloIdL_TrackIdL_IsoVL_DZ_v*	1	MuonEG
HLT_Mu12_TrkIsoVVL_Ele23_CaloIdL_TrackIdL_IsoVL_DZ_v*	1	MuonEG
HLT_DiMu9_Ele9_CaloIdL_TrackIdL_DZ_v*	1	MuonEG
HLT_Ele32_WPTight_Gsf_v*	1	SingleElectron
HLT_IsoMu24_v*	1	SingleMuon

Table 6: Trigger paths used in 2018 collision data.

101 **3.1.1 Trigger Efficiency**

102 The efficiency in data of the combination of triggers used in the analysis with respect to the  
 103 offline reconstruction and selection is measured by considering  $4\ell$  events triggered by single  
 104 lepton triggers. Details on the procedures are described in  $H \rightarrow ZZ \rightarrow 4\ell$  ( $\ell = e, \mu$ ) analyses  
 105 common note [19].

106 A summary of the trigger efficiencies in MC truth, and in MC and data using the tag and probe  
 107 method are summarized in table 7. The trigger efficiency in simulation is found to be  $> 99\%$  in  
 108 each final state.

Final State	$gg \rightarrow H$ MC	$gg \rightarrow H$ MC (matching)	Data (matching)
$4e$	$0.991^{+.002}_{-.002}$	$0.948^{+.004}_{-.004}$	$0.982^{+.005}_{-.007}$
$4\mu$	$0.997^{+.001}_{-.001}$	$0.997^{+.001}_{-.001}$	$1.000^{+.000}_{-.001}$
$2e2\mu$	$0.995^{+.001}_{-.001}$	$0.964^{+.002}_{-.002}$	$0.983^{+.003}_{-.004}$

Table 7: Trigger efficiencies measured using  $4\ell$  events in 2018 data (TBU).

109 **3.2 Simulation samples and theoretical predictions**

110 **3.2.1 Signal Samples**

111 Descriptions of the SM Higgs boson production are obtained using the POWHEG V2 [22–24]  
 112 generator for the five main production modes: gluon fusion ( $gg \rightarrow H$ ) including quark mass  
 113 effects [25], vector boson fusion (VBF) [26], and associated production (WH, ZH and  $t\bar{t} H$  [27]).  
 114 The simulation of Higgs production through gluon fusion i.e.  $gg \rightarrow H$  production at next-  
 115 to-next-to-leading order (NNLO) is obtained by NNLOPS [28] and is used in the analysis as  
 116 reference theory predictions for observed differential cross section results. A dedicated studies  
 117 using MADGRAPH5\_AMC@NLO-FxFx generators with next-to-leading order (NLO) accuracy  
 118 is done for  $gg \rightarrow H$  production as additional theoretical predication for fiducial cross section  
 119 measurement. Details are described in Section 3.2.1. In the case of WH and ZH the MiNLO  
 120 HVJ extension of POWHEG is used [29]. The description of the decay of the Higgs boson to  
 121 four leptons is obtained using the JHUGEN generator [30]. In the case of WH, ZH and  $t\bar{t} H$ ,  
 122 the Higgs boson is allowed to decay to  $H \rightarrow ZZ \rightarrow 2\ell 2X$  such that 4-lepton events where two  
 123 leptons originate from the decay of associated Z, W bosons or top quarks are also taken into  
 124 account in the simulation. Showering of parton-level events is done using PYTHIA8.209, and in  
 125 all cases matching is performed by allowing QCD emissions at all energies in the shower and  
 126 vetoing them afterwards according to the POWHEG internal scale. All samples are generated  
 127 with the NNPDF 3.1 NLO parton distribution functions (PDFs) [31]. The list of signal samples  
 128 and their cross sections are shown in Table 8. For each year, corresponding simulation samples  
 129 are reweighted to match the pileup distribution in data for which details are described in [19].

130 **Simulation of Higgs production using MADGRAPH5**

131 To be updated.

132 **3.2.2 Background Samples**

133 Production of ZZ via quark-antiquark annihilation is generated at next-to-leading order (NLO)  
 134 using POWHEG V2 [32] and PYTHIA8, with the same settings as for the Higgs signal. As this  
 135 simulation covers a large range of ZZ invariant masses, dynamical QCD factorization and  
 136 renormalization scales have been chosen, equal to  $m_{ZZ}$ .

137 The  $gg \rightarrow ZZ$  process is simulated at leading order (LO) with MCFM [33, 34]. In order to match  
 138 the  $gg \rightarrow H \rightarrow ZZ$  transverse momentum spectra predicted by POWHEG at NLO, the showering

Process	Dataset Name	$\sigma \times BR(\times \epsilon_{\text{filter}})$
gg → H(124) → ZZ → 4ℓ	/GluGluHToZZTo4L_M124_13TeV_powheg2_JHUGenV7011_pythia8/[1]	12.18 fb
gg → H(125) → ZZ → 4ℓ	/GluGluHToZZTo4L_M125_13TeV_powheg2_JHUGenV7011_pythia8/[1]	12.18 fb
gg → H(126) → ZZ → 4ℓ	/GluGluHToZZTo4L_M126_13TeV_powheg2_JHUGenV7011_pythia8/[1]	12.18 fb
qq → Hqq → ZZqq → 4ℓqq	/VBF_HToZZTo4L_M125_13TeV_powheg2_JHUGenV709_pythia8/[1]	1.044 fb
qq → W <sup>+</sup> H → W <sup>+</sup> ZZ → 4ℓ + X	/WplusH_HToZZTo4L_M125_13TeV_powheg2-minlo-HWJ_JHUGenV7011_pythia8/[1]	0.232 fb
qq → W <sup>-</sup> H → W <sup>-</sup> ZZ → 4ℓ + X	/WminusH_HToZZTo4L_M125_13TeV_powheg2-minlo-HWJ_JHUGenV7011_pythia8/[1]	0.147 fb
qq → ZH → ZZZ → 4ℓ + X	/ZH_HToZZ_4LFitter_M125_13TeV_powheg2-minlo-HZJ_JHUGenV7011_pythia8/[1]	0.668 fb
gg → ttH → ttZZ → 4ℓ + X	/ttH_HToZZ_4LFitter_M125_13TeV_powheg_JHUGenV7011_pythia8/[1]	0.393 fb
gg → bbH → bbZZ → 4ℓ + X	/bbH_HToZZTo4L_M125_13TeV_JHUGenV7011_pythia8/[1]	0.135 fb
q̄q/qg → tHq → tqZZ → 4ℓ + X	/tqH_HToZZTo4L_M125_13TeV_JHUGenV7011_pythia8/[1]	0.0213 fb

[1] HIG-RunIISummer20UL18wmLHEGEN-000\*

Table 8: Signal Monte Carlo samples and cross sections.

Process	Dataset Name	$\sigma \cdot BR$
qq → ZZ → 4ℓ	/ZZTo4L_TuneCP5_13TeV_powheg_pythia8/	1.256 pb
qq → ZZ → 4ℓ	/ZZTo4L_TuneCP5_13TeV-amcatnloFXFX_pythia8/	1.212 pb
gg → ZZ → 4e	/GluGluToContinToZZTo4e_13TeV_MCFM701/	0.00159 pb
gg → ZZ → 4μ	/GluGluToContinToZZTo4mu_13TeV_MCFM701/	0.00159 pb
gg → ZZ → 2e2μ	/GluGluToContinToZZTo2e2mu_13TeV_MCFM701/	0.00319 pb
Z → ℓℓ + jets	/DYJetsToLL_M-50_TuneCUETP8M1_13TeV-amcatnloFXFX_pythia8/	6104 pb
Z → ℓℓ + jets	/DYJetsToLL_M-10to50_TuneCUETP8M1_13TeV-amcatnloFXFX_pythia8/	18610 pb
WZ → 3ℓν	/WZTo3LNu_TuneCUETP8M1_13TeV-powheg_pythia8/	4.430 pb
t̄t	/TTJets_TuneCUETP8M1_13TeV-amcatnloFXFX_pythia8/	815.96 pb
t̄t → 2ℓ2ν2b	/TTTo2L2Nu_13TeV-powheg/	87.31 pb
ZZZ	/ZZZ_TuneCUETP8M1_13TeV-amcatnlo_pythia8/	0.01398 pb
WZZ	/WZZ_TuneCUETP8M1_13TeV-amcatnlo_pythia8/	0.05565 pb
WWZ	/WWZ_TuneCUETP8M1_13TeV-amcatnlo_pythia8/	0.1651 pb
t̄t+ZZ	/TTZZ_TuneCUETP8M2T4_13TeV-madgraph_pythia8/	0.001572 pb
t̄t+WW	/TTWW_TuneCUETP8M2T4_3TeV-madgraph_pythia8/	0.007883 pb
t̄t+Z	/ttZJets_13TeV_madgraphMLM/	0.259 pb

Table 9: Background Monte Carlo samples and cross sections.

139 for MCFM samples is performed with different PYTHIA8 settings, allowing only emissions up  
 140 to the parton-level scale (“wimpy” shower).

141 Although not directly used to model data observations, additional MC samples of WZ, Drell-  
 142 Yan+jets, t̄t, and tribosons are generated using MADGRAPH5\_AMCATNLO [35] either inclu-  
 143 sively or merging several jet multiplicities, as detailed in the table. Table 9 summarizes the MC  
 144 simulation datasets used for this analysis.

## 4 Objects

This analysis follows the same object defintion as in [36] for each year. Detailed descriptcion on objection definitions and scale factors can be found in the corresponding analysis note [19]. Since this analysis is based on Ultra Legacy (UL) full Run 2 data, most of the objects related ingredients will be reevaluated with respect to [19].

The reconstruction of the SM Higgs boson in the decay chain  $H \rightarrow ZZ \rightarrow 4\ell$  requires very efficient lepton reconstruction and identification in order to be sensitive to a low mass Higgs, for which at least one of the leptons has a  $p_T$  within the range 5 - 15 GeV. In this kinematic region the need is for an optimal efficiency, while retaining the rate of misidentified leptons low enough. On the same time, to allow a precise measurement of the Higgs boson mass and together properties, which depend on the lepton kinematics, the analysis needs a precise momentum measurement. For both reasons, the analysis will make use of high statistics sources of prompt leptons to measure efficiency, mis-identification rate, and energy scale/resolution. Muon Efficiency measuremens using UL dataset are discribed as follows:

### 4.1 Electrons

#### 4.1.1 Electron Reconstruction and Identification

Referred to [19].

#### 4.1.2 Electron Energy Calibrations

Referred to [19].

#### 4.1.3 Electron Efficiency Measurements

Referred to [19].

### 4.2 Muons

#### 4.2.1 Muon Reconstruction and Identification

Referred to [19].

#### 4.2.2 Muon Energy Calibrations

Referred to [19].

#### 4.2.3 Muon Efficiency Measurements

Muon efficiencies are measured with the Tag and Probe (T&P) method performed on  $Z \rightarrow \mu\mu$  and  $J/\psi \rightarrow \mu\mu$  events in bins of  $p_T$  and  $\eta$ . More details on the methodology can be found in Ref. [37]. Measurements are extracted using 2016, 2017 and 2018 UL data. The Z sample is used to measure the muon reconstruction and identification efficiency at high  $p_T$ , and the efficiency of the isolation and impact parameter requirements at all  $p_T$ . The  $J/\psi$  sample is used to measure the reconstruction efficiency at low  $p_T$ , as it benefits from a better purity in that kinematic regime.

**Reconstruction and identification** Results for the muon reconstruction and identification efficiency for  $p_T > 20$  GeV have been derived by the Muon POG. However, results for low  $p_T$  muons were derived using  $J/\psi$  events, with the same definitions of probe and passing probes. Events are selected using `HLT_Mu8_v*` or `HLT_Mu17_v*` or `HLT_Mu20_v*` triggers. The probe

183 in this measurement are tracks reconstructed in the inner tracker, and the passing probes are  
 184 those that are also reconstructed as a global or tracker muon and passing the Muon POG Loose  
 185 muon identification.

186 Details on the procedure can be found in Ref. [38]. The efficiency and scale factors used for low  
 187  $p_T$  muons are the ones derived using single muon ultra-legacy dataset.

188 The efficiency in data and simulation is shown in Fig. 1.

189 **Impact parameter requirements** The measurement is performed using Z events. Events  
 190 are selected with `HLT_IsoMu20_v*` or `HLT_IsoMu22_v*` or `HLT_IsoMu22_eta2p1_v*` for  
 191 2016, `HLT_IsoMu27_v*` for 2017 and `HLT_IsoMu24_v*` for 2018 measurements. For this mea-  
 192 surement, the probe is a muon passing the POG Loose identification criteria, and it is consid-  
 193 ered a passing probe if it satisfies the SIP3D,  $dxy$ ,  $dz$  cuts of this analysis. The results are shown  
 194 in Fig. 2.

195 **Isolation requirements** The isolation efficiency is measured using events from the Z decay  
 196 for any  $p_T$ . The events are selected with the triggers as required for impact parameter require-  
 197 ments measurements as explained in previous paragraph. To fit the FSR contribution in the  
 198 low mass region, MC template convoluted with the Gaussian is used to better fit the dimuon  
 199 invariant mass.

200 The results are shown in Fig. 3.

201 **Tracking** The efficiency to reconstruct a muon track in the inner detector can be measured  
 202 using as probes tracks reconstructed in the muon system alone. However, since it comes out to  
 203 be 100%, it is no more recommended by muon POG.

204 **Overall results** The product of all the data to simulation scale factors for muon tracking,  
 205 reconstruction, identification, impact parameter and isolation requirements is shown in Fig. 4.  
 206 The systematic effects on measurements are estimated by <sup>1</sup>:

- 207 1. Varying the analytical signal and background shape models used to fit the dimuon in-  
 208 variant mass
- 209 2. Increasing and decreasing the number of bins in dimuon mass distribution
- 210 3. Increasing and decreasing the dimuon mass range
- 211 4. Relaxing and tightening a selection cut on tag muons

### 212 **4.3 Photons for FSR recovery**

213 Referred to [19].

### 214 **4.4 Jets**

215 Referred to [19].

---

<sup>1</sup>For low  $p_T$  measurements of reconstruction and identification only first three systematic sources are used as recommended by muon POG

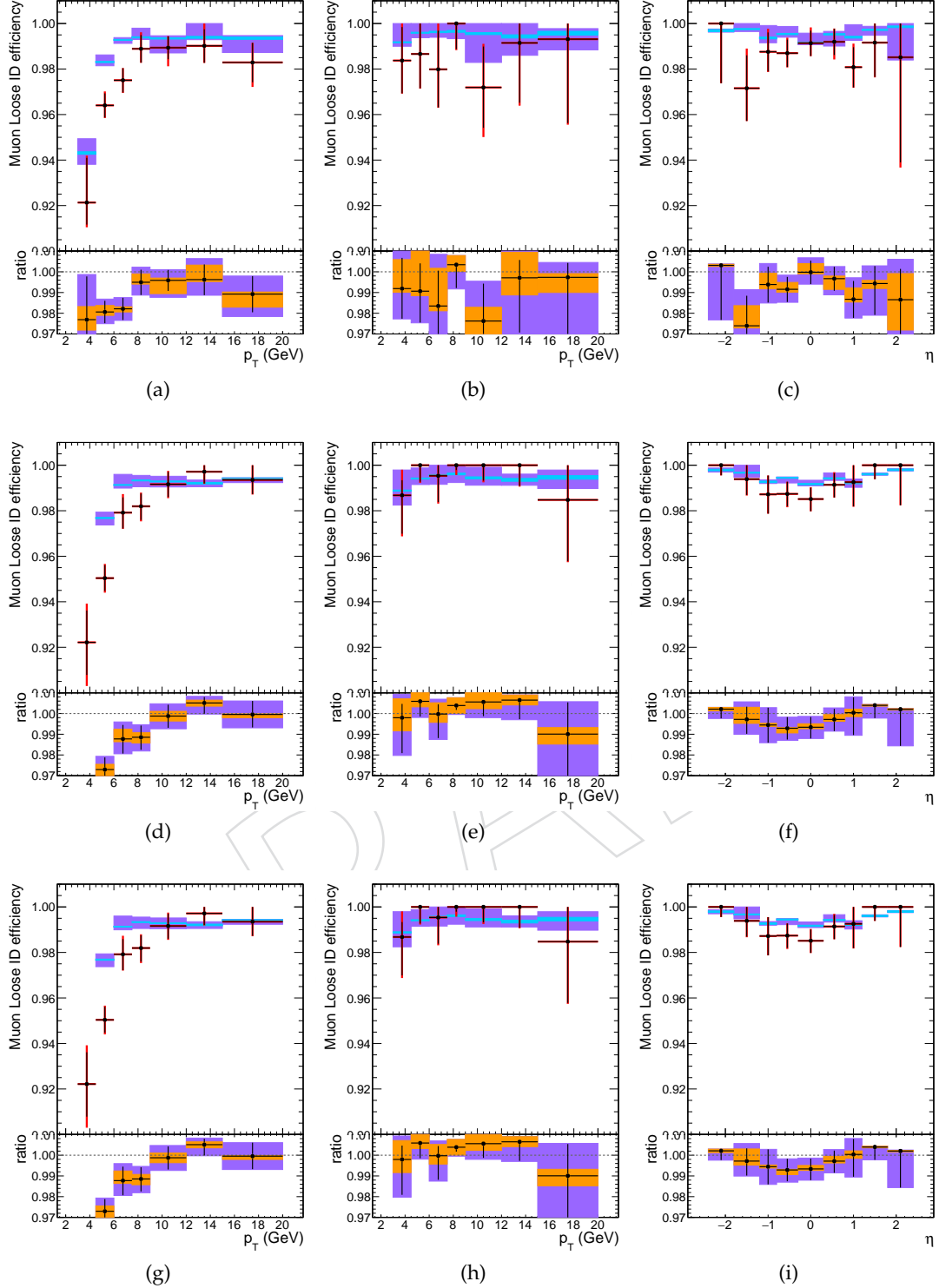


Figure 1: Muon reconstruction and identification efficiency at low  $p_T$ , measured with the tag&probe method on  $J/\psi$  events, as function of  $p_T$  in the barrel (left) and endcaps (center), and as function of  $\eta$  for  $p_T > 7\text{ GeV}$  (right), for 2016 (top), 2017 (middle) and 2018 (bottom). In the upper panel, the larger error bars include also the systematical uncertainties, while the smaller ones are purely statistical. In the lower panel showing the ratio of the two efficiencies, the black error bars are for the statistical uncertainty, the orange rectangles for the systematical uncertainty and the violet rectangles include both uncertainties.

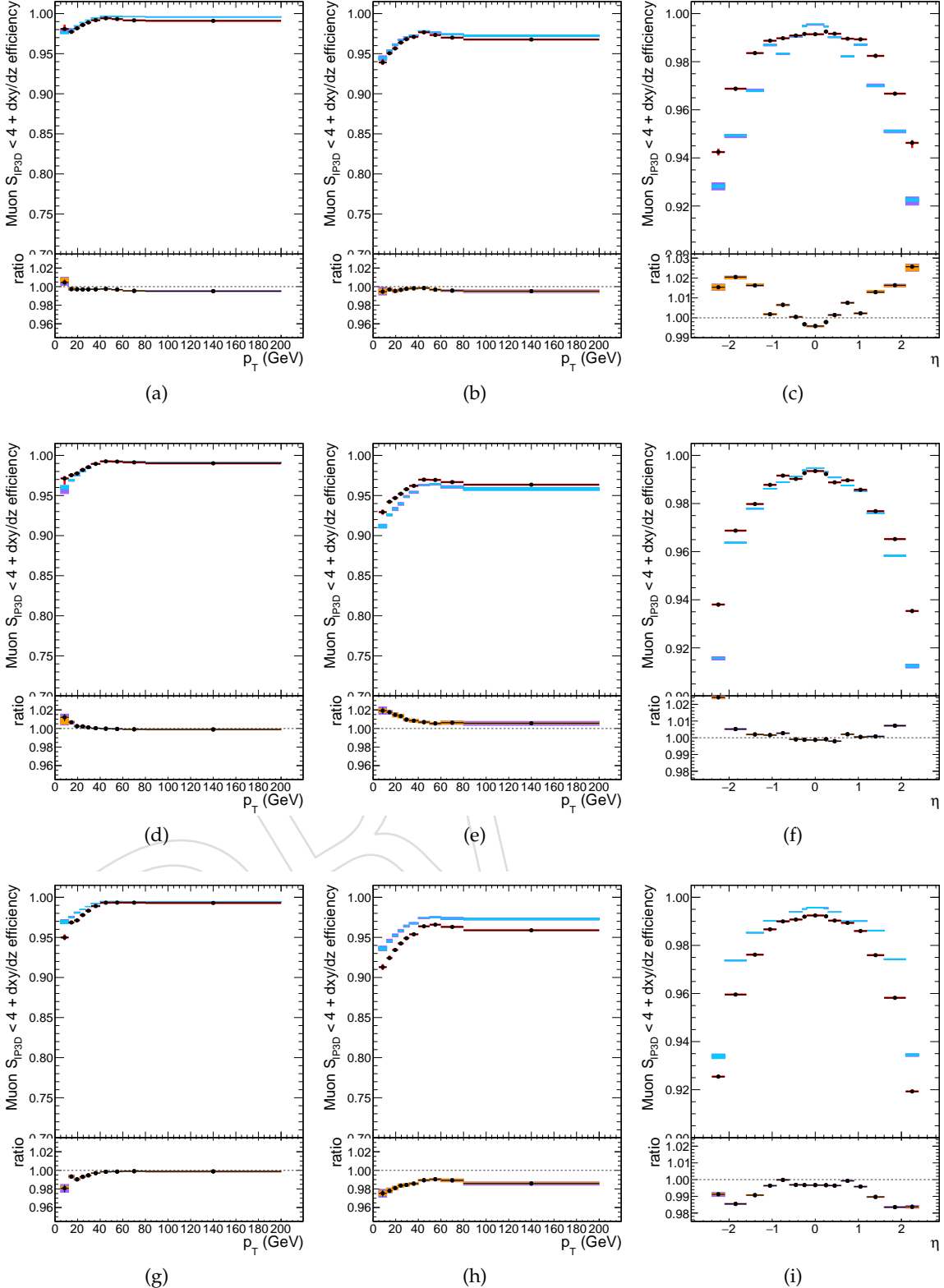


Figure 2: Efficiency of the muon impact parameter requirements, measured with the tag&probe method on  $Z$  events, as function of  $p_T$  in the barrel (left) and endcaps (center), and as function of  $\eta$  for  $p_T > 20$  GeV (right), for 2016 (top), 2017 (middle) and 2018 (bottom). In the upper panel, the larger error bars include also the systematical uncertainties, while the smaller ones are purely statistical. In the lower panel showing the ratio of the two efficiencies, the black error bars are for the statistical uncertainty, the orange rectangles for the systematical uncertainty and the violet rectangles include both uncertainties.

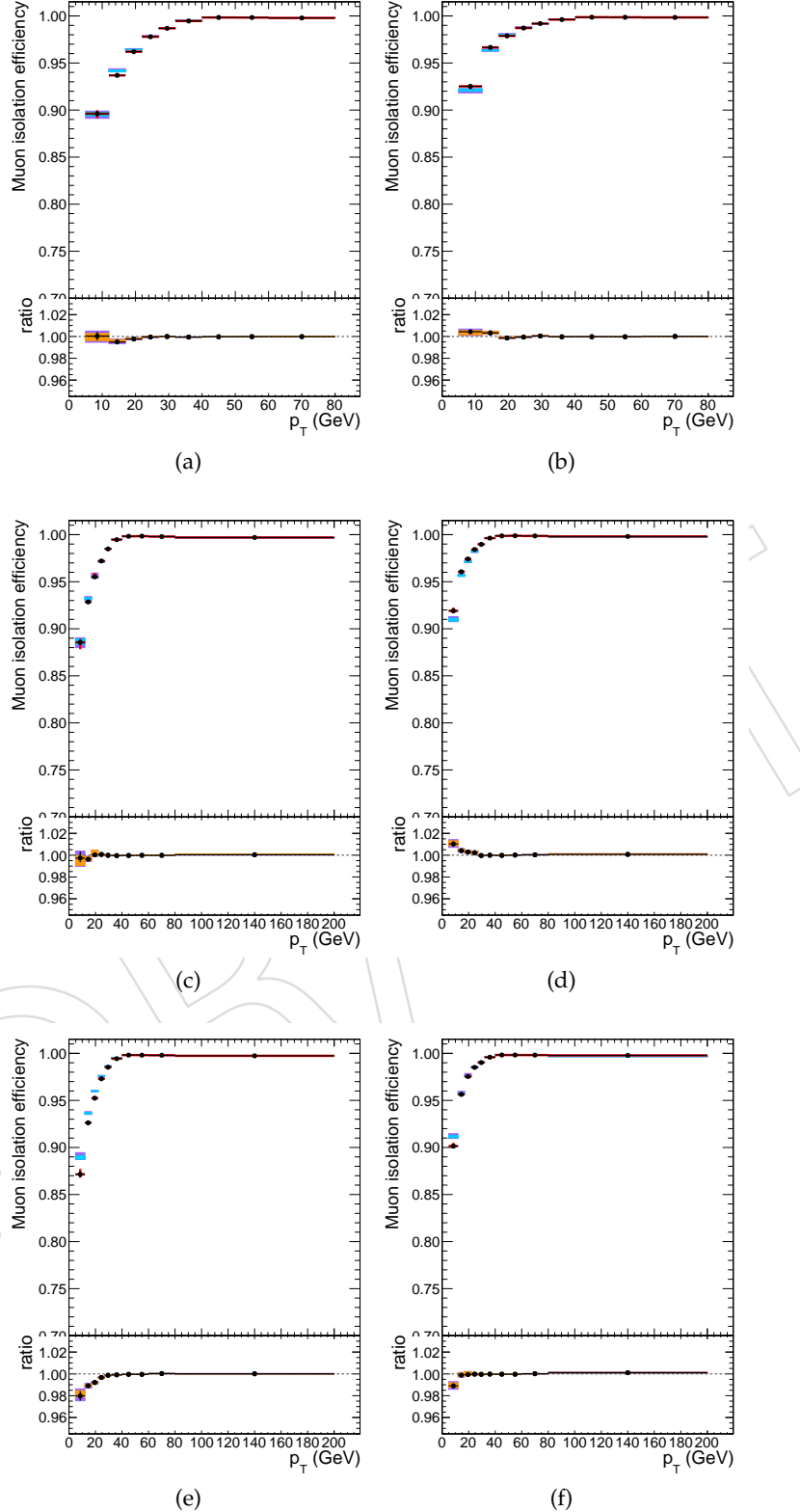


Figure 3: Efficiency of the muon isolation requirement, measured with the tag&probe method on  $Z$  events, as function of  $p_T$  in the barrel (left) and endcaps (right), for 2016 (top), 2017 (middle) and 2018 (bottom). In the upper panel, the larger error bars include also the systematical uncertainties, while the smaller ones are purely statistical. In the lower panel showing the ratio of the two efficiencies, the black error bars are for the statistical uncertainty, the orange rectangles for the systematical uncertainty and the violet rectangles include both uncertainties.

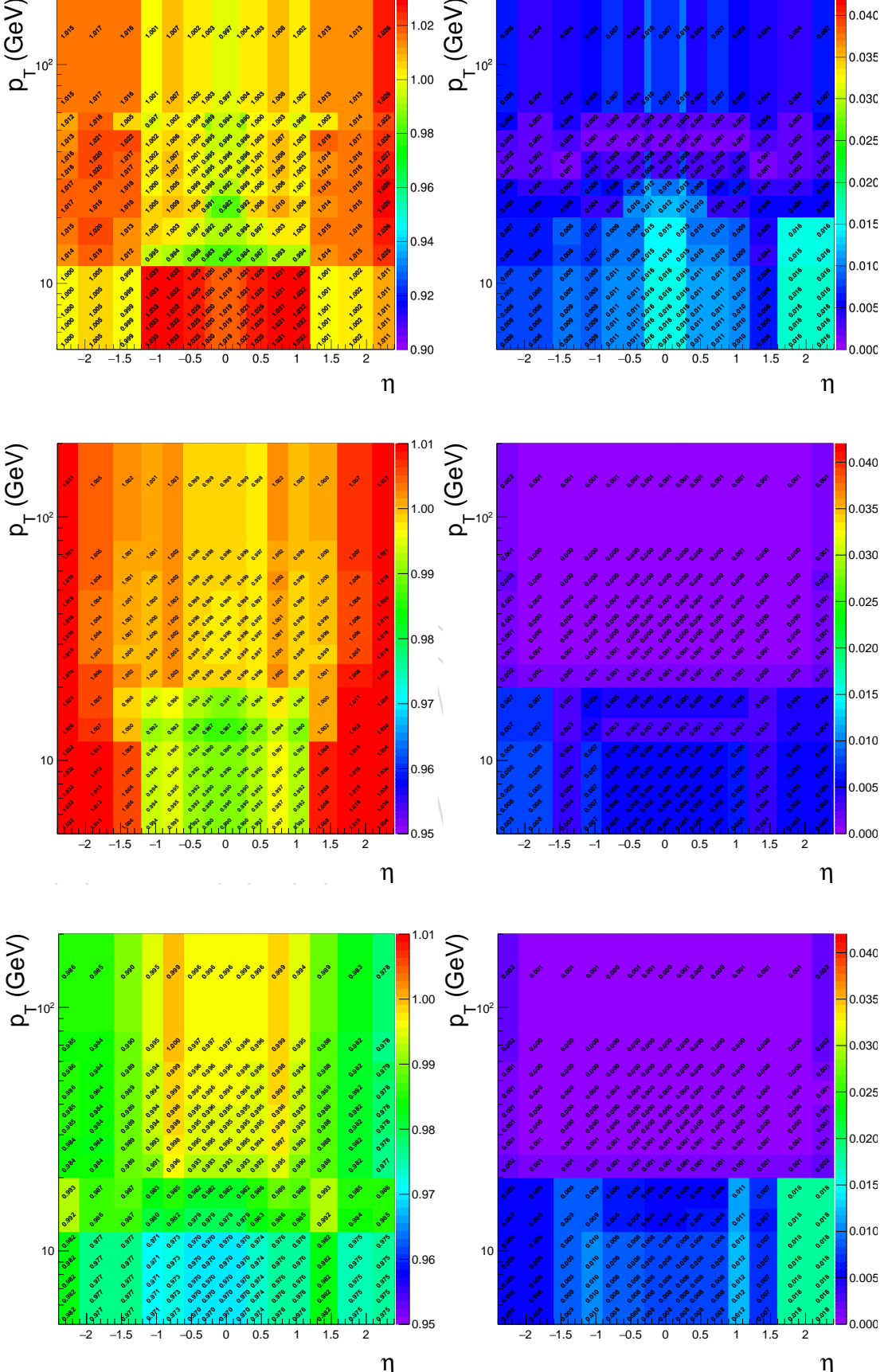


Figure 4: Left: Overall data to simulation scale factors for muons, as function of  $p_T$  and  $\eta$ . Right: Uncertainties on data to simulation scale factors for muons, as function of  $p_T$  and  $\eta$ . Results are shown for 2016 (top), 2017 (middle) and 2018 (bottom).

**216 5 Signal Modelling**

**217** Referred to AN [19]

DRAFT

## 218 6 Background Estimation

- 219 Details on the background processes and their modeling is discussed in detail in AN [19]. In  
 220 order to perform the differential measurements, the background four-lepton mass spectrum  
 221 need to be extracted at the reconstruction level for each bin of the considered observable. In  
 222 general, the background mass spectrum shape is not the same in every bin of the considered  
 223 observable because the background does not have a resonance structure. The mass spectrum  
 224 also can have non-negligible correlation with the observables.
- 225 In case of the irreducible backgrounds, the four-lepton mass spectra are extracted as the  $m_{4l}$   
 226 template shapes using Monte Carlo simulated events for each bin of the observable considered  
 227 for the measurement. Similarly, in case of the reducible backgrounds the templates are built  
 228 from the control regions in data.

In each differential bin of  $p_T(4\ell)$  fractions of background events are presented in the Table 10.

Table 10: Estimated fraction of background events in each bin of  $p_T(4\ell)$ , for each final state using 2018 samples.

Background	final state	0 – 15	15 – 30	30 – 45	45 – 80	80 – 120	120 – 200	200 – 13000
qqZZ	2e2μ	0.483668	0.239196	0.130151	0.105276	0.0266332	0.011809	0.00326633
qqZZ	4e	0.459665	0.234399	0.136986	0.114916	0.0388128	0.00989346	0.00532725
qqZZ	4μ	0.492632	0.241203	0.110977	0.109173	0.0297744	0.0129323	0.00330827
ggZZ	2e2μ	0.310446	0.309859	0.191901	0.168134	0.0187793	0.000880282	0.0
ggZZ	4e	0.3085	0.306332	0.19247	0.17433	0.0169994	0.00136908	0.0
ggZZ	4μ	0.321332	0.319311	0.194863	0.150987	0.0128703	0.000638196	0.0
Z+X (CR)	4l	0.0992521	0.211153	0.209307	0.305327	0.120303	0.0483797	0.00627828

229

### 230 6.1 Estimation of ZZ normalization from Data

- 231 In earlier analyses, both the shape and the normalization for  $q\bar{q} \rightarrow ZZ$  background were  
 232 measured from simulation. However, with full Run 2 statistics, we can benefit from enough  
 233 statistics to extend  $m_{4\ell}$  range to fit ZZ normalization from data, still taking shapes from sim-  
 234 ulation. This would help to improve the estimation and as well as reduction in uncertainties  
 235 because luminosity and other theoretical uncertainties no longer contribute to the normaliza-  
 236 tion. (studies in under validation)

## 237 7 Analysis Strategy

### 238 7.1 Event Selection

#### 239 7.1.1 Trigger Selection

240 The events are required to have fired the High-Level Trigger paths described in subsection 3.1.  
 241 Unlike in the Run I analysis, the trigger requirement does not depend on the selected final state:  
 242 it is always the OR of all HLT paths. The reason is in Run II we will be targeting associated  
 243 production modes that can come with additional leptons, thus improving trigger efficiency  
 244 further.

#### 245 7.1.2 Vertex Selection

246 The events are required to have at least one good primary vertex (PV) fulfilling the following  
 247 criteria: high number of degree of freedom ( $N_{PV} > 4$ ), collisions restricted along the  $z$ -axis  
 248 ( $z_{PV} < 24$  cm) and small radius of the PV ( $r_{PV} < 2$  cm).

#### 249 7.1.3 Z, ZZ and best ZZ Candidate Selection

250 The four-lepton candidates are built from what we call **selected leptons**, which are the tight  
 251 leptons that pass the  $SIP_{3D} < 4$  vertex constraint and the isolation cuts, where FSR photons  
 252 are subtracted as described in [19]. A lepton cross cleaning is applied by discarding electrons  
 253 which are within  $\Delta R < 0.05$  of selected muons.

254 The construction and selection of four-lepton candidates proceeds according to the following  
 255 sequence:

256 1. **Z candidates** are defined as pairs of selected leptons of opposite charge and matching  
 257 flavour ( $e^+e^-$ ,  $\mu^+\mu^-$ ) that satisfy  $12 < m_{\ell\ell(\gamma)} < 120$  GeV/ $c^2$ , where the Z candidate mass  
 258 includes the selected FSR photons if any.

259 2. **ZZ candidates** are defined as pairs of non-overlapping Z candidates. The Z candidate  
 260 with reconstructed mass  $m_{\ell\ell}$  closest to the nominal Z boson mass is denoted as  $Z_1$ , and  
 261 the second one is denoted as  $Z_2$ . ZZ candidates are required to satisfy the following list  
 262 of requirements:

- 263 • **Ghost removal** :  $\Delta R(\eta, \phi) > 0.02$  between each of the four leptons.
- 264 • **lepton  $p_T$** : Two of the four selected leptons should pass  $p_{T,i} > 20$  GeV/ $c$  and  
 $p_{T,j} > 10$  GeV/ $c$ . FSR photons are used.
- 266 • **QCD suppression**: all four opposite-sign pairs that can be built with the four  
 267 leptons (regardless of lepton flavor) must satisfy  $m_{\ell\ell} > 4$  GeV/ $c^2$ . Here, se-  
 268 lected FSR photons are not used in computing  $m_{\ell\ell}$ , since a QCD-induced low  
 269 mass dilepton (eg.  $J/\Psi$ ) may have photons nearby (e.g. from  $\pi_0$ ).
- 270 •  **$Z_1$  mass**:  $m_{Z_1} > 40$  GeV/ $c^2$
- 271 • **'smart cut'**: defining  $Z_a$  and  $Z_b$  as the mass-sorted alternative pairing Z candi-  
 272 dates ( $Z_a$  being the one closest to the nominal Z boson mass), require NOT( $|m_{Z_a} -$   
 $m_Z| < |m_{Z_1} - m_Z|$  AND  $m_{Z_b} < 12$ ). Selected FSR photons are included in  $m_Z$ 's  
 273 computations. This cut discards  $4\mu$  and  $4e$  candidates where the alternative  
 274 pairing looks like an on-shell Z + low-mass  $\ell^+\ell^-$ . (NB. In Run I, such a situa-  
 275 tion was avoided by choosing the best ZZ candidate before applying kinematic  
 276 cuts to it, most precisely before the  $m_{Z_2} > 12$  GeV/ $c^2$  cut. The present smart  
 277 cut allows to choose the best ZZ candidate after all kinematic cuts.)

279     • **four-lepton invariant mass:**  $m_{4\ell} > 70 \text{ GeV}/c^2$  (selected FSR photons are in-  
280       cluded).

281     3. Events containing at least one selected ZZ candidate form the **signal region**.

282     4. **Best ZZ candidate selection:** If more than one ZZ candidates survive the above selection,  
283       we choose the one with  $Z_1$  closest in mass to nominal Z boson mass and  $Z_2$  from the  
284       candidates whose lepton give higher  $p_T$  sum.

285 **7.2 Fiducial Volume Significance and Definition**

286 To minimize the model dependence, results are extracted in the fiducial volume that closely  
matches with the detector geometry as shown in Figure 5.



Figure 5: Fiducial phase definition among different models.

287

288 The differential cross subsections are measured in a fiducial region in order to reduce the ef-  
289 fects of model dependent acceptances. The fiducial selection mimics the reconstruction level  
290 selection, which is optimised to detect a low mass ( $m_H 125\text{GeV}$ ) Higgs boson decaying to 4 lep-  
291 tons through two Z bosons. Since in the standard model there are multiple production modes,  
292 the fiducial selection and measurement strategy are designed to be independent of how the

293 Higgs boson is produced. For this reason, the inclusion of isolation in the fiducial selection  
 294 is necessary in order to make the reconstruction efficiency with respect to the fiducial volume  
 295 independent of the number of jets.

296 The fiducial volume is defined to match closely the reconstruction level selection and is very  
 297 similar to the definition used in Refs. [18]. With respect to the Run 1 analysis, the leptons are  
 298 defined as “dressed” leptons rather than Born level leptons. Leptons are dressed by adding the  
 299 four-momenta of leptons within  $\Delta R < 0.3$  to the bare leptons. The fiducial lepton isolation cri-  
 300 teria is also updated to match the Run 2 reconstruction level isolation. Leptons are considered  
 301 isolated at generator level if the sum  $p_T$  of particles within a cone  $\Delta R < 0.3$  is less than 0.35. The  
 302 fiducial volume definition can be seen in Table 11. The fiducial volume acceptance for various  
 303 SM production modes can be seen in Table 16.

Table 11: Summary of requirements and selections used in the definition of the fiducial phase space for the  $H \rightarrow 4\ell$  cross subsection measurements.

Requirements for the $H \rightarrow 4\ell$ fiducial phase space	
Lepton kinematics and isolation	
leading lepton $p_T$	$p_T > 20 \text{ GeV}$
next-to-leading lepton $p_T$	$p_T > 10 \text{ GeV}$
additional electrons (muons) $p_T$	$p_T > 7(5) \text{ GeV}$
pseudorapidity of electrons (muons)	$ \eta  < 2.5(2.4)$
$p_T$ sum of all stable particles within $\Delta R < 0.3$ from lepton	less than $0.35 \cdot p_T$
Event topology	
existence of at least two SFOS lepton pairs, where leptons satisfy criteria above	
inv. mass of the $Z_1$ candidate	$40 \text{ GeV} < m(Z_1) < 120 \text{ GeV}$
inv. mass of the $Z_2$ candidate	$12 \text{ GeV} < m(Z_2) < 120 \text{ GeV}$
distance between selected four leptons	$\Delta R(\ell_i \ell_j) > 0.02$ for any $i \neq j$
inv. mass of any opposite sign lepton pair	$m(\ell^+ \ell^-) > 4 \text{ GeV}$
inv. mass of the selected four leptons	$105 \text{ GeV} < m_{4\ell} < 140 \text{ GeV}$
the selected four leptons must originate from the $H \rightarrow 4\ell$ decay	

### 304 7.3 Binning strategy for differential observables

Choice of bin boundaries and number of bins are two important aspects of differential measurements. With respect to the Run 1 analyses, we are benefitted from more statistic during Run 2 where data is recorded at  $137 \text{ fb}^{-1}$  with CMS detector. Sufficient statistics has helped to choose more fine binning for the observables than before. Bin boundaries are chosen in such a way that there is similar relative uncertainties on the expected cross section in the respective bins. Relative uncertainty ( $\Delta_{rel}$ ) is defined as:

$$\Delta_{rel}^i = \frac{d\sigma_{fid}^i}{\Delta_{tot}^i} \quad (2)$$

305 where  $d\sigma_{fid}^i$  and  $\Delta_{tot}^i$  are expected cross section and total uncertainty in bin  $i$  for a differential  
 306 observable.

307 Table 12 shows the current choice of bin boundaries of  $p_T(H)$  observables with details of ex-  
 308 pected cross section and relative uncertainties in the bins.

Table 12: Differential cross section results for the pT4l observable.

Bin range (GeV)	$d\sigma_{fid}$ (fb)	$\Delta_{tot}$ (% fb)	$\Delta_{rel}$ (%)	$\delta_{stat}$ (% fb)	$\delta_{syst}$ (% fb)
0 - 10	0.34	+0.11 -0.096	+33 -28	+0.1 -0.091	+0.048 -0.031
10 - 20	0.53	+0.13 -0.11	+25 -21	+0.12 -0.11	+0.056 -0.037
20 - 30	0.42	+0.11 -0.097	+27 -23	+0.1 -0.093	+0.044 -0.027
30 - 45	0.43	+0.11 -0.094	+25 -22	+0.1 -0.089	+0.044 -0.029
45 - 80	0.52	+0.11 -0.1	+22 -19	+0.1 -0.092	+0.05 -0.038
80 - 120	0.25	+0.073 -0.062	+29 -25	+0.069 -0.06	+0.024 -0.018
120 - 200	0.18	+0.057 -0.048	+31 -26	+0.055 -0.046	+0.016 -0.011
200 - 13000	0.082	+0.036 -0.028	+44 -34	+0.035 -0.028	+0.008 -0.004

## 309 7.4 Unfolding

310 The effects of imperfect detector resolution can in general have an non-negligible impact on  
 311 the shape of the distribution of the measured observables. For this reason, in case of the dif-  
 312 ferential cross sections measurements, a procedure to correct for the detection efficiencies and  
 313 resolution effects is applied. Throughout this document, this procedure will be referred to as  
 314 the unfolding procedure, and the unfolded differential distributions will be referred to as dis-  
 315 tributions at the fiducial level. Currently adopted procedure is “bin-by-bin unfolding”. This  
 316 procedure for the unfolding of the detector effects from the observed distributions is the same  
 317 as in Refs. [18] and [39]. The finite efficiencies and resolution effects are encoded in a detec-  
 318 tor response matrix which describes how events migrate from a given observable bin at the  
 319 fiducial level to a given bin at the reconstruction level. This matrix is diagonally dominant,  
 320 with sizeable off-diagonal elements for observables involving jets. It is aimed we would also  
 321 perform matrix inversion method as a validation tool for preceding method.

322 Examples of the efficiency matrices for gluon fusion and VBF production can be seen in Fig. 6.  
 323 The matrices for the  $p_{TH}$  and  $N(jets)$  observables are shown.

## 324 7.5 Acceptance and other correction factors

325 In this section the acceptance and other correction factors while measuring the cross sections  
 326 are discussed in details.

### 327 7.5.1 Acceptance

328 Ratio of the total number of events passing the fiducial level selectons  $N_{fid.}$  to the total number  
 329 of the generated events  $N_{gen.}$  are is called acceptance as given in Equation 3.

$$A = \frac{N_{fid.}}{N_{gen.}} \quad (3)$$

### 330 7.5.2 Other correction factors

331 Measurement strategy and definition of the fiducial volume is optimized to:

- 332 • detect a low mass Higgs ( $m_H=125.38$  GeV) boson decaying to 4 leptons through a  
 333 pair of Z bosons
- 334 • keep the measurements independent of how the Higgs boson is produced.

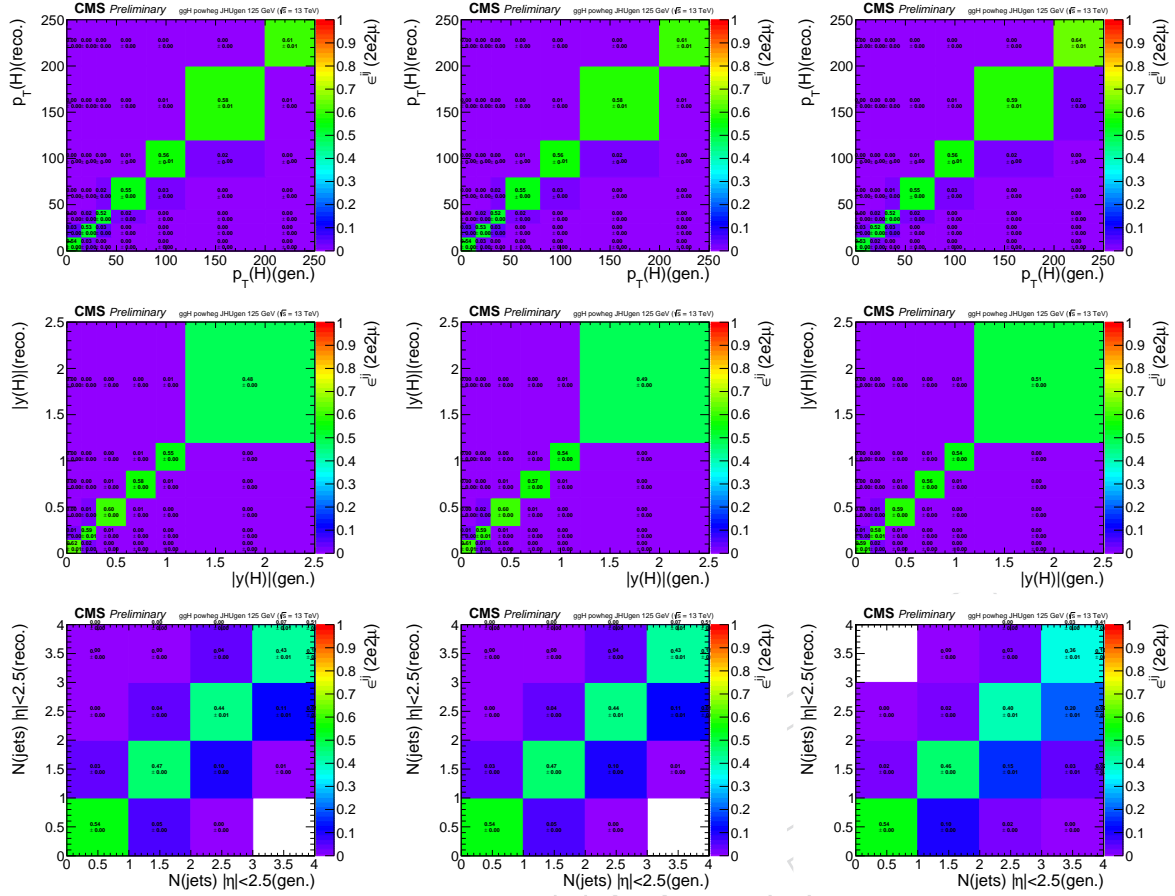


Figure 6: Efficiency matrices for the  $p_{\text{TH}}$  (top) and  $yH$  (middle) and  $N(\text{jets})$  (bottom) observables for gluon fusion production modes in the  $2e2\mu$  final state in 2016 (left) 2017 (middle) and 2018 (right) (TBU).

For reconstruction efficiency to be independent of fiducial phase space, it is necessary to include isolation in the definition of fiducial phase space.

In case of associated production of Higgs with vector bosons where the bosons can decay leptonically, there is possibility that Higgs is reconstructed from wrong combination of leptons. This makes it necessary to consider such “wrong combination” events as a background in order to keep complete information from unbinned simultaneous fit of signal and background parameterizations to four-lepton invariant mass.

Also, signal events which pass the fiducial level selections but fail the reconstruction are accounted in the fiducial efficiency ( $\epsilon$ ) and the events which pass the reconstruction but fail the fiducial selections are referred to as “nonfiducial signal” events ( $f_{\text{nonfid}}$ ) and are treated as a background as illustrated in Figure 7.

The summary of acceptance and other factors for full Run 2 periods are given Table. 16.

## 7.6 Statistical Procedure

We measure differential fiducial cross subsection for  $pp \rightarrow H \rightarrow 4\ell$  by performing a maximum likelihood fit of the signal and background parameterisations to the observed  $4\ell$  mass distribution,  $N_{\text{obs}}(m_{4\ell})$ , and the fiducial cross subsection ( $\sigma_{\text{fid}}$ ) is directly extracted from the fit. The systematic uncertainties are included in the form of nuisance parameters and are effectively



Figure 7: Fiducial efficiency( $\epsilon$ ) and nonfiducial( $f_{nonfid}$ ) signal definition.

Table 13: Summary of different Standard Model signal models (2016).

Signal process	$\mathcal{A}_{fid}$	$\epsilon$	$f_{nonfid}$	$(1 + f_{nonfid})\epsilon$
Individual Higgs boson production modes				
gg $\rightarrow$ H (POWHEG) 125 GeV	$0.397 \pm 0.001$	$0.604 \pm 0.001$	$0.051 \pm 0.001$	$0.635 \pm 0.001$
VBF 125 GeV	$0.446 \pm 0.001$	$0.618 \pm 0.002$	$0.039 \pm 0.001$	$0.642 \pm 0.002$
WH 125 GeV	$0.328 \pm 0.001$	$0.593 \pm 0.002$	$0.077 \pm 0.001$	$0.638 \pm 0.002$
ZH 125 GeV	$0.340 \pm 0.002$	$0.608 \pm 0.003$	$0.077 \pm 0.002$	$0.655 \pm 0.004$
ttH 125 GeV	$0.312 \pm 0.002$	$0.585 \pm 0.003$	$0.169 \pm 0.004$	$0.684 \pm 0.004$

352 integrated out in the fit procedure. The results are obtained using an asymptotic approach [40]  
 353 with a test statistic based on the profile likelihood ratio [41]. Following the models for signal  
 354 and background contributions described above, the number of expected events in each final

Table 14: Summary of different Standard Model signal models (2017).

Signal process	$\mathcal{A}_{\text{fid}}$	$\epsilon$	$f_{\text{nonfid}}$	$(1 + f_{\text{nonfid}})\epsilon$
Individual Higgs boson production modes				
gg $\rightarrow$ H (POWHEG) 125 GeV	$0.403 \pm 0.001$	$0.593 \pm 0.001$	$0.056 \pm 0.001$	$0.626 \pm 0.001$
VBF 125 GeV	$0.445 \pm 0.001$	$0.609 \pm 0.001$	$0.044 \pm 0.001$	$0.636 \pm 0.001$
WH 125 GeV	$0.329 \pm 0.001$	$0.583 \pm 0.002$	$0.081 \pm 0.001$	$0.631 \pm 0.002$
ZH 125 GeV	$0.341 \pm 0.002$	$0.594 \pm 0.003$	$0.084 \pm 0.002$	$0.644 \pm 0.004$
ttH 125 GeV	$0.318 \pm 0.003$	$0.589 \pm 0.006$	$0.187 \pm 0.007$	$0.699 \pm 0.008$

Table 15: Summary of different Standard Model signal models (2018).

Signal process	$\mathcal{A}_{\text{fid}}$	$\epsilon$	$f_{\text{nonfid}}$	$(1 + f_{\text{nonfid}})\epsilon$
Individual Higgs boson production modes				
gg $\rightarrow$ H (POWHEG) 125 GeV	$0.403 \pm 0.001$	$0.599 \pm 0.001$	$0.055 \pm 0.001$	$0.632 \pm 0.001$
VBF 125 GeV	$0.443 \pm 0.001$	$0.617 \pm 0.002$	$0.043 \pm 0.001$	$0.644 \pm 0.002$
WH 125 GeV	$0.330 \pm 0.001$	$0.625 \pm 0.002$	$0.075 \pm 0.001$	$0.672 \pm 0.002$
ZH 125 GeV	$0.339 \pm 0.002$	$0.629 \pm 0.003$	$0.083 \pm 0.002$	$0.681 \pm 0.004$
ttH 125 GeV	$0.314 \pm 0.002$	$0.589 \pm 0.003$	$0.184 \pm 0.004$	$0.698 \pm 0.004$

Table 16: Summary of different Standard Model signal models.(Full Run 2)

Signal process	$\mathcal{A}_{\text{fid}}$	$\epsilon$	$f_{\text{nonfid}}$	$(1 + f_{\text{nonfid}})\epsilon$
Individual Higgs boson production modes				
gg $\rightarrow$ H (POWHEG) 125 GeV	$0.402 \pm 0.001$	$0.598 \pm 0.002$	$0.054 \pm 0.001$	$0.631 \pm 0.002$
VBF 125 GeV	$0.445 \pm 0.002$	$0.615 \pm 0.002$	$0.043 \pm 0.001$	$0.641 \pm 0.003$
WH 125 GeV	$0.329 \pm 0.002$	$0.604 \pm 0.003$	$0.078 \pm 0.002$	$0.651 \pm 0.004$
ZH 125 GeV	$0.340 \pm 0.003$	$0.613 \pm 0.005$	$0.082 \pm 0.004$	$0.663 \pm 0.006$
ttH 125 GeV	$0.315 \pm 0.004$	$0.588 \pm 0.007$	$0.181 \pm 0.009$	$0.694 \pm 0.010$

355 state  $f$  and in each bin  $i$  of a considered observable is expressed as a function of  $m_{4\ell}$  given by:

$$\begin{aligned}
 N_{\text{obs}}^{f,i}(m_{4\ell}) &= N_{\text{fid}}^{f,i}(m_{4\ell}) + N_{\text{nonfid}}^{f,i}(m_{4\ell}) + N_{\text{nonres}}^{f,i}(m_{4\ell}) + N_{\text{bkg}}^{f,i}(m_{4\ell}) \\
 &= \epsilon_{i,j}^f \cdot (1 + f_{\text{nonfid}}^{f,i}) \cdot \sigma_{\text{fid}}^{f,j} \cdot \mathcal{L} \cdot \mathcal{P}_{\text{res}}(m_{4\ell}) \\
 &\quad + N_{\text{nonres}}^{f,i} \cdot \mathcal{P}_{\text{nonres}}(m_{4\ell}) + N_{\text{bkg}}^{f,i} \cdot \mathcal{P}_{\text{bkg}}(m_{4\ell}),
 \end{aligned} \tag{4}$$

356 The parameter  $\sigma_{\text{fid}}^{f,j}$  is the signal cross subsection in bin  $j$  of the fiducial phase space, and it is the  
357 parameter extracted from the measurement.

358 The shape of the resonant signal contribution,  $\mathcal{P}_{\text{res}}(m_{4\ell})$ , is described by a double-sided Crys-  
359 tal Ball function, as described in previous sections, whose normalisation is proportional to  
360 the fiducial cross subsection. The shape of the non-resonant signal contribution,  $\mathcal{P}_{\text{nonres}}(m_{4\ell})$ ,  
361 which arises from WH, ZH, and ttH production where one of the leptons from the Higgs bo-  
362 son decay is lost or not selected, is empirically modelled by a Landau distribution whose shape  
363 parameters are constrained in the fit to be within a range determined from simulation. This  
364 contribution is treated as a background and hereafter we will refer to this contribution as the  
365 “non-resonant signal” contribution.

366 The  $\epsilon_{i,j}^f$  represents the detector response matrix that maps the number of expected events in  
367 a given observable bin  $j$  at the fiducial level to the number of expected events in the bin  $i$  at

368 the reconstruction level. The  $f_{\text{nonfid}}^i$  fraction describes the ratio of the non-fiducial and fiducial  
369 signal contribution in bin  $i$  at the reconstruction level. The efficiency is measured using signal  
370 simulation samples and corrected for residual differences between data and simulation. In the  
371 case of the integrated fiducial cross subsection measurement the efficiencies reudce to a single  
372 values.

373 An additional resonant contribution arises from events which are reconstructed but which do  
374 not originate from the fiducial phase space. These events are due to detector effects which  
375 cause differences between the quantities used for the fiducial phase space definition and the  
376 analogous quantities are the reconstruction level. This contribution is treated as background  
377 and is referred to as the “non-fiducial signal” contribution. The shape of these events is verified  
378 using simulation to be identical to the shape of the fiducial signal and its normalisation is fixed  
379 to be a fraction of the fiducial signal component. The value of this fraction, which we denote  
380 by  $f_{\text{nonfid}}$ , which has been determined from simulation for each of the studied signal models.

381 The variation between different models of the factor in the final column of Table 16,  $(1 +$   
382  $f_{\text{nonfid}})\epsilon$ , is directly related to the model dependence of the measurement. The model depen-  
383 dence is defined as the variation of the factor  $(1 + f_{\text{nonfid}})\epsilon$  when the relative fraction of each  
384 the production modes are varied within there experimental constraints.

## 385 **7.7 Extraction of differential $H \rightarrow 4\ell$ cross section**

### 386 **7.7.1 Considered observables**

387 The differential fiducial cross sections are presented as a function of several kinematic observ-  
388 ables which are sensitive to the Higgs-boson production mechanisms. Examples are rapidity  
389 and transverse momentum of the four-lepton system, associated jet multiplicity and transverse  
390 momentum of the leading jet  $p_T(H)$  or  $p_T(4\ell)$ ,  $|y(H)|$  or  $|y(4\ell)|$ ,  $N(\text{jets})$ , and  $p_T(\text{jet})$ . These  
391 measurements are important to test the Standard Model predictions in the Higgs sector and  
392 can be used to constrain phase spaces of many theories beyond the Standard Model. In addition,  
393 several other observables related to decay of Higgs boson are also studied. These include  
394  $m_{Z_1}$ ,  $m_{Z_2}$ ,  $\phi$ ,  $\cos\theta^*$  and several other observables which are sensitive to spin and CP or Higgs  
395 bosons.

### 396 **7.7.2 Choice of bin boundaries**

397 For each kinematic or differential observable, selection procedure of the binning boundaries  
398 has been optimized in order to have a similar expected measured cross-section for every bin.  
399 Relative uncertainties for  $p_T$  of Higgs observables are given in Table. 17.

### 400 **7.7.3 Applying the Statistical Procedure**

401 The fiducial differential cross section is extracted in the bins of kinematic observables at the  
402 fiducial level following the procedure outlined in previous. For signal yields, mass spectrum  
403 of signal is built in each cell of the response matrix using a Double Crytal Ball (DCB) function,  
404 similar to what was done in Ref. [? ]. In practice, the same parameters of the CB function are  
405 used in each cell and the systematic uncertainties assigned on the energy scale and resolution  
406 generally cover discrepancy of signal mass spectrum among each cell.

407 Examples of the fitted signal line shapes for differential bins of  $p_T(H)$  from gg $\rightarrow H$  (POWHEG  
408 + JHUGEN 125 GeV 2018 sample) in the individual final states are shown in Figure 30, and  
409 examples of the efficiency matrices for  $p_T(H)$  for the  $2e2\mu$  final state are shown in Fig 9. Many  
410 more examples can be seen in Appendix A.

Table 17: Differential cross section results for the  $p_T(H)$  observable.

Bin range (GeV)	$d\sigma_{fid}$ (fb)	$\Delta_{tot}$ (% fb)	$\Delta_{rel}$ (%)	$\delta_{stat}$ (% fb)	$\delta_{syst}$ (% fb)
<b>CMS preliminary choice</b>					
0 - 10	0.34	+0.11 -0.096	+33 -28	+0.1 -0.091	+0.048 -0.031
10 - 20	0.53	+0.13 -0.11	+25 -21	+0.12 -0.11	+0.056 -0.037
20 - 30	0.42	+0.11 -0.097	+27 -23	+0.1 -0.093	+0.044 -0.027
30 - 45	0.43	+0.11 -0.094	+25 -22	+0.1 -0.089	+0.044 -0.029
45 - 80	0.52	+0.11 -0.1	+22 -19	+0.1 -0.092	+0.05 -0.038
80 - 120	0.25	+0.073 -0.062	+29 -25	+0.069 -0.06	+0.024 -0.018
120 - 200	0.18	+0.057 -0.048	+31 -26	+0.055 -0.046	+0.016 -0.011
200 - 13000	0.082	+0.036 -0.028	+44 -34	+0.035 -0.028	+0.008 -0.004
Total bins = 8	$\sigma_{fid} = \sum d\sigma_{fid} = 2.8$ (fb)				

<sup>411</sup> Figure 10 shows the four lepton mass distributions for an Asimov dataset generated using SM  
<sup>412</sup> cross section values and efficiencies from the  $gg \rightarrow H$  production mode from POWHEG+JHUGEN,  
<sup>413</sup> and resulting fitted values of PDFs of signal and background for different bins of  $p_T(H)$  (all fi-  
<sup>414</sup> nal states combined).

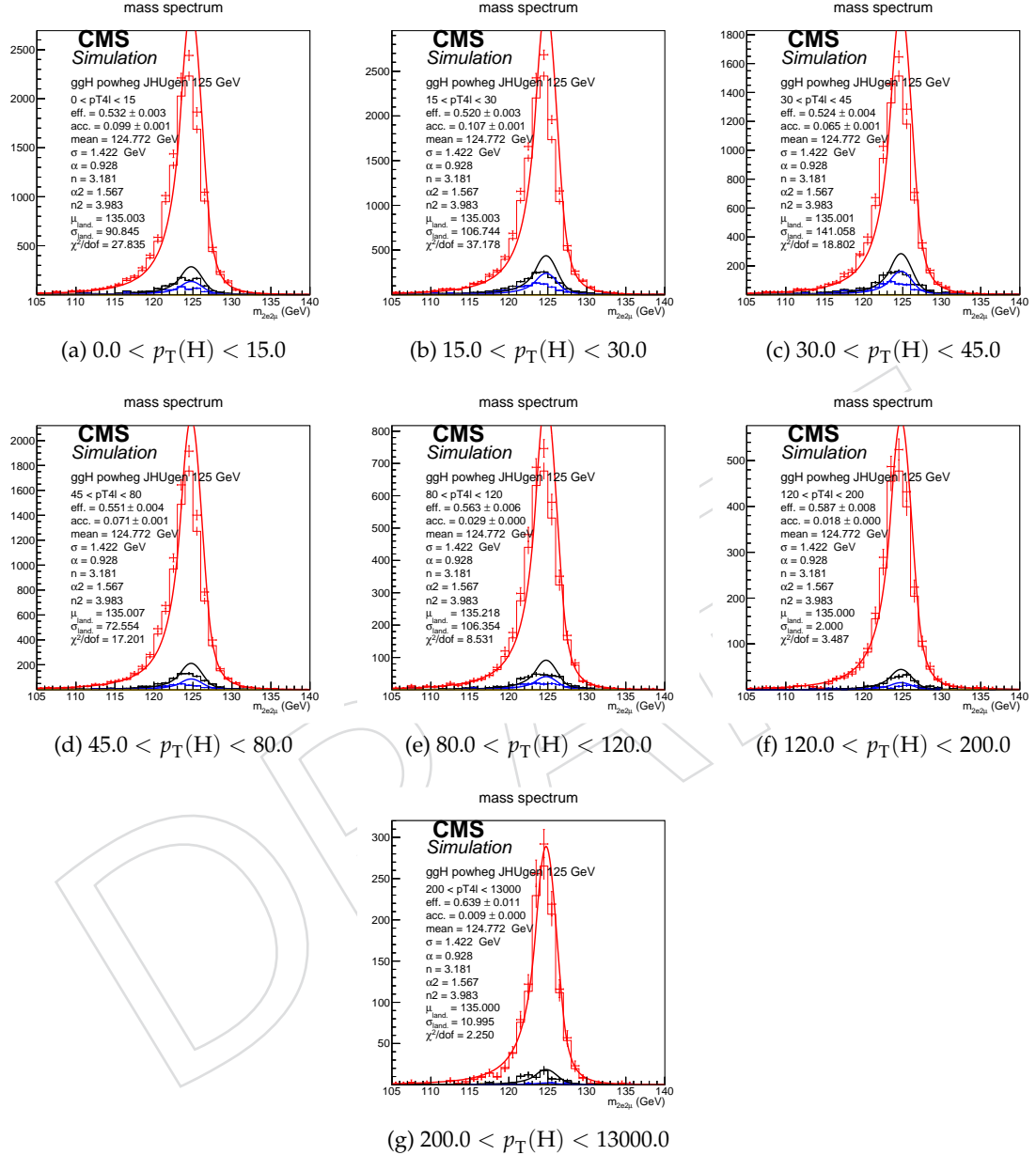


Figure 8: Example signal shapes at reconstruction level for a resonance of  $m(4\ell)$  in  $2e2\mu$  final state for the  $gg \rightarrow H$  production mode from POWHEG+JHUGEN in different bins of  $p_{\text{T}}(\text{H})$ . The black curve represents events which do not pass the fiducial volume selection. The curve has no effect on the result.

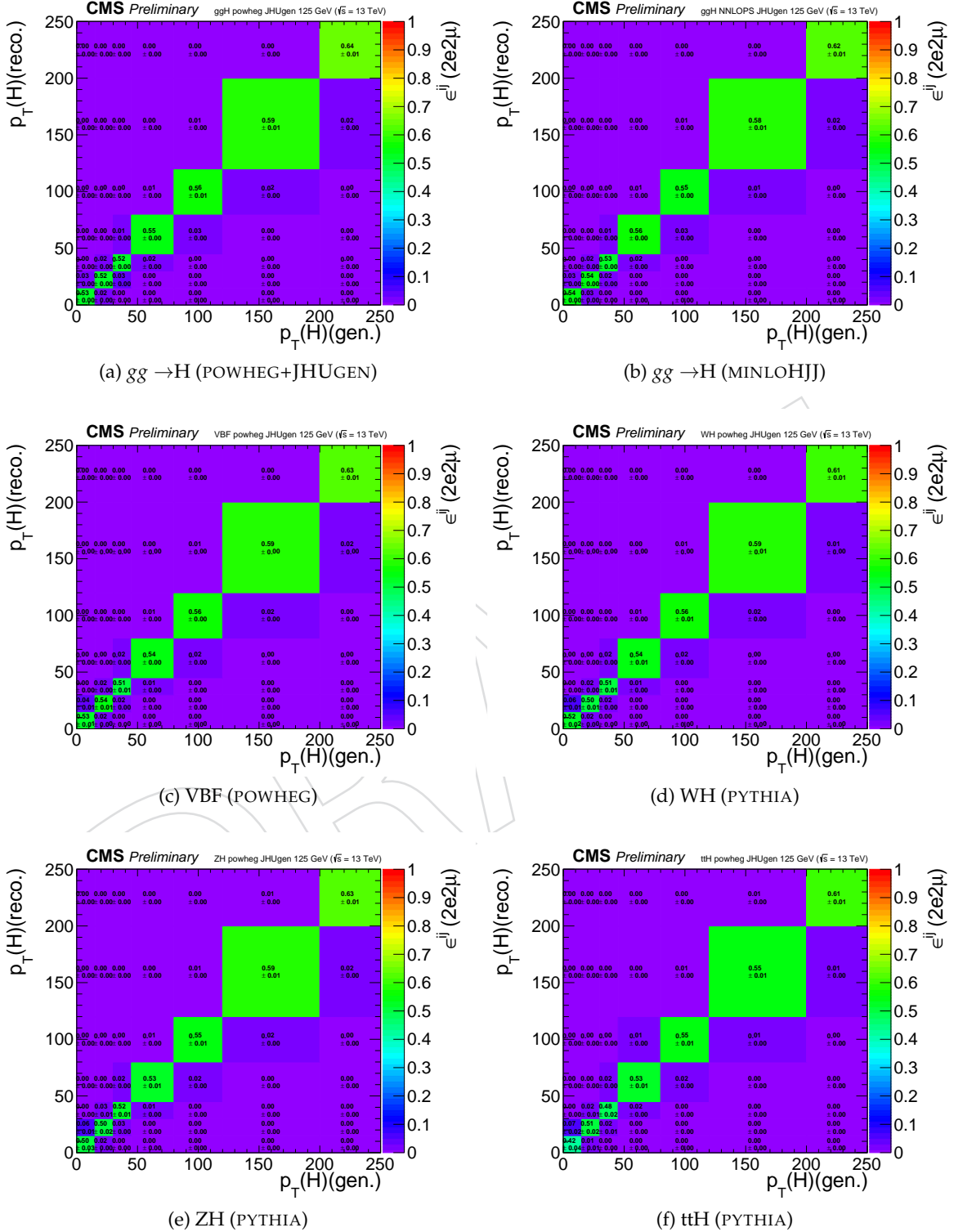


Figure 9: Efficiency response matrices for  $p_T(H)$  for different SM production modes in the  $2e2\mu$  final state using 2018 samples.

<sup>415</sup> **7.8 Interpretations**

<sup>416</sup> To be updated

<sup>417</sup> **7.8.1  $\kappa$ -framework**

<sup>418</sup> To be updated

<sup>419</sup> **7.8.2 Effective Field Theory**

<sup>420</sup> To be updated.

<sup>421</sup> **7.8.3  $\kappa$ -framework**

DRAFT

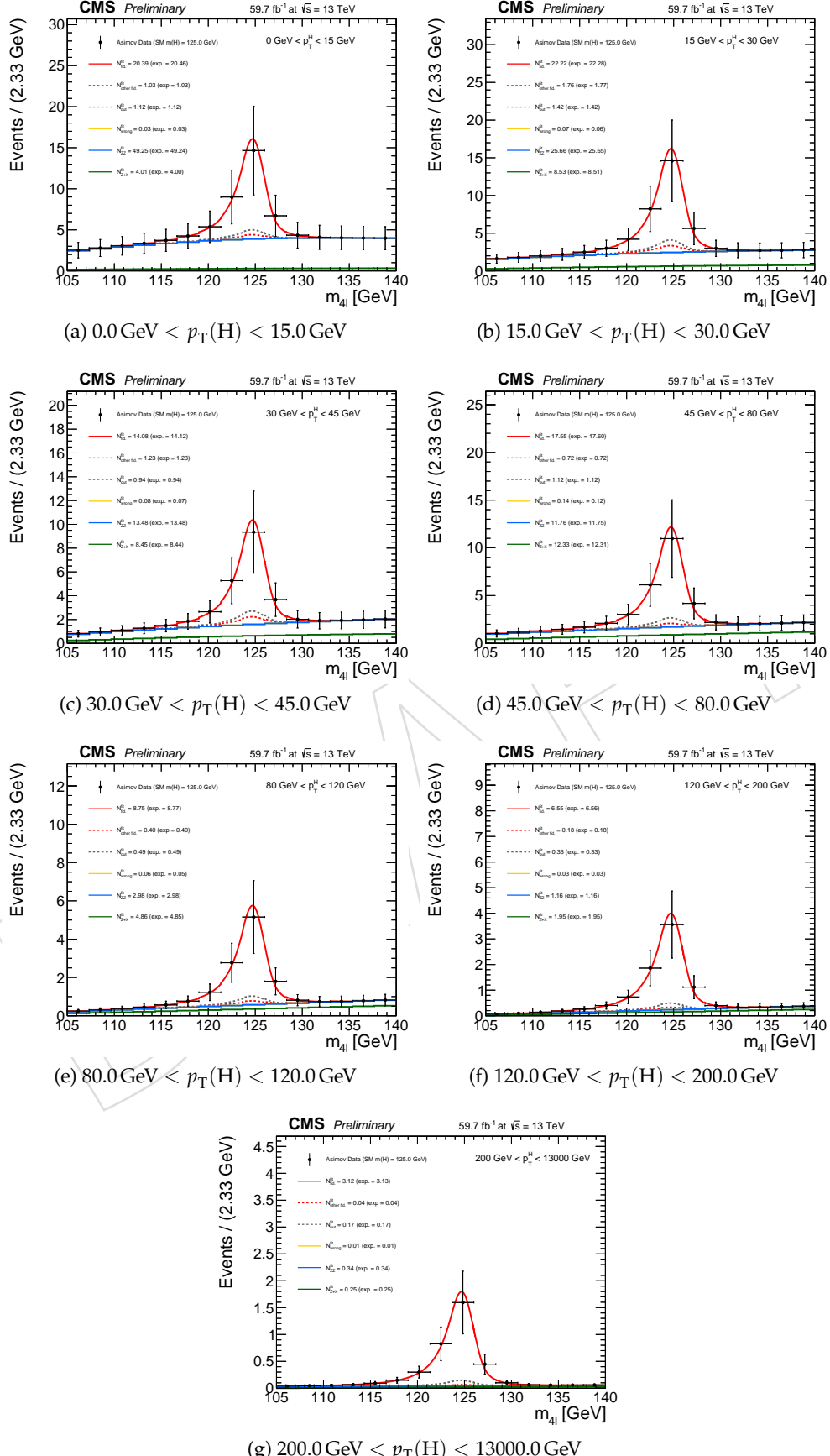


Figure 10: Four lepton mass distributions for an Asimov dataset generated using SM cross section values and SM efficiencies where the  $gg \rightarrow H$  prediction is from POWHEG+JHUGEN and resulting fitted values of PDFs of signal and background for different bins of  $p_T(H)$  (all final states combined).

## 422 8 Systematic uncertainties

423 The main experimental uncertainties which affect both signal and background are the uncer-  
 424 tainty on the integrated luminosity (from to 2.3% to 2.6%, depending on the data taking period)  
 425 and the uncertainty on the lepton identification and reconstruction efficiency (ranging from 1  
 426 to 2.5% and from 11 to 15.5% on the overall yields, in the  $4\mu$  and  $4e$  channels, respectively).  
 427 Experimental uncertainties for the reducible background estimation, described in Section ??,  
 428 vary between 6% to 32% from the variation of the fake rates. The mismatch in the composition  
 429 of backgrounds between the samples where the fake rate is derived and where it is applied  
 430 accounts for about 30%.

431 The uncertainty of the lepton energy scale is assessed by propagating down to the four-leptons  
 432 invariant mass the uncertainty associated the lepton momentum corrections on each individual  
 433 lepton. The uncertainty is treated as uncorrelated (all up or all down). The new four-leptons  
 434 invariant mass obtained this way is then fitted with only the mean value floating. The differ-  
 435 ence between the new mean value and the default one gives an estimation of the impact of the  
 436 lepton energy scale. The values are reported in the Table 18, together with the estimation of the  
 437 impact of lepton momentum resolution, following a similar procedure.

Table 18: Difference (in %) between the nominal mean and width of the four-leptons Higgs mass distribution and those where the lepton momentum scale and resolution uncertainties have been propagated.

	4e	$4\mu$	$2e2\mu$
Scale Difference (%)	0.087	0.049	0.069
Resolution Difference (%)	17	12	17

438 The results obtained this way suggest that the uncertainties from 2016 (20% on the resolution,  
 439 0.3% for the  $4e$  channel for scale) are still valid.

440 Theoretical uncertainties which affect both the signal and background estimation include un-  
 441 certainties from the renormalization and factorization scale and choice of PDF set. The uncer-  
 442 tainty from the renormalization and factorization scale is determined by varying these scales  
 443 between 0.5 and 2 times their nominal value while keeping their ratio between 0.5 and 2. In the  
 444 case of ggF production mode, the QCD scale uncertainty is broken down to 9 different sources.  
 445 The renormalization and factorization scale affect the overall cross section, the migration of  
 446 the stage1.1 bins in different Higgs pT and number of jets, top loop effects are treated as inde-  
 447 pendent uncertainties, and correlated among different stage 1.1 bins. The numbers are shown  
 448 in Fig ???. The uncertainty from the PDF set is determined by taking the root mean square of  
 449 the variation when using different replicas of the default NNPDF set. PDF uncertainty arises  
 450 from uncertainty is also taken into account. On the background, an additional uncertainty of  
 451 10% on the K factor used for the  $gg \rightarrow ZZ$  prediction is applied as described in Section ???. A  
 452 systematic uncertainty of 2% on the branching ratio of  $H \rightarrow ZZ \rightarrow 4\ell$  only affects the signal  
 453 yield. In the case of event categorization, experimental and theoretical uncertainties which ac-  
 454 count for possible migration of signal and background events between categories are included.  
 455 The main sources of uncertainty on the event categorization include the QCD scale, PDF set,  
 456 and the modeling of hadronization and the underlying event. These uncertainties amount to  
 457 between 4–20% for the signal and 3–20% for the background depending on the category. The  
 458 lower range corresponds to the VBF and VH processes and the upper range corresponds to the  
 459  $gg \rightarrow H$  process yield in the VBF-2jet-tagged category. Additional uncertainties come from the  
 460 imprecise knowledge of the jet energy scale (from 2% for the  $gg \rightarrow H$  yield in the untagged  
 461 category to 22% for  $gg \rightarrow H$  yield in the VBF-2jet-tagged category) and b-tagging efficiency

<sup>462</sup> and mistag rate (up to 10% in the  $t\bar{t}H$ -tagged category). In the cross section measurement, the  
<sup>463</sup> signal cross section uncertainties arise from theoretical sources are removed.

Table 19: Summary of the experimental systematic uncertainties in the  $H \rightarrow 4\ell$  measurements of 2016, 2017 and 2018 data.

Summary of relative systematic uncertainties			
Common experimental uncertainties			
Luminosity	2.6 %	2.3 %	2.5 %
Lepton identification/reconstruction efficiencies	1.2 – 15.5 %	1.1 – 12 %	0.7 – 11 %
Background related uncertainties			
Reducible background ( $Z+X$ )	31 – 42 %	31 – 38 %	31 – 37 %
Signal related uncertainties			
Lepton energy scale	0.04 – 0.3 %	0 %	0 %
Lepton energy resolution	20 %	20 %	20 %

Table 20: Summary of the theory systematic uncertainties in the  $H \rightarrow 4\ell$  measurements for the inclusive analysis

Summary of inclusive theory uncertainties	
QCD scale (gg)	± 3.9 %
PDF set (gg)	± 3.2 %
Bkg K factor (gg)	± 10 %
QCD scale (VBF)	+0.4/-0.3 %
PDF set (VBF)	± 2.1 %
QCD scale (WH)	+0.5/-0.7 %
PDF set (WH)	± 1.9 %
QCD scale (ZH)	+3.8/-3.1 %
PDF set (ZH)	± 1.6 %
QCD scale ( $t\bar{t}H$ )	+5.8/-9.2 %
PDF set ( $t\bar{t}H$ )	± 3.6 %
BR( $H \rightarrow ZZ \rightarrow 4\ell$ )	2 %
QCD scale ( $q\bar{q} \rightarrow ZZ$ )	+3.2/-4.2 % %
PDF set ( $q\bar{q} \rightarrow ZZ$ )	+3.1/-3.4 %
Electroweak corrections ( $q\bar{q} \rightarrow ZZ$ )	± 0.1 %

## <sup>464</sup> 8.1 Systematic uncertainties treatment when combining the data sets

<sup>465</sup> In this Section we describe how different systematic uncertainties are treated when combining  
<sup>466</sup> the data sets. The theoretical uncertainties are correlated. All the experimental systematics are  
<sup>467</sup> treated independently.

468 In this subsection we summarize the status of the analysis after selection, showing the inputs to  
469 the final results, namely the event yields and errors in the full signal region and in a restricted  
470  $m_{4\ell}$  range, and the distributions of the main kinematic variables in data and MC.

### 471 8.1.1 Signal Region Yields

472 The number of candidates observed in data and the expected yields for the backgrounds and  
473 Higgs boson signal after the full event selection are reported in Table 22 for the full range of  
474  $m_{4\ell}$ . Table ?? shows the expected and observed yields for each of the 22 event categories, for a  
475  $118 < m_{4\ell} < 130$  GeV mass window around the Higgs boson peak.

Table 21: The number of expected background and signal events and number observed candidates after full analysis selection, for each final state, for the full mass range  $m_{4\ell} > 70$  GeV, for an integrated luminosity of  $137 \text{ fb}^{-1}$ . Signal and ZZ backgrounds are estimated from Monte Carlo simulation, Z+X is estimated from data.

Channel	$4\mu$	$4e$	$2e2\mu$	$4l$
qqZZ	1414.85	748.64	1835.05	3998.54
ggZZ	268.48	163.45	399.78	831.70
ZX	112.84	48.62	151.71	313.18
EW bkg	15.13	12.73	27.83	55.69
Sum of backgrounds	1811.30	973.45	2414.36	5199.11
Signal ( $m_H = 125$ GeV)	95.27	46.01	118.53	259.82
Total expected	1906.57	1019.46	2532.90	5458.93
Data	1970	1032	2646	5648

### 476 8.1.2 Signal Region Distributions

477 The reconstructed four-lepton invariant mass distribution is shown in Figure 13 for the full  
478 dataset, and compared to expectations from the SM backgrounds, first for the full mass range,  
479 and then zooming on the low-mass range and high-mass range. In Figure 14, the same dis-  
480 tributions are shown split by final state ( $4e$ ,  $4\mu$ , and  $2e2\mu$ ), for the two same mass ranges. In  
481 Figure ??, they are split by event category, for the low-mass range. The SM background dis-  
482 tributions are obtained combining the rate normalization from data-driven methods and knowl-  
483 edge on shapes taken from the MC samples.

484

485 The reconstructed dilepton invariant masses selected as  $Z_1$  and  $Z_2$  are shown in Figures ??  
486 together with their correlation, both full range of  $m_{4\ell}$  and focusing on a  $118 < m_{4\ell} < 130$  GeV  
487 mass window around the Higgs boson peak.

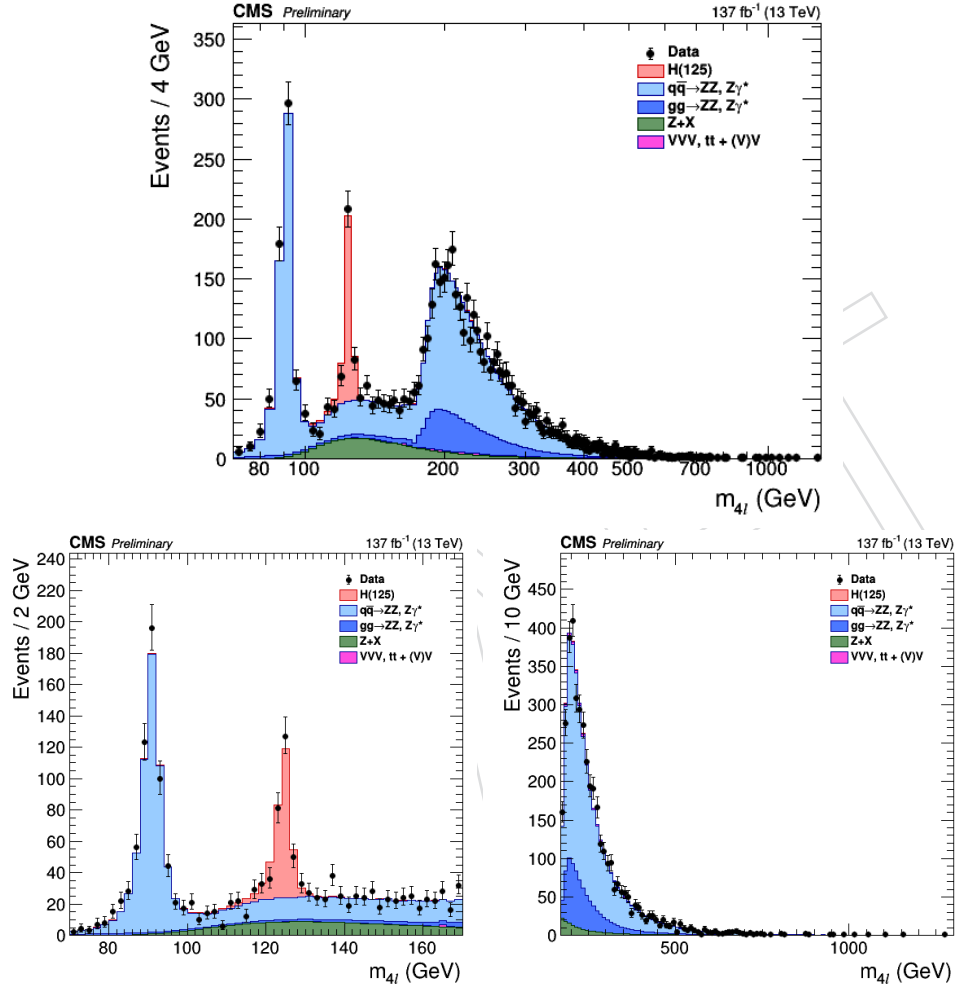


Figure 11: Distribution of the four-lepton reconstructed invariant mass  $m_{4l}$  in the full mass range (top) and the low-mass range (bottom left) and high-mass range (bottom right). Points with error bars represent the data and stacked histograms represent expected distributions. The 125 GeV Higgs boson signal and the ZZ backgrounds are normalized to the SM expectation, the Z+X background to the estimation from data.

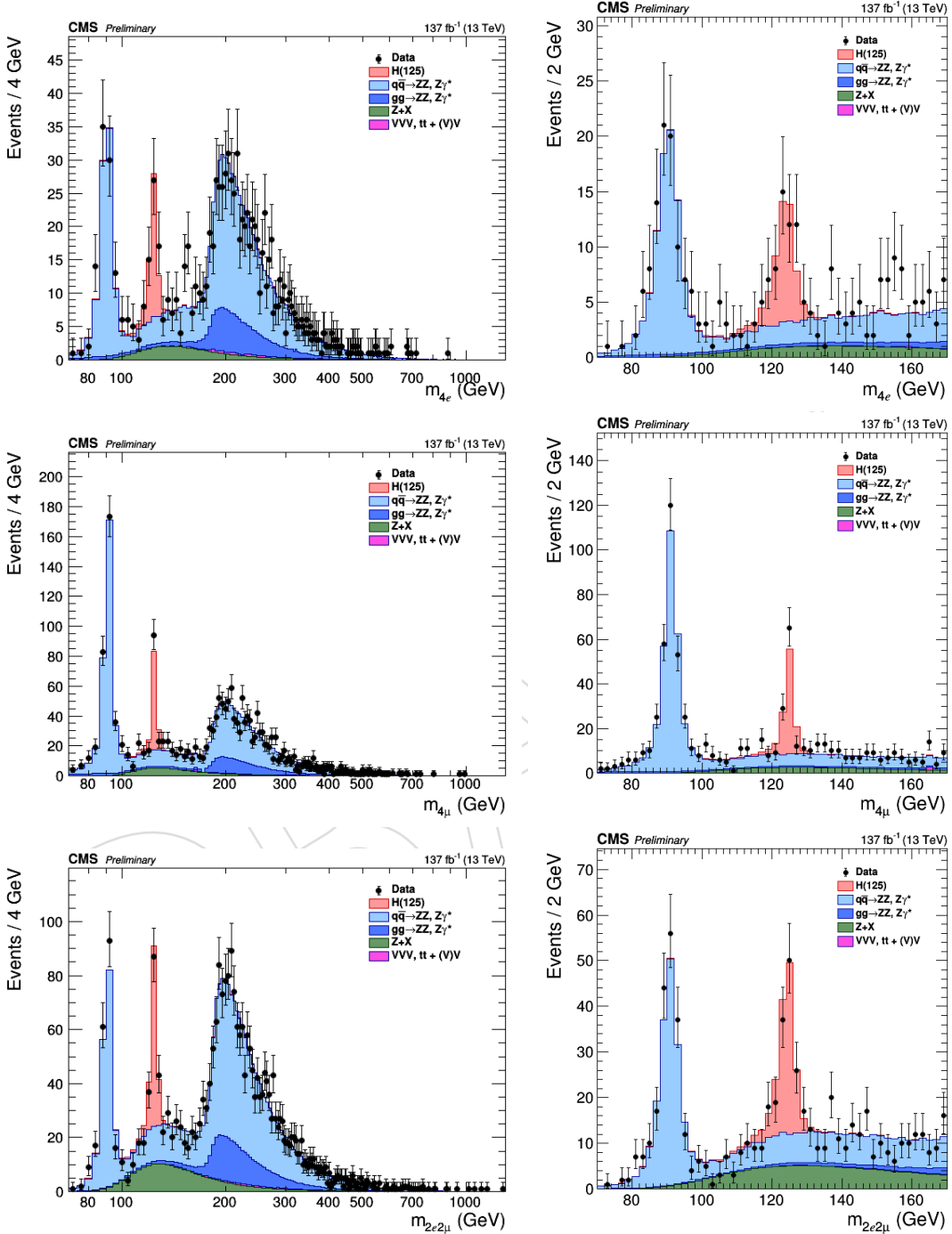
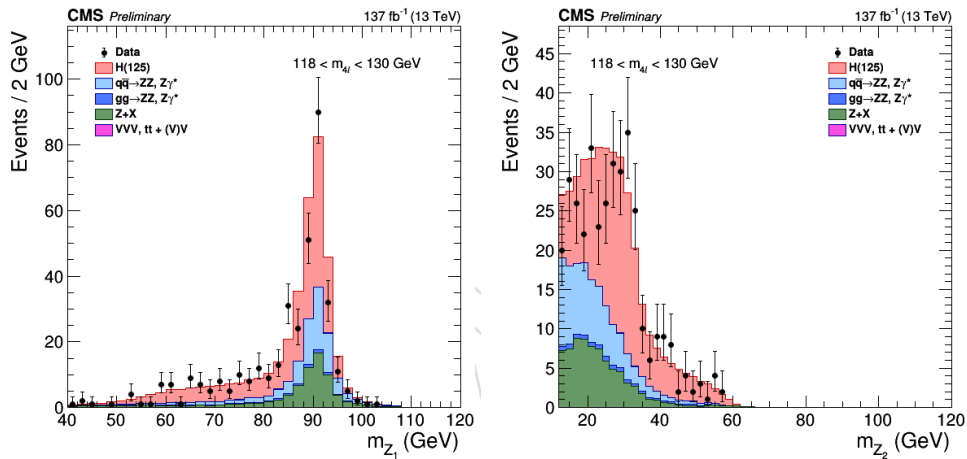


Figure 12: Distribution of the four-lepton reconstructed mass in several sub-channels:  $4e$  (top),  $4\mu$  (middle),  $2e2\mu$  for the low-mass range (bottom) for the full mass range (left) and the low-mass range (right).



Distribution of the  $Z_1$  (left) and  $Z_2$  (right) reconstructed invariant masses for the full mass range (left) and the low mass ( $118 < m_{4\ell} < 130$  GeV) range (right). The stacked histograms and the gray scale represent expected distributions, and points represent the data. The 125 GeV Higgs boson signal and the ZZ backgrounds are normalized to the SM expectation, the Z+X background to the estimation from data.

---

## 488 9 Results

489 In this section, we describe the methods used for the estimation of the significance of the ex-  
 490 cess of events above the SM backgrounds observed in the low-mass region, and of the signal  
 491 strength, i.e. its cross section normalized to the one expected for a SM Higgs.

492 To exploit all the properties of the resonance under study or search, a multi-dimensional fit is  
 493 implemented. For each of the categories defined in Section ??, the variable used in the maxi-  
 494 mum likelihood fit is the four-lepton mass without kinematic refitting  $m_{4\ell}$ .

### 495 9.1 Yields and distributions

496 In this subsection we summarize the status of the analysis after selection, showing the inputs to  
 497 the final results, namely the event yields and errors in the full signal region and in a restricted  
 498  $m_{4\ell}$  range, and the distributions of the main kinematic variables in data and MC.

#### 499 9.1.1 Signal Region Yields

500 The number of candidates observed in data and the expected yields for the backgrounds and  
 501 Higgs boson signal after the full event selection are reported in Table 22 for the full range of  
 502  $m_{4\ell}$ . Table ?? shows the expected and observed yields for each of the 22 event categories, for a  
 503  $118 < m_{4\ell} < 130$  GeV mass window around the Higgs boson peak.

Table 22: The number of expected background and signal events and number observed candi-  
 dates after full analysis selection, for each final state, for the full mass range  $m_{4\ell} > 70$  GeV, for  
 an integrated luminosity of  $137 \text{ fb}^{-1}$ . Signal and ZZ backgrounds are estimated from Monte  
 Carlo simulation, Z+X is estimated from data.

Channel	$4\mu$	$4e$	$2e2\mu$	$4l$
qqZZ	1414.85	748.64	1835.05	3998.54
ggZZ	268.48	163.45	399.78	831.70
ZX	112.84	48.62	151.71	313.18
EW bkg	15.13	12.73	27.83	55.69
Sum of backgrounds	1811.30	973.45	2414.36	5199.11
Signal ( $m_H = 125$ GeV)	95.27	46.01	118.53	259.82
Total expected	1906.57	1019.46	2532.90	5458.93
Data	1970	1032	2646	5648

#### 504 9.1.2 Signal Region Distributions

505 The reconstructed four-lepton invariant mass distribution is shown in Figure 13 for the full  
 506 dataset, and compared to expectations from the SM backgrounds, first for the full mass range,  
 507 and then zooming on the low-mass range and high-mass range. In Figure 14, the same dis-  
 508 tributions are shown split by final state ( $4e$ ,  $4\mu$ , and  $2e2\mu$ ), for the two same mass ranges. In  
 509 Figure ??, they are split by event category, for the low-mass range. The SM background distri-  
 510 butions are obtained combining the rate normalization from data-driven methods and knowl-  
 511 edge on shapes taken from the MC samples.

512

513 The reconstructed dilepton invariant masses selected as  $Z_1$  and  $Z_2$  are shown in Figures ??  
 514 together with their correlation, both full range of  $m_{4\ell}$  and focusing on a  $118 < m_{4\ell} < 130$  GeV  
 515 mass window around the Higgs boson peak.

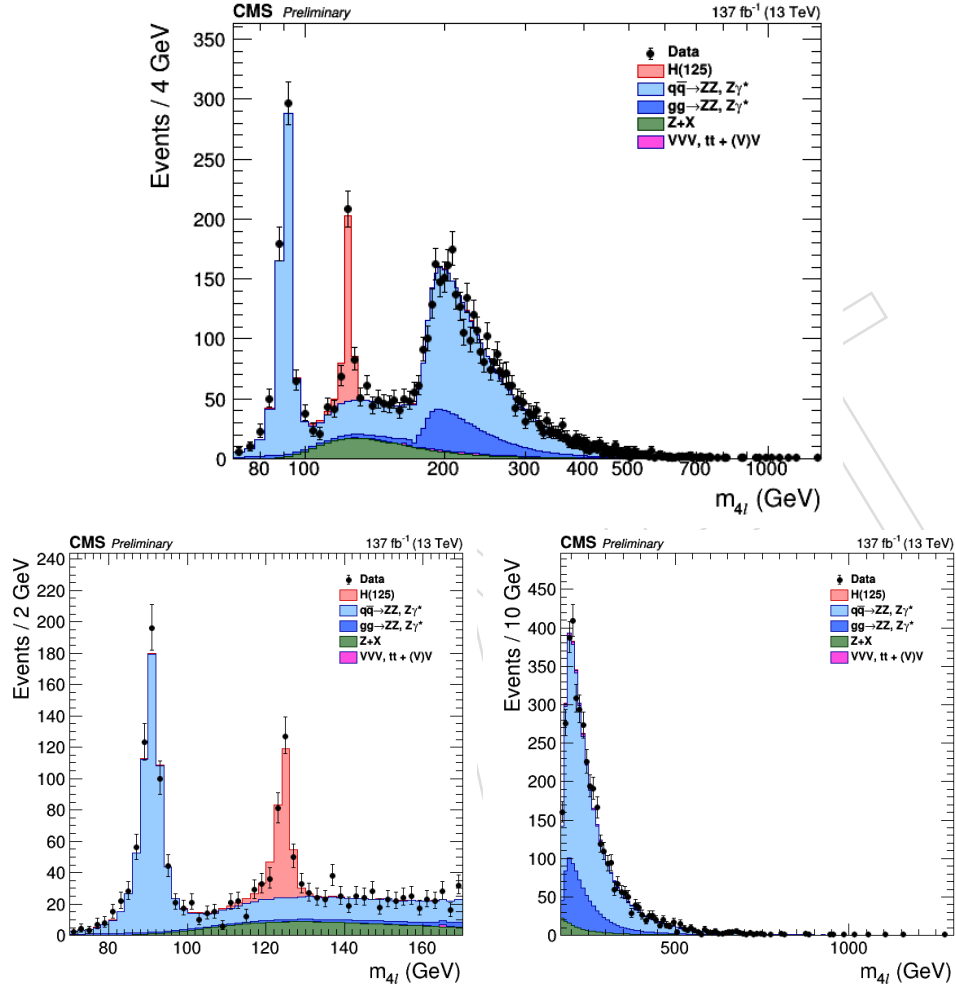


Figure 13: Distribution of the four-lepton reconstructed invariant mass  $m_{4\ell}$  in the full mass range (top) and the low-mass range (bottom left) and high-mass range (bottom right). Points with error bars represent the data and stacked histograms represent expected distributions. The 125 GeV Higgs boson signal and the ZZ backgrounds are normalized to the SM expectation, the  $Z+X$  background to the estimation from data.

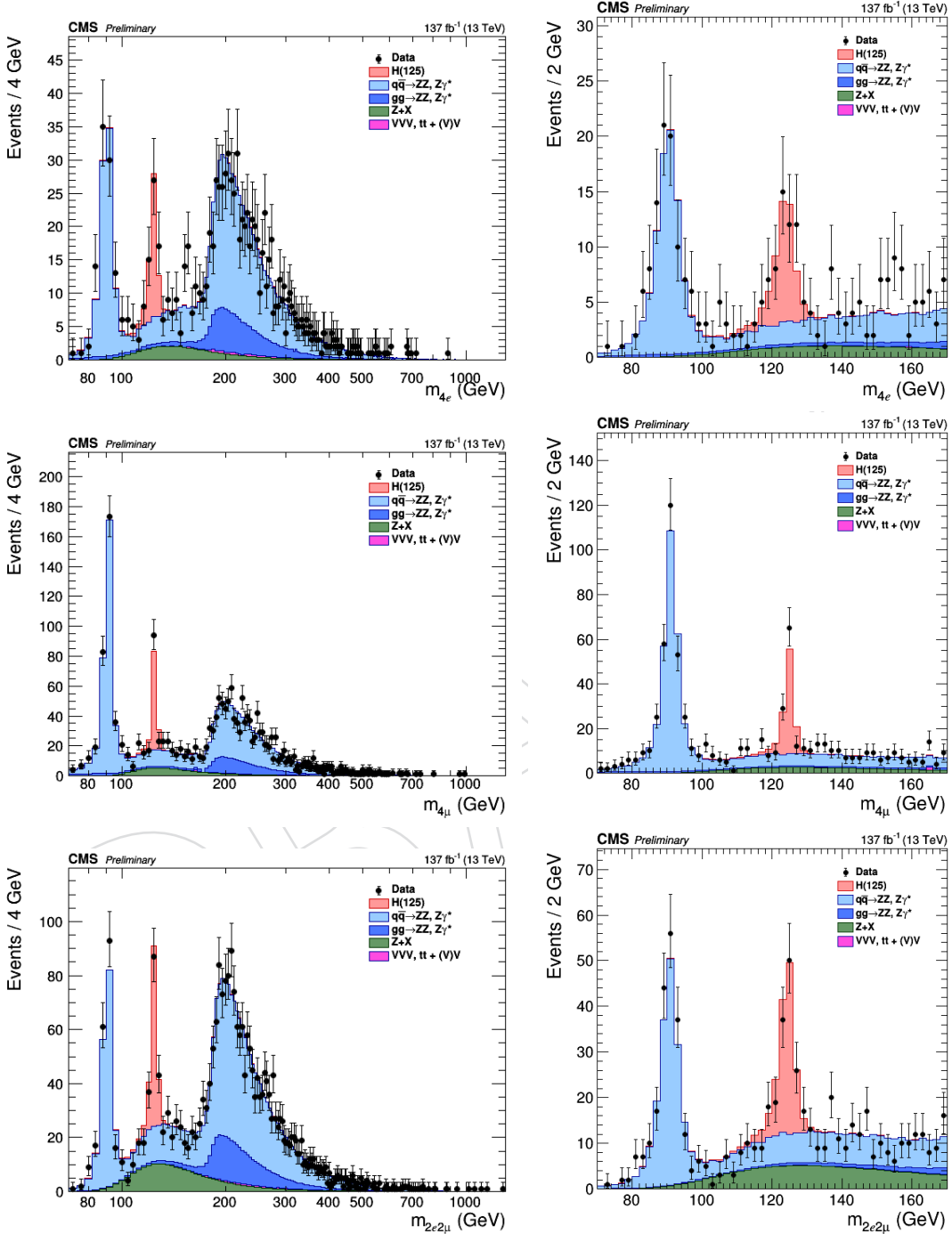
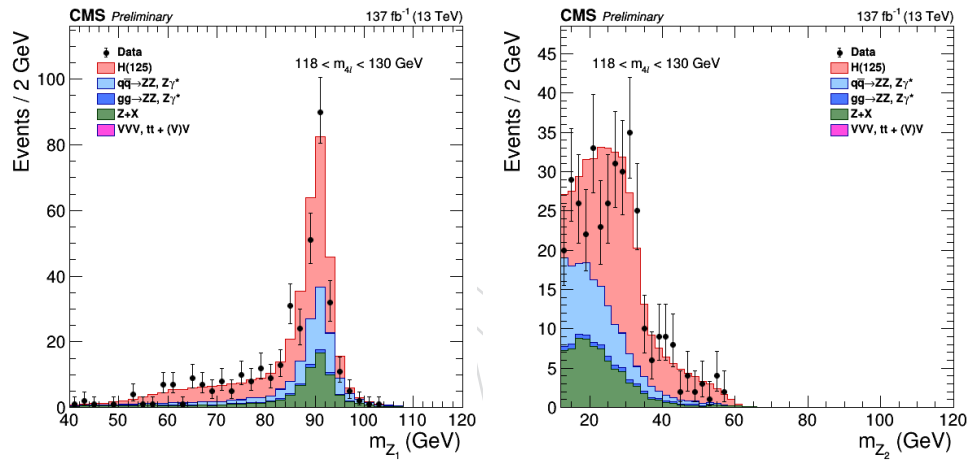


Figure 14: Distribution of the four-lepton reconstructed mass in several sub-channels:  $4e$  (top),  $4\mu$  (middle),  $2e2\mu$  for the low-mass range (bottom) for the full mass range (left) and the low-mass range (right).



Distribution of the  $Z_1$  (left) and  $Z_2$  (right) reconstructed invariant masses for the full mass range (left) and the low mass ( $118 < m_{4\ell} < 130$  GeV) range (right). The stacked histograms and the gray scale represent expected distributions, and points represent the data. The 125 GeV Higgs boson signal and the ZZ backgrounds are normalized to the SM expectation, the Z+X background to the estimation from data.

## 516 9.2 Differential Cross Sections measurement results

517 **FIXME:** Results to be updated with final processing

### 518 9.2.1 Results for Higgs production observables

519 The expected differential cross section results can be seen in Fig. 15.

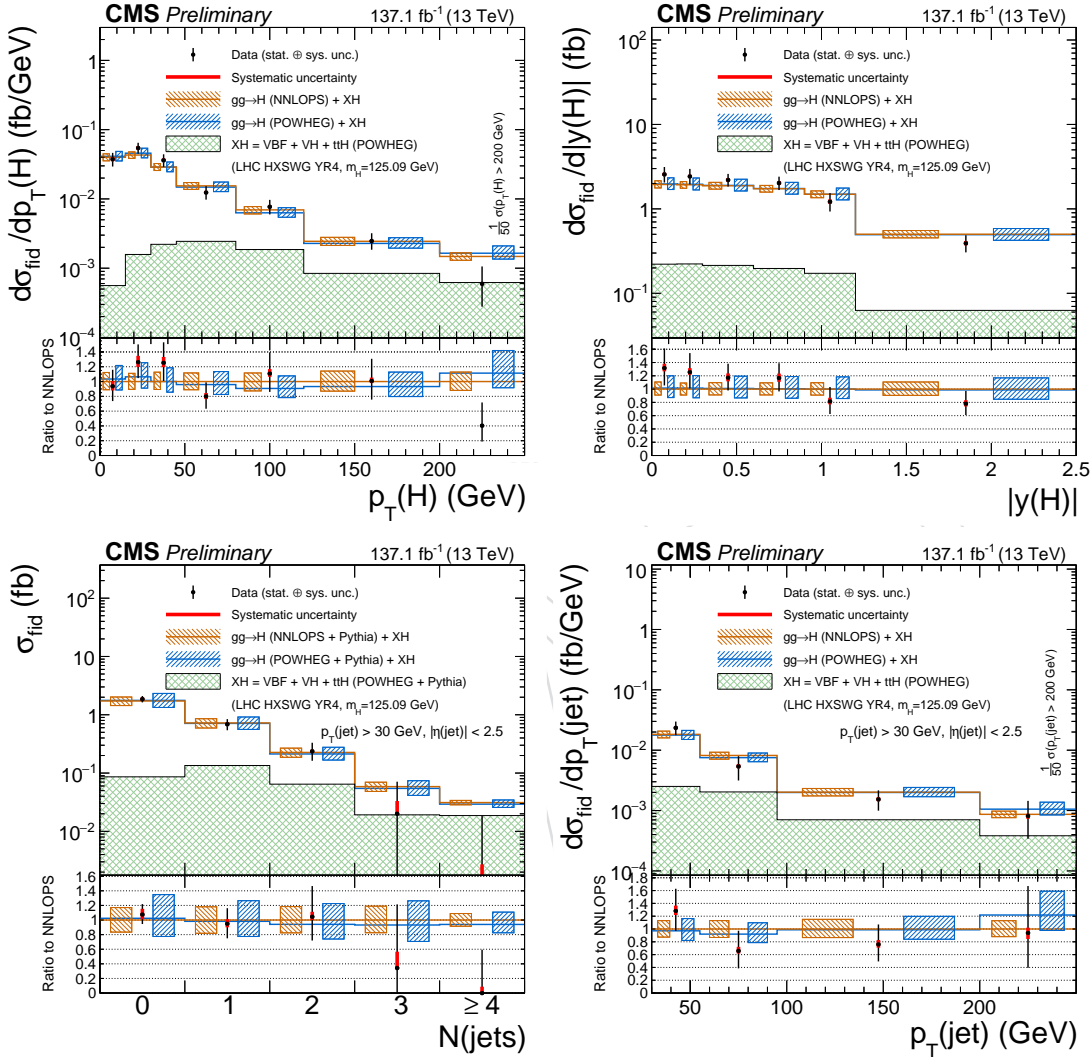


Figure 15: The results of the differential cross section measurement for  $p_T(H)$  (middle left),  $|y(H)|$  (middle right) and  $N(\text{jets})$  (bottom left),  $p_T$  of the leading jet (bottom right). The acceptance and theoretical uncertainties in the differential bins are calculated using POWHEG. The sub-dominant component of the signal ( $\text{VBF} + \text{VH} + \text{ttH}$ ) is denoted as  $\text{XH}$ .

### 520 9.2.2 Results for Higgs decay observables

521 Additional decay observables include  $\Phi$ ,  $\Phi_1$ ,  $m(Z_1)$ ,  $m(Z_2)$ ,  $|\cos\theta^*|$ ,  $|\cos\theta_1|$  and  $|\cos\theta_2|$  which  
522 are studied in  $H \rightarrow 4\ell$  using full Run 2 toy data and compared with the theoretical predictions.

523 In each plot shown below, systematic uncertainty is indicated by red bars and black bars show  
524 total statistical and the systematic uncertainties, combined in quadrature. The blue and brown  
525 colors show the theoretical predictions. The acceptances and the theoretical uncertainties in  
526 differential bins are computed using POWHEG. Sub-dominant production contributions  $\text{XH}$

<sup>527</sup> = VBF + VH + ttH are shown in green separately. The systematic uncertainties correspond to  
<sup>528</sup> the generators accuracy are also taken in to account for differential predictions. The fraction of  
<sup>529</sup> 4 $\mu$ , 4e and 2e2 $\mu$  in each differential bin is allowed to float in fit.

DRAFT

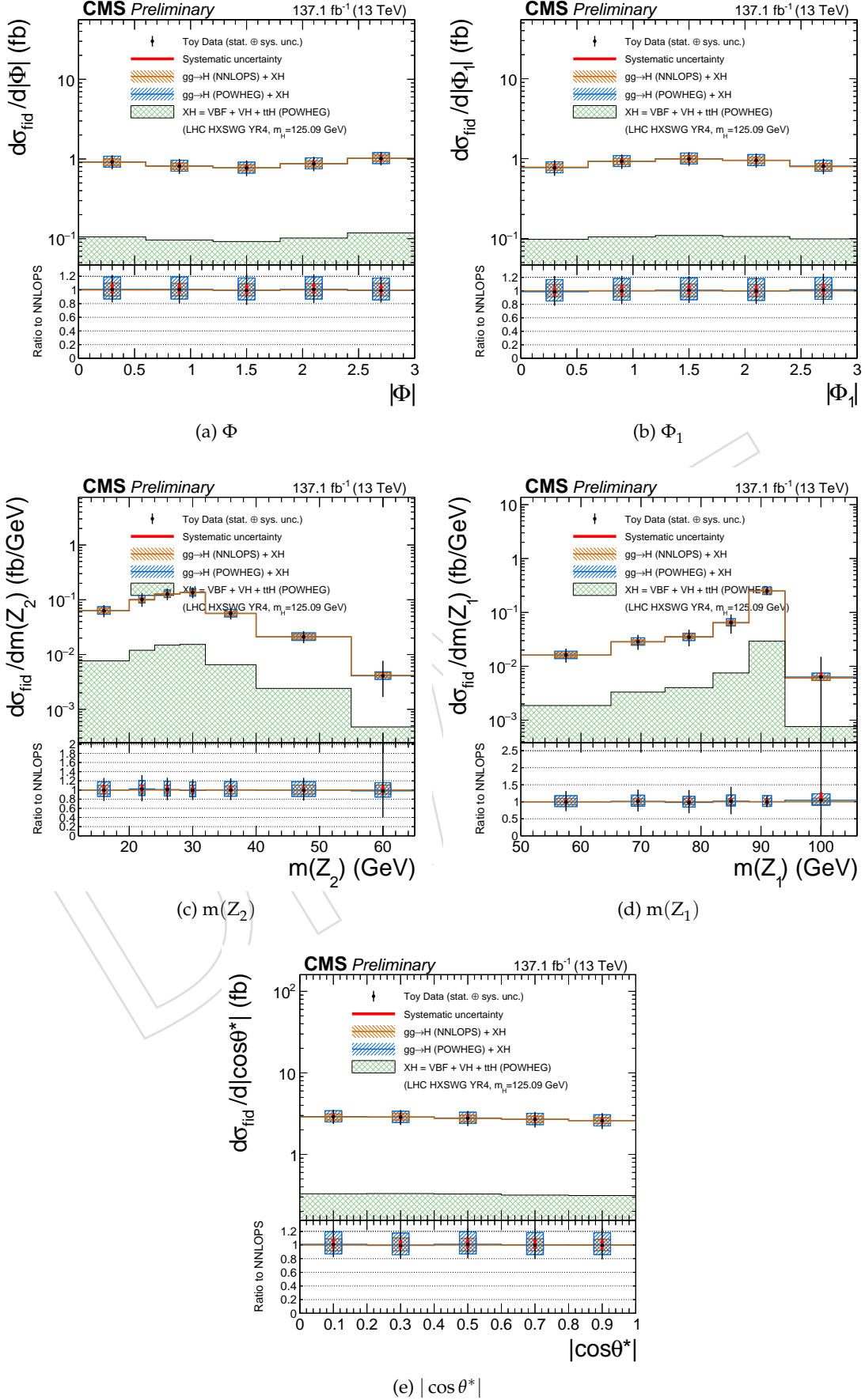


Figure 16: Differential fiducial cross section results using full Run 2 toy data for  $\Phi$ ,  $\Phi_1$ ,  $m(Z_1)$ ,  $m(Z_2)$  and  $|\cos\theta^*|$  in  $H \rightarrow 4\ell$  and comparison with the theoretical predictions.

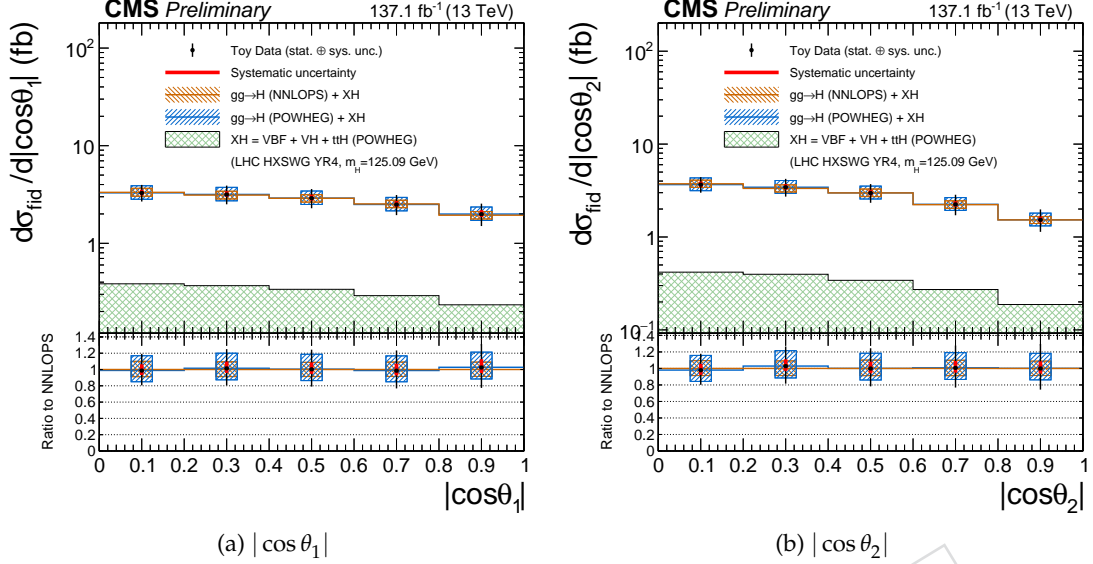


Figure 17: Differential fiducial cross section results using full Run 2 toy data for  $|\cos \theta_1|$ ,  $|\cos \theta_2|$  in  $H \rightarrow 4\ell$  and comparison with the theoretical predictions. Systematic uncertainty is indicated by red bars and black bars show total statistical and the systematic uncertainties, combined in quadrature. The blue and brown colors show the theoretical predictions. The acceptances and the theoretical uncertainties in differential bins are computed using POWHEG. Sub-dominant production contributions  $XH = VBF + VH + t\bar{t}H$  are shown in green separately. The systematic uncertainties correspond to the generators accuracy are also taken in to account for differential predictions. The fraction of  $4\mu$ ,  $4e$  and  $2e2\mu$  in each differential bin is allowed to float in fit.

530 **9.3 Double differential cross section measurements**

531 Differential measurements are extended upto higher dimension upto 2. Several 2D combina-  
532 tion are aimed to be measured e.g.  $m(Z_1)$  vs  $m(Z_2)$  and so forth. To be updated further.

533 **9.4 Interpretations**

534 To be updated.

535 **9.4.1 Constraints on Yukawa Couplings: Fits of coupling modifiers ( $\kappa_b$  vs.  $\kappa_c$ )**

536 To be updated.

537 **9.4.2 Constraint on Higgs boson trilinear self-coupling ( $\kappa_\lambda$ )**

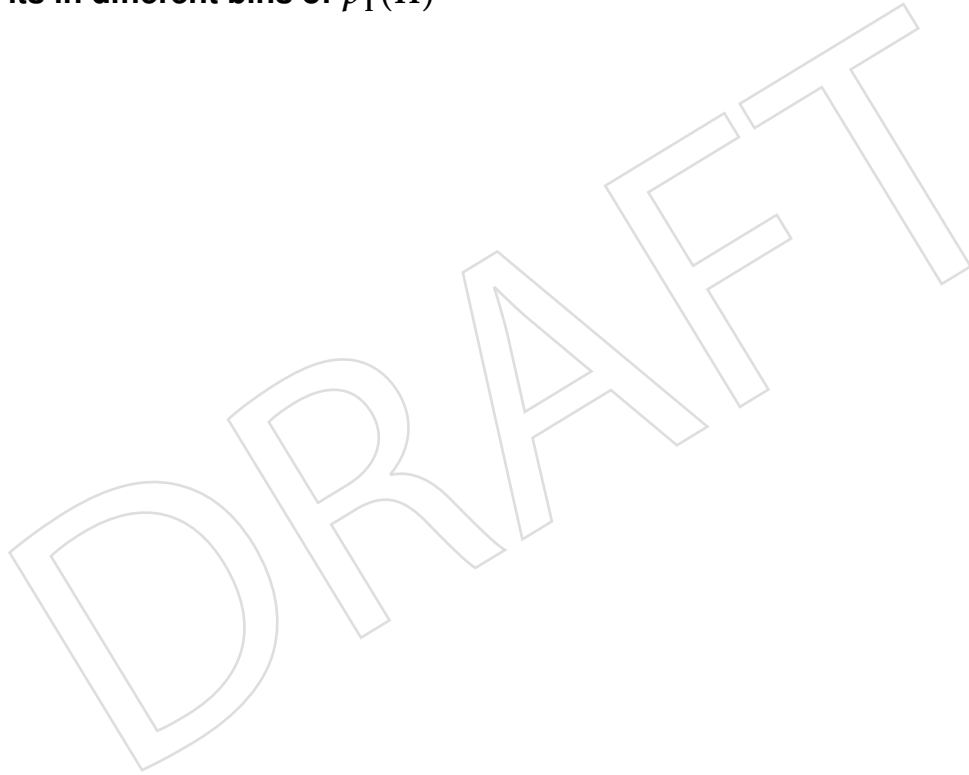
538 To be updated.

DRAFT

## 539 A Signal Shapes and Efficiencies

540 For all plots showing fits to the signal distributions, the red histograms show the distribution of  
541 events which pass both the fiducial selection at generator level and pass the full reconstruction  
542 level selection, including the selection on  $p_T(H)$ . The red curve shows a fit to this distribution  
543 using a double-sided crystal ball function, and the resulting  $\sigma$  of the fit is also shown on the  
544 plot. The blue histograms show events which pass the full reconstruction level selection, and  
545 pass the fiducial selection at generator level within a different  $p_T(H)$  bin. The blue curves show  
546 a fit to this distribution using the same function as the red curve with a different normalization.  
547 The black histograms show the distribution of events which pass the full reconstruction level  
548 selection but do not pass the fiducial selection at generator level, and the black curve shows a fit  
549 to this distribution using the same function as the red curve but with a different normalization.  
550 The yellow histogram shows events which pass the full reconstruction level selection but where  
551 one of the four selected leptons does not originate from the Higgs boson. The yellow curve  
552 shows a fit to this distribution using a Landau function.

553 **A.1 Fits in different bins of  $p_T(H)$**



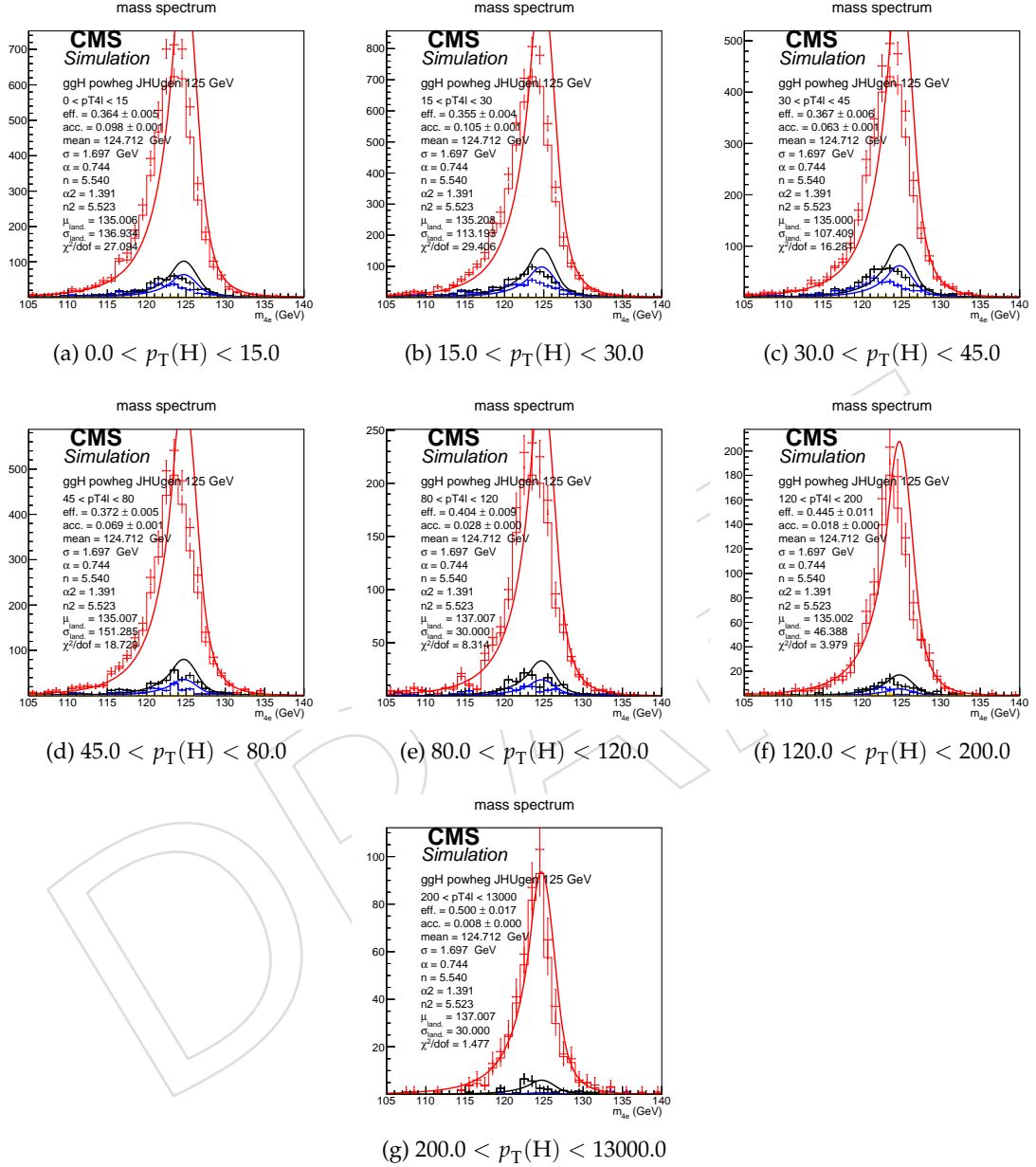


Figure 18: Example signal shapes at reconstruction level for a resonance of  $m(4\ell)$  in  $4e$  final state for the  $gg \rightarrow H$  production mode from POWHEG+JHUGEN in different bins of  $p_T(H)$ . The black curve represents events which do not pass the fiducial volume selection. The curve has no effect on the result.

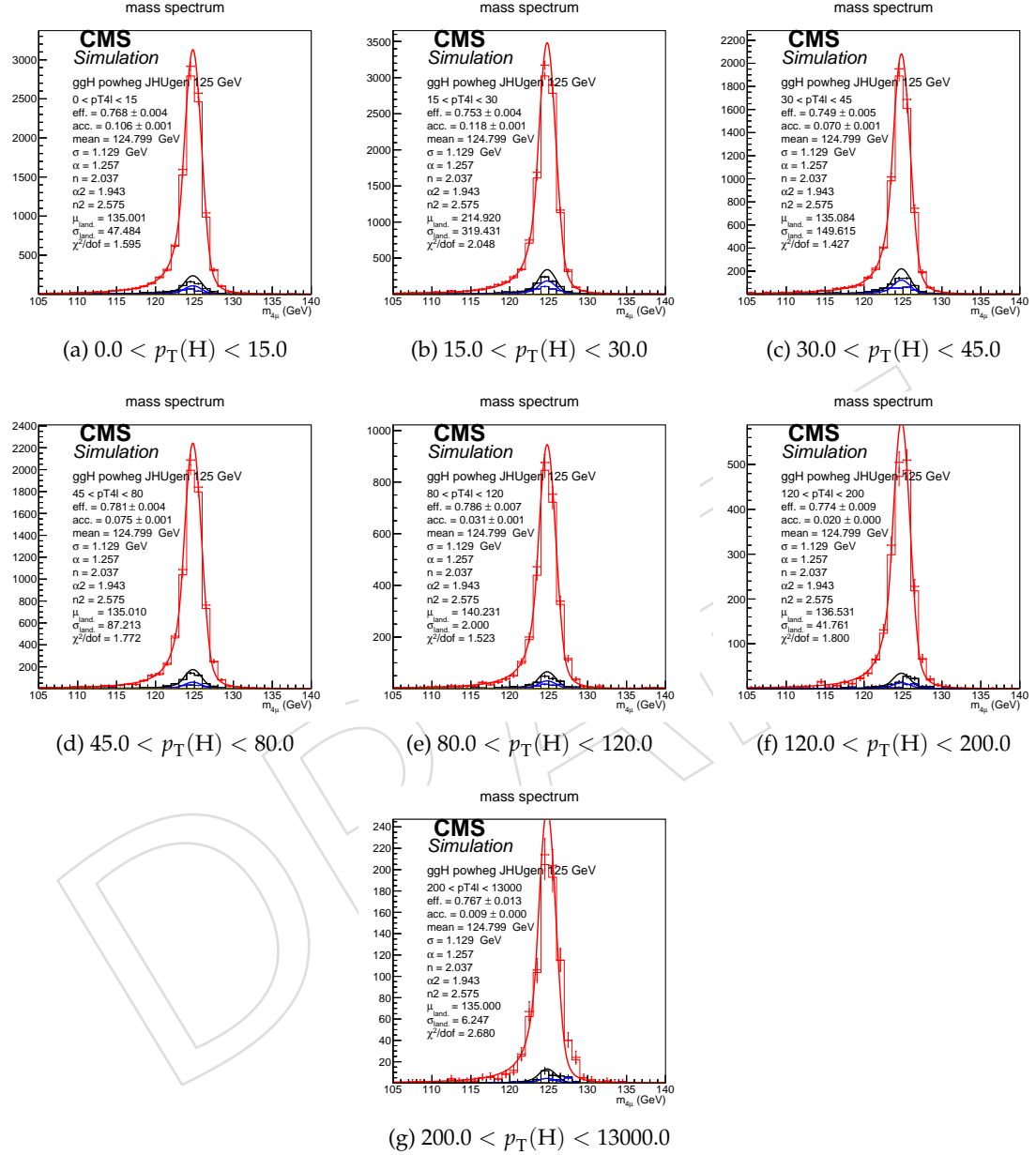


Figure 19: Example signal shapes at reconstruction level for a resonance of  $m(4\ell)$  in  $4\mu$  final state for the  $gg \rightarrow H$  production mode from POWHEG+JHUGEN in different bins of  $p_T(H)$ . The black curve represents events which do not pass the fiducial volume selection. The curve has no effect on the result.

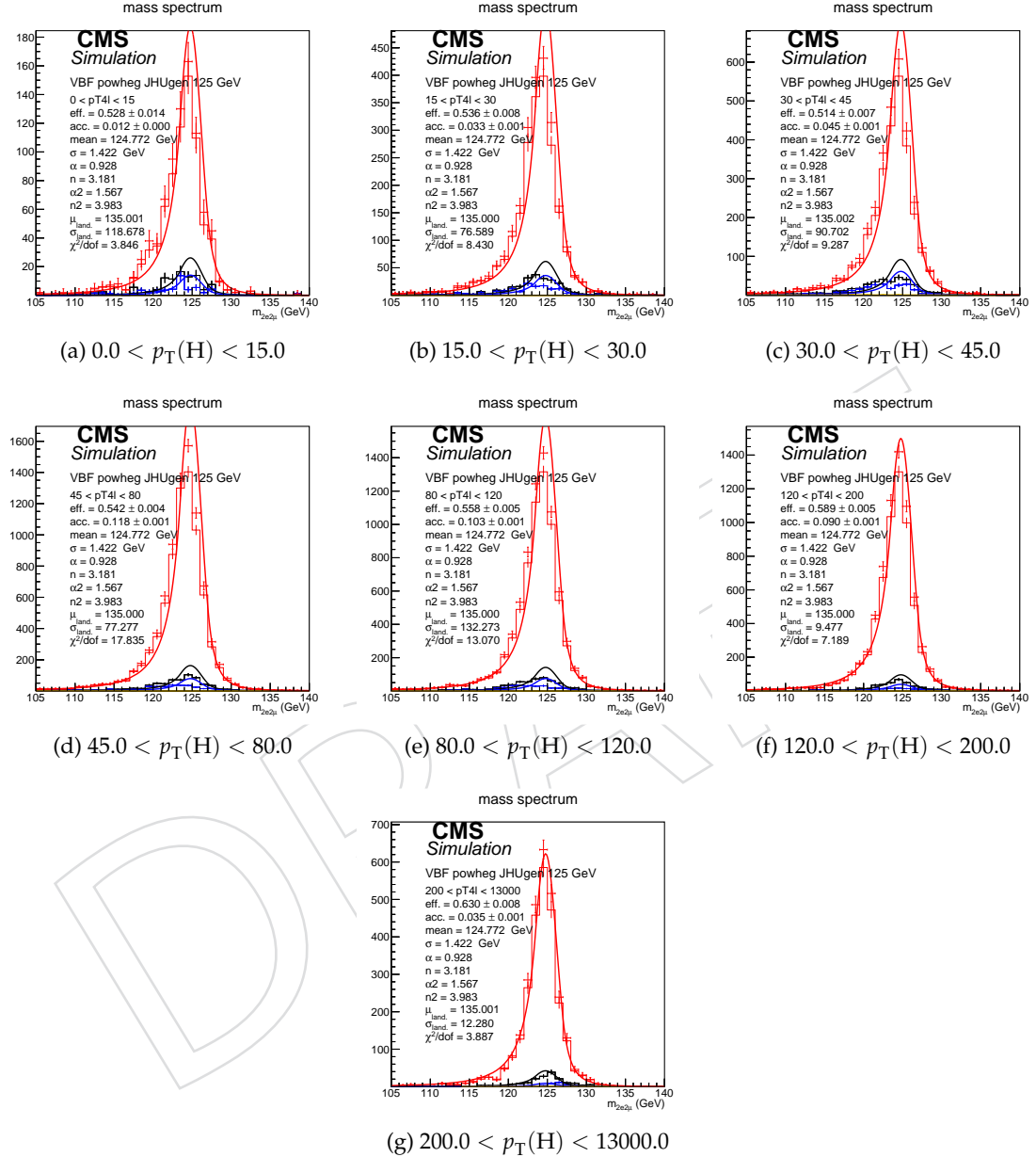


Figure 20: Example signal shapes at reconstruction level for a resonance of  $m(4\ell)$  in  $2e2\mu$  final state for the  $VBF$  production mode from POWHEG+JHUGEN in different bins of  $p_T(H)$ . The black curve represents events which do not pass the fiducial volume selection. The curve has no effect on the result.

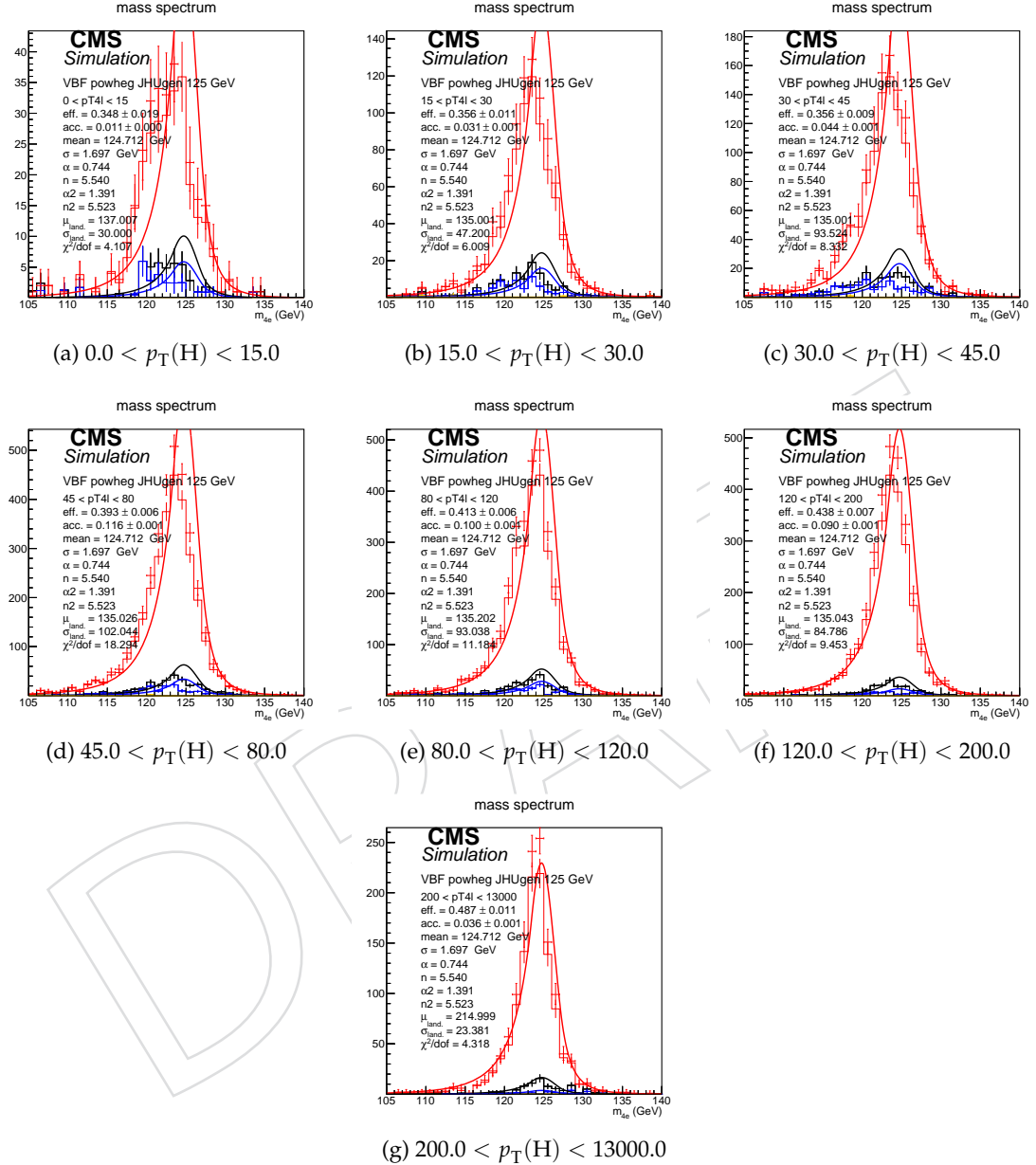


Figure 21: Example signal shapes at reconstruction level for a resonance of  $m(4\ell)$  in  $4e$  final state for the  $VBF$  production mode from POWHEG+JHUGEN in different bins of  $p_T(H)$ . The black curve represents events which do not pass the fiducial volume selection. The curve has no effect on the result.

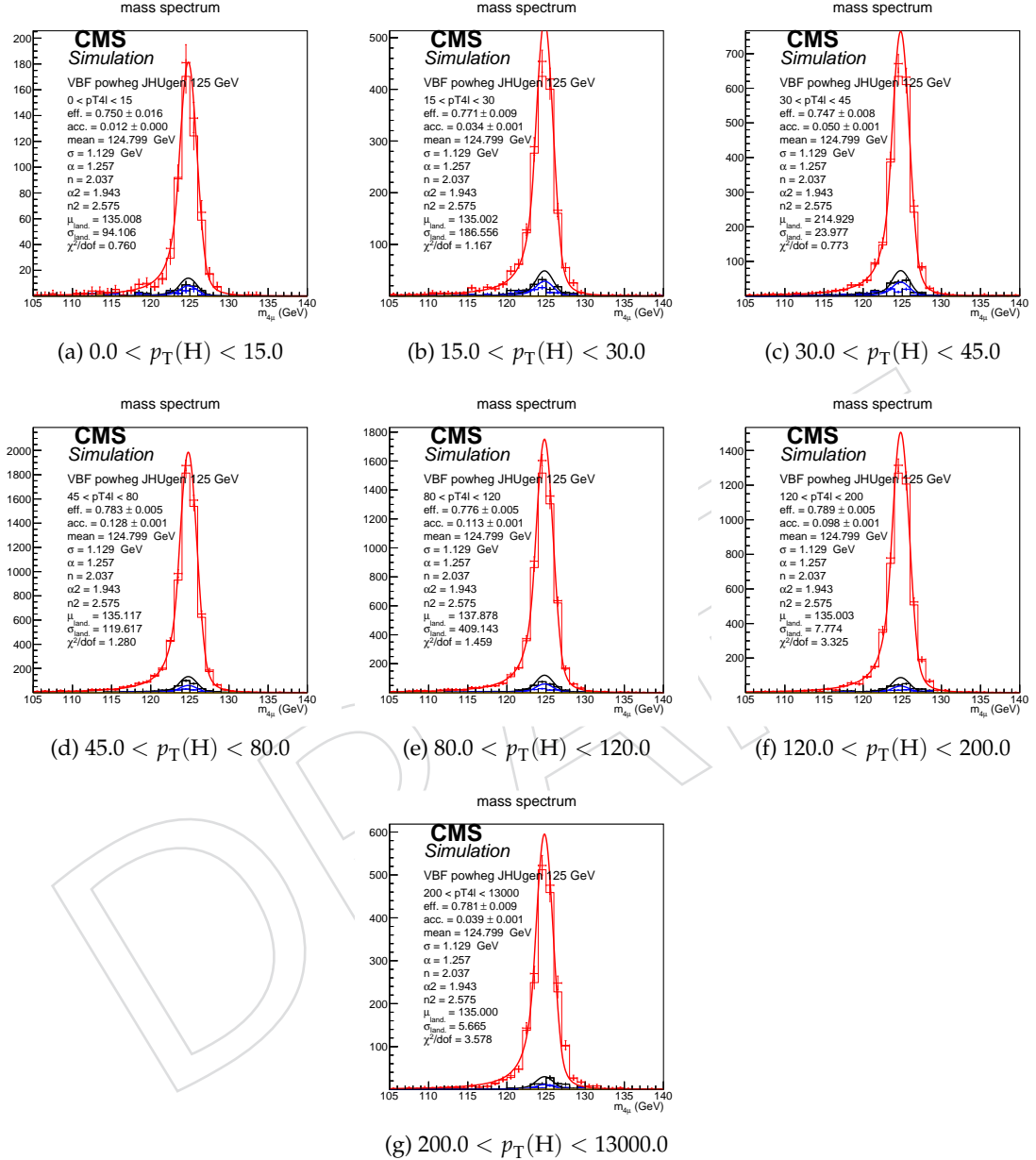


Figure 22: Example signal shapes at reconstruction level for a resonance of  $m(4\ell)$  in  $4\mu$  final state for the  $VBF$  production mode from POWHEG+JHUGEN in different bins of  $p_T(H)$ . The black curve represents events which do not pass the fiducial volume selection. The curve has no effect on the result.

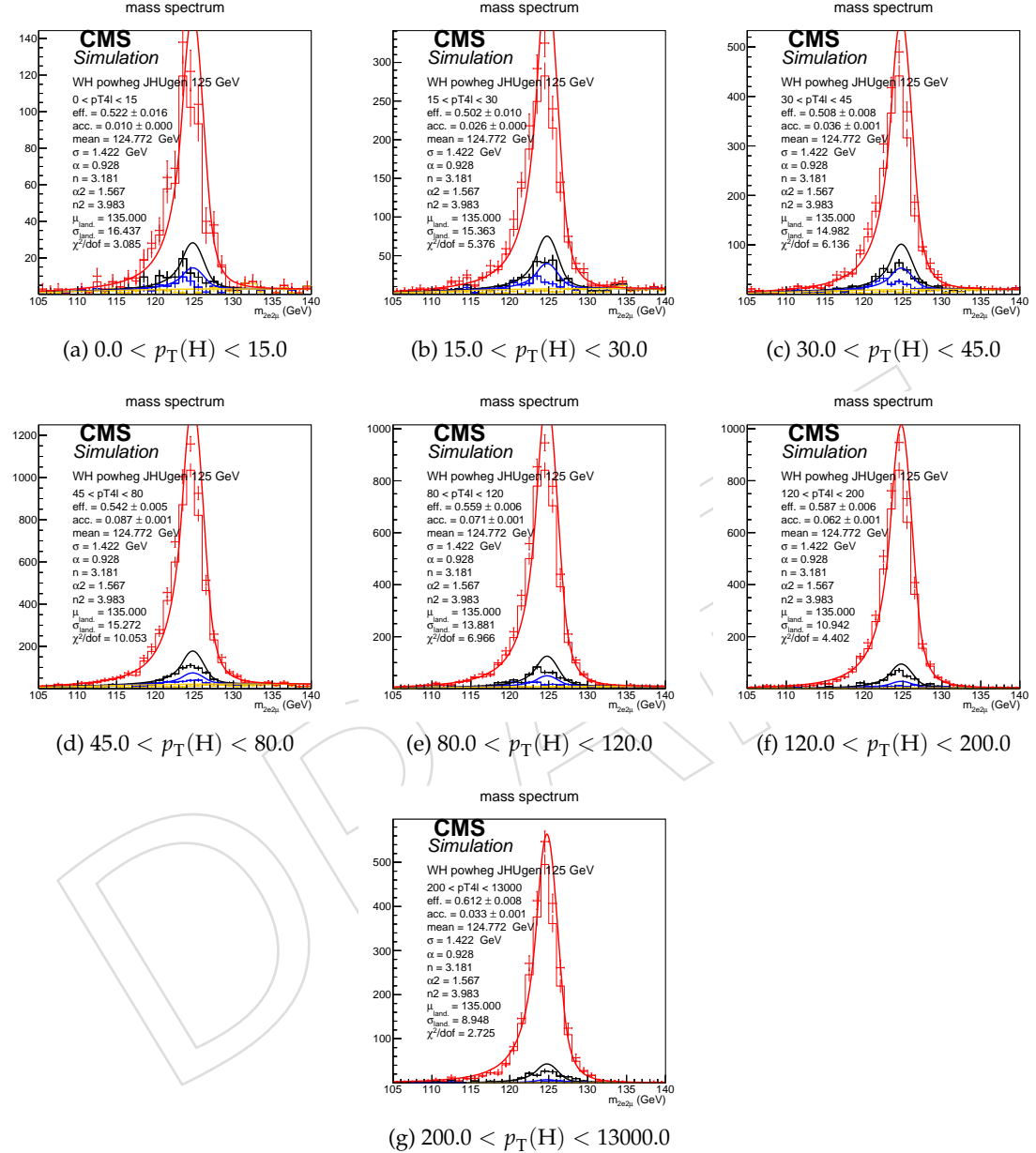


Figure 23: Example signal shapes at reconstruction level for a resonance of  $m(4\ell)$  in  $2e2\mu$  final state for the  $WH$  production mode from POWHEG+JHUGEN in different bins of  $p_T(H)$ . The black curve represents events which do not pass the fiducial volume selection. The curve has no effect on the result.

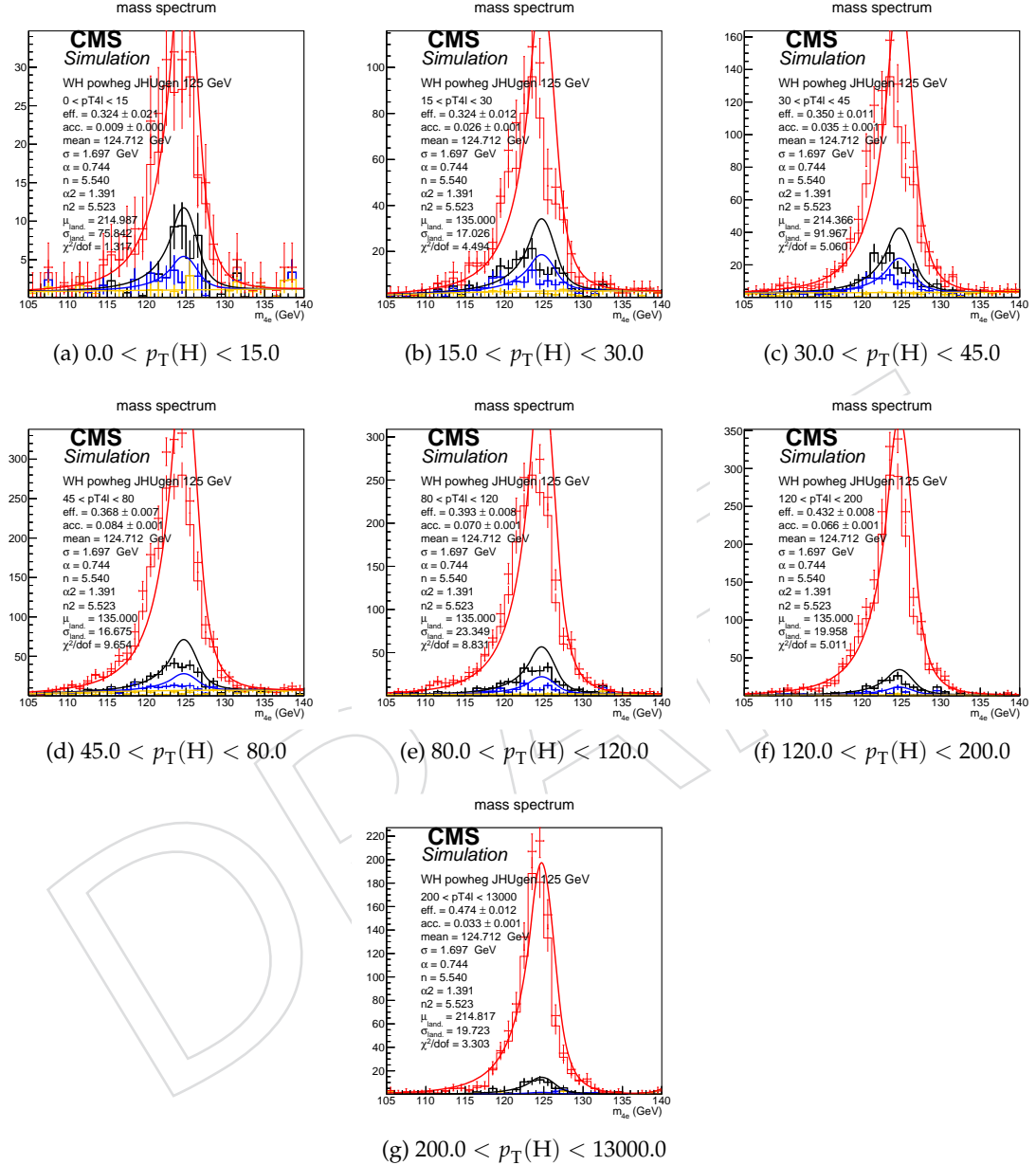


Figure 24: Example signal shapes at reconstruction level for a resonance of  $m(4\ell)$  in  $4e$  final state for the  $WH$  production mode from POWHEG+JHUGEN in different bins of  $p_{\text{T}}(\text{H})$ . The black curve represents events which do not pass the fiducial volume selection. The curve has no effect on the result.

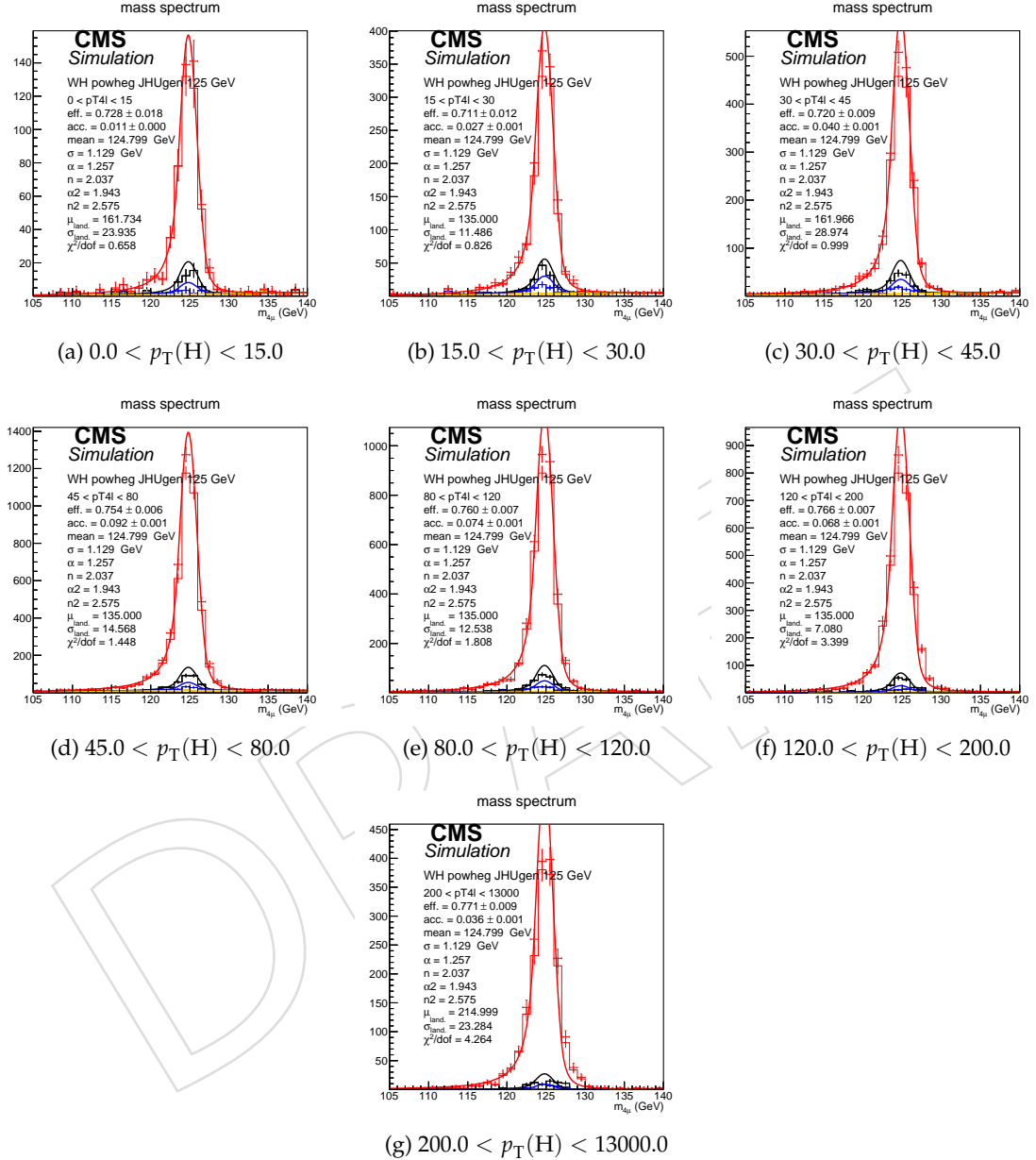


Figure 25: Example signal shapes at reconstruction level for a resonance of  $m(4\ell)$  in  $4\mu$  final state for the  $gg \rightarrow H$  production mode from POWHEG+JHUGEN in different bins of  $p_T(H)$ . The black curve represents events which do not pass the fiducial volume selection. The curve has no effect on the result.

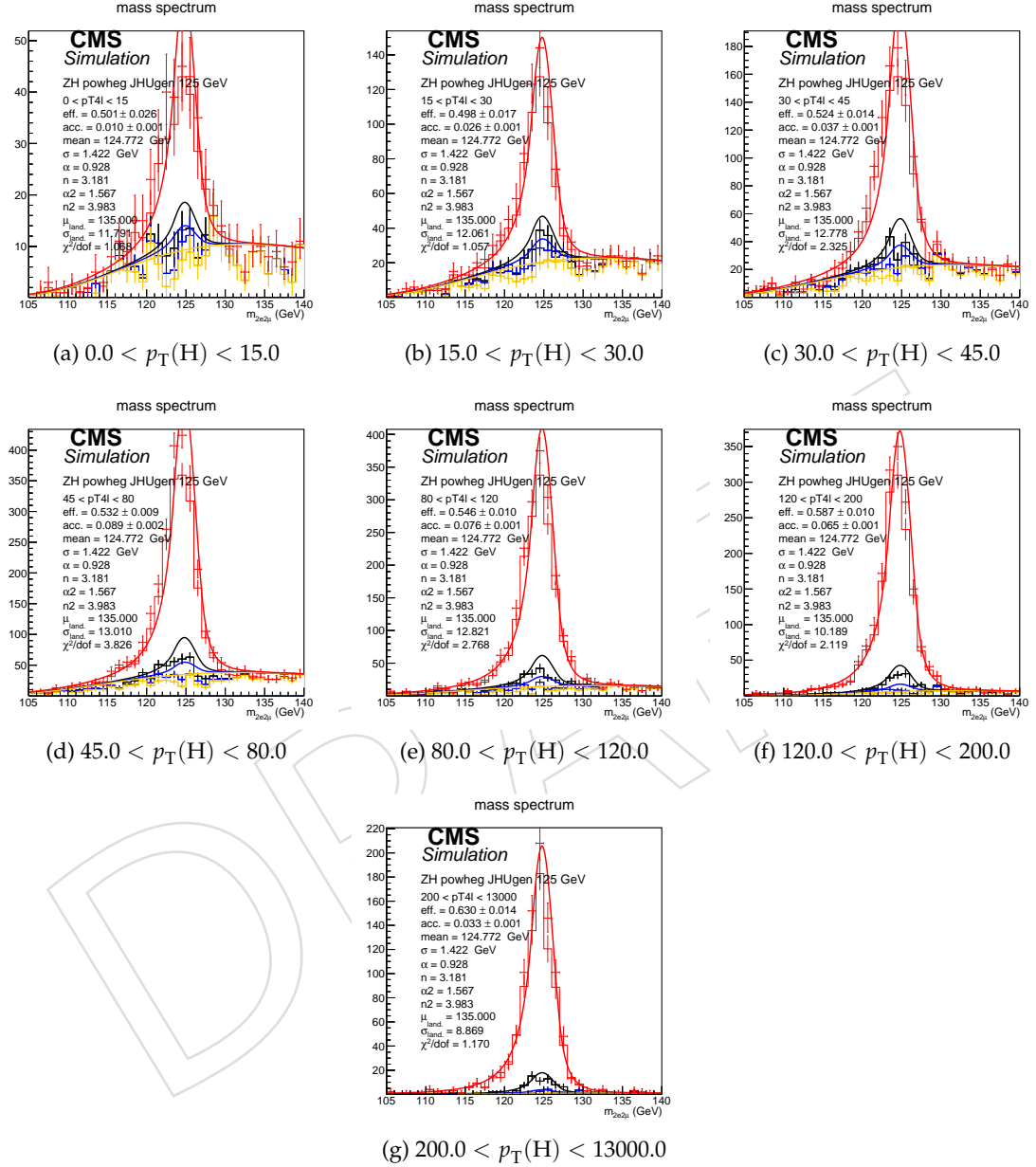


Figure 26: Example signal shapes at reconstruction level for a resonance of  $m(4\ell)$  in  $2e2\mu$  final state for the  $ZH$  production mode from POWHEG+JHUGEN in different bins of  $p_T(H)$ . The black curve represents events which do not pass the fiducial volume selection. The curve has no effect on the result.

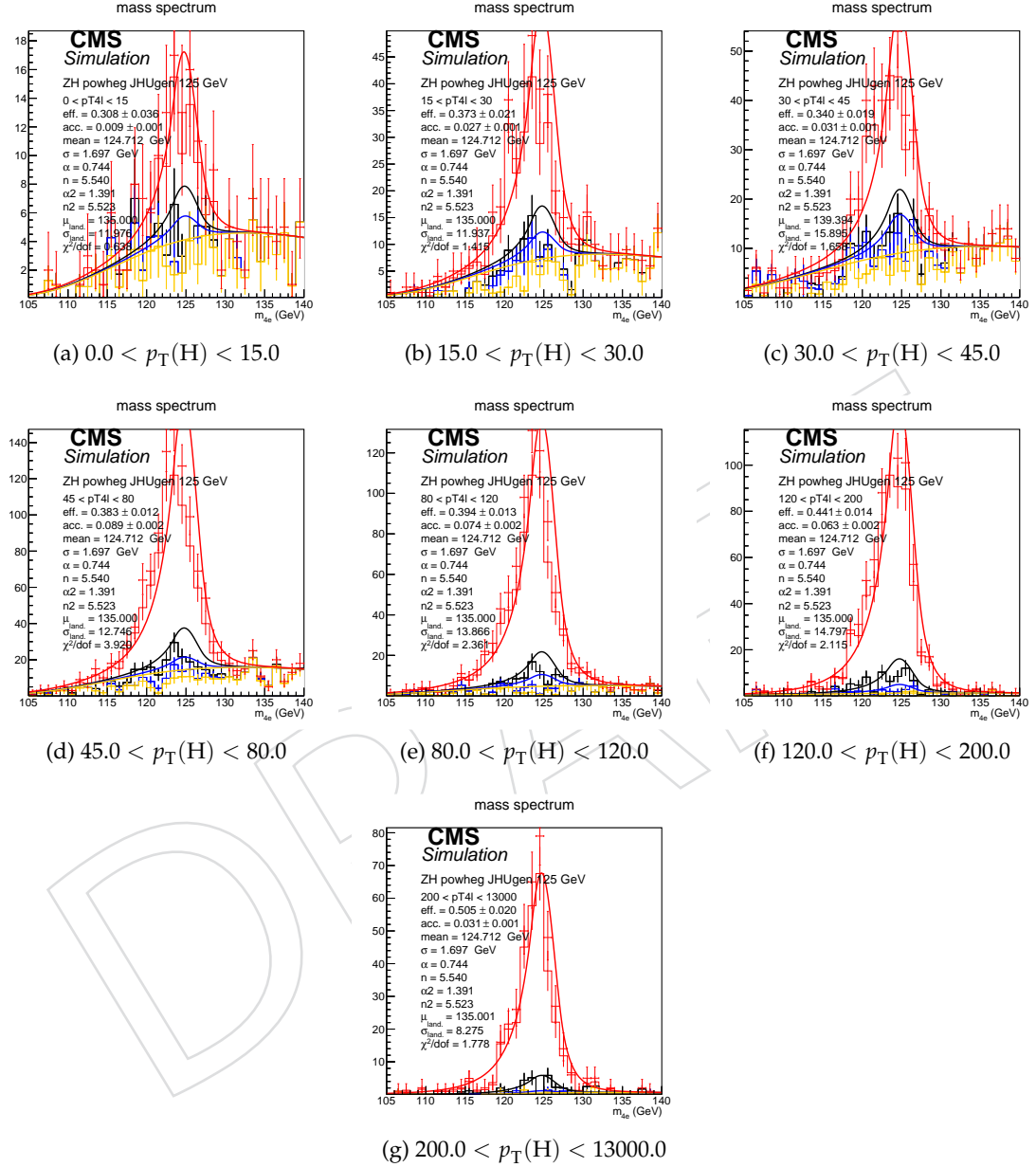


Figure 27: Example signal shapes at reconstruction level for a resonance of  $m(4\ell)$  in  $4e$  final state for the  $ZH$  production mode from POWHEG+JHUGEN in different bins of  $p_T(H)$ . The black curve represents events which do not pass the fiducial volume selection. The curve has no effect on the result.

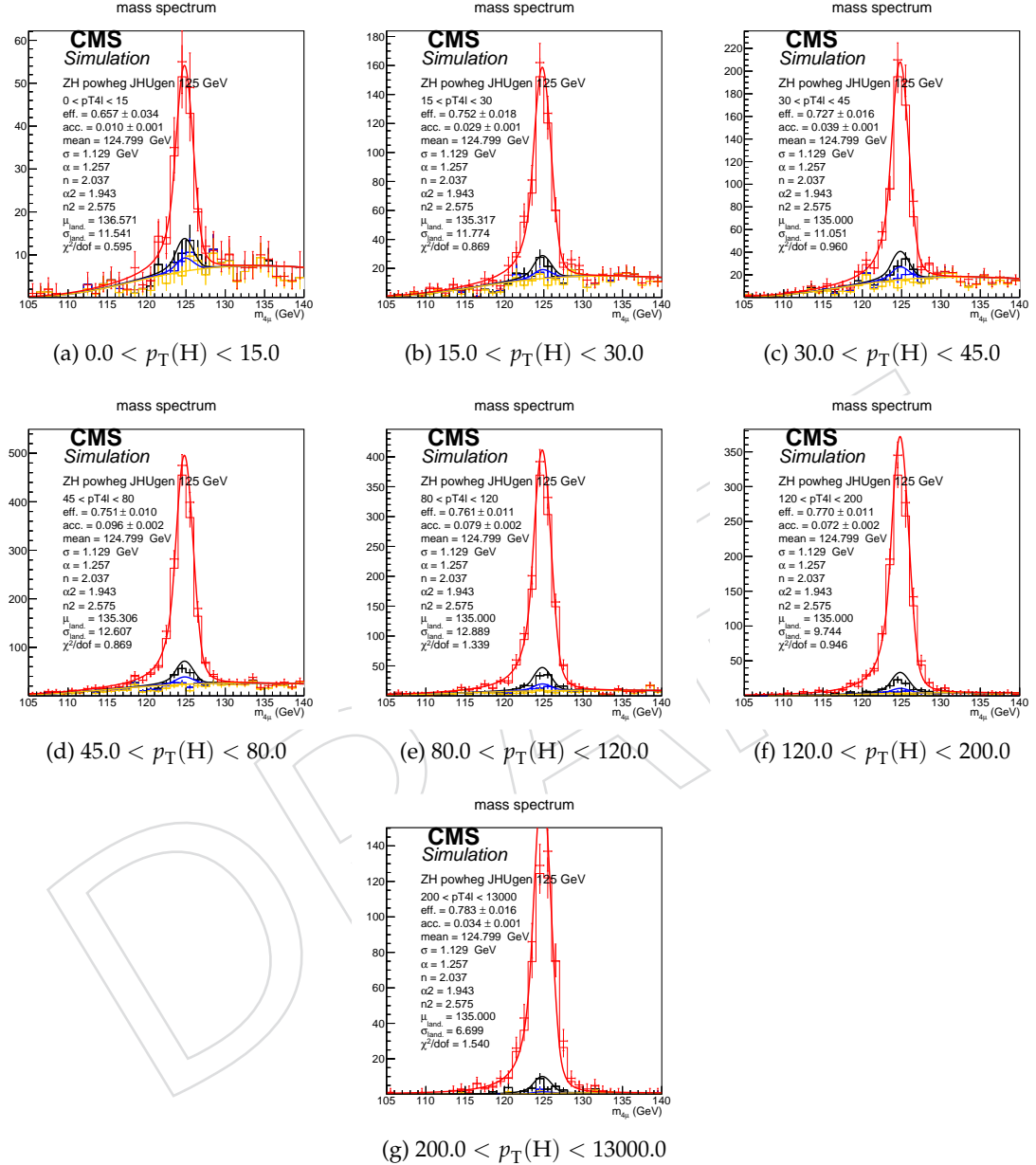


Figure 28: Example signal shapes at reconstruction level for a resonance of  $m(4\ell)$  in  $4\mu$  final state for the  $ZH$  production mode from POWHEG+JHUGEN in different bins of  $p_T(H)$ . The black curve represents events which do not pass the fiducial volume selection. The curve has no effect on the result.

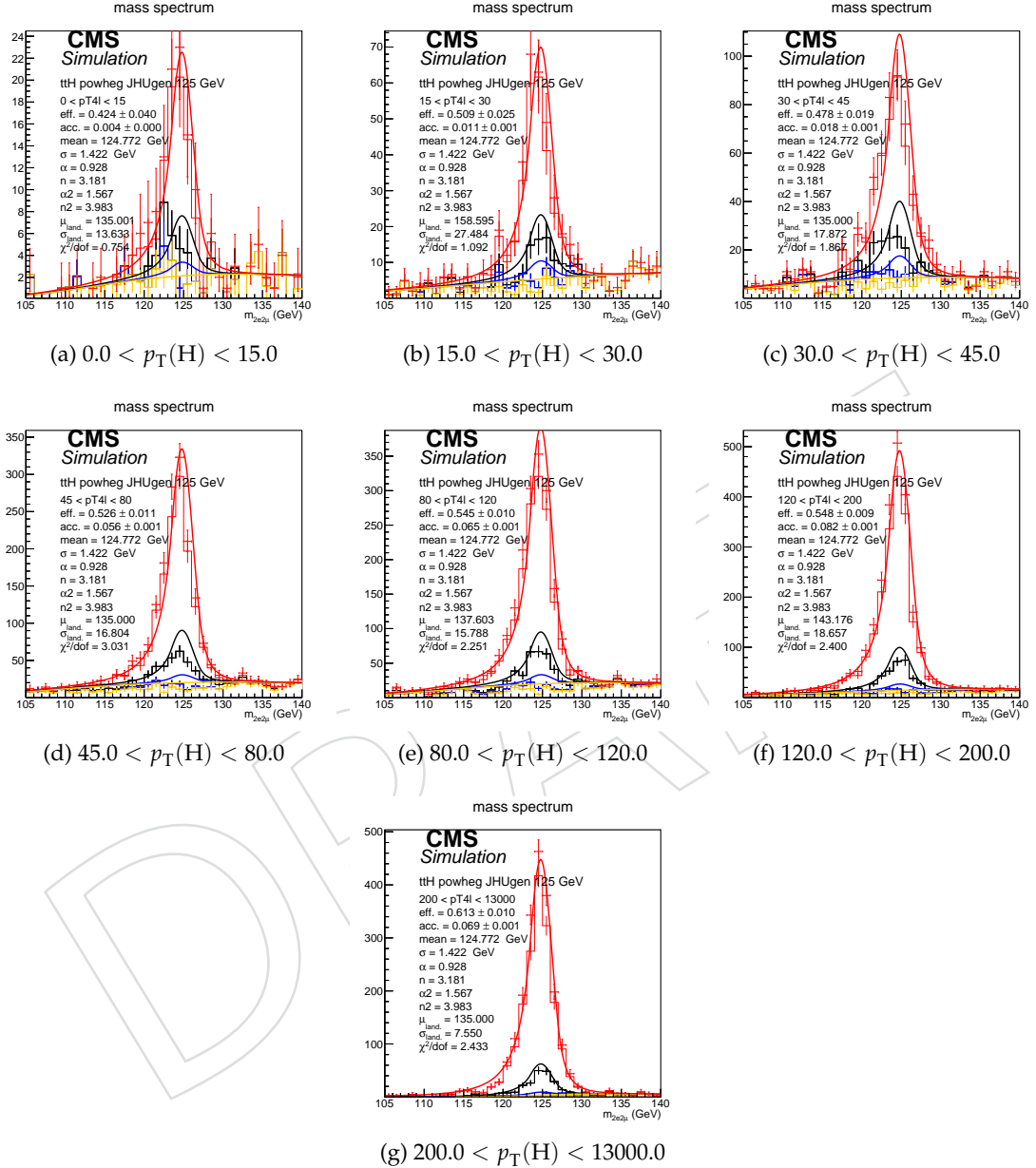


Figure 29: Example signal shapes at reconstruction level for a resonance of  $m(4\ell)$  in  $2e2\mu$  final state for the  $t\bar{t}H$  production mode from POWHEG+JHUGEN in different bins of  $p_T(H)$ . The black curve represents events which do not pass the fiducial volume selection. The curve has no effect on the result.

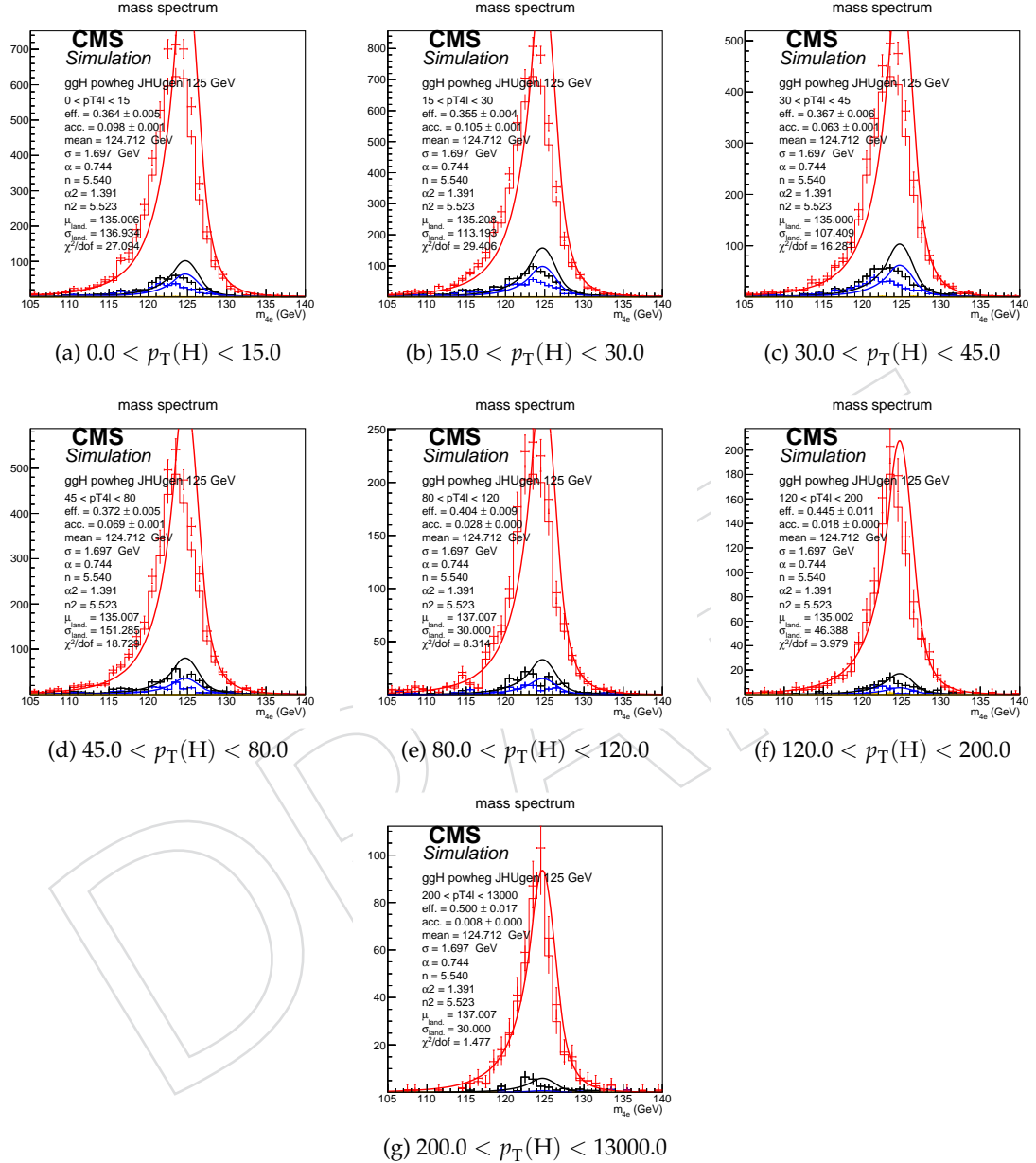


Figure 30: Example signal shapes at reconstruction level for a resonance of  $m(4\ell)$  in  $4e$  final state for the  $t\bar{t}H$  production mode from POWHEG+JHUGEN in different bins of  $p_T(H)$ . The black curve represents events which do not pass the fiducial volume selection. The curve has no effect on the result.

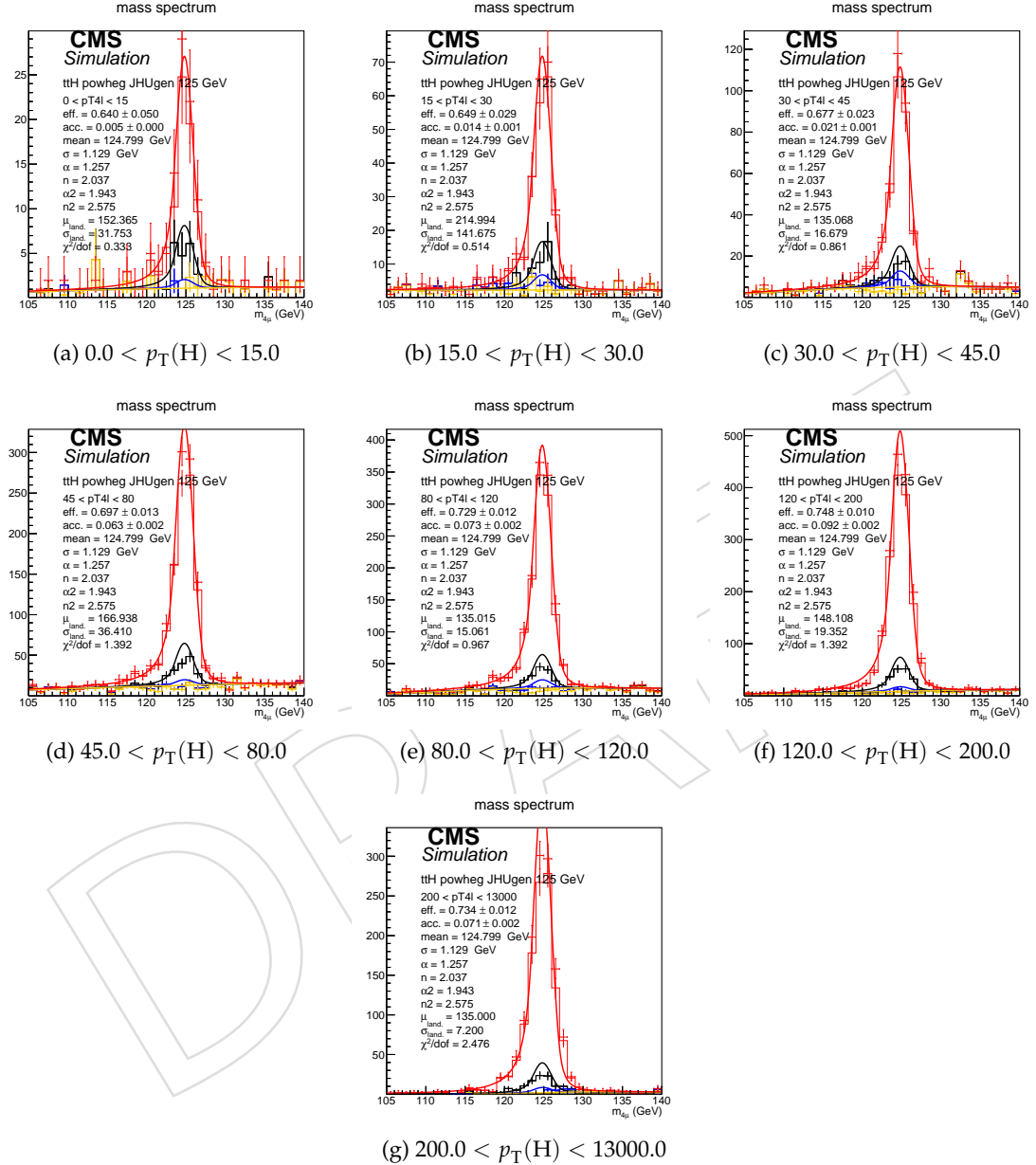


Figure 31: Example signal shapes at reconstruction level for a resonance of  $m(4\ell)$  in  $4\mu$  final state for the  $t\bar{t}H$  production mode from POWHEG+JHUGEN in different bins of  $p_{\text{T}}(\text{H})$ . The black curve represents events which do not pass the fiducial volume selection. The curve has no effect on the result.

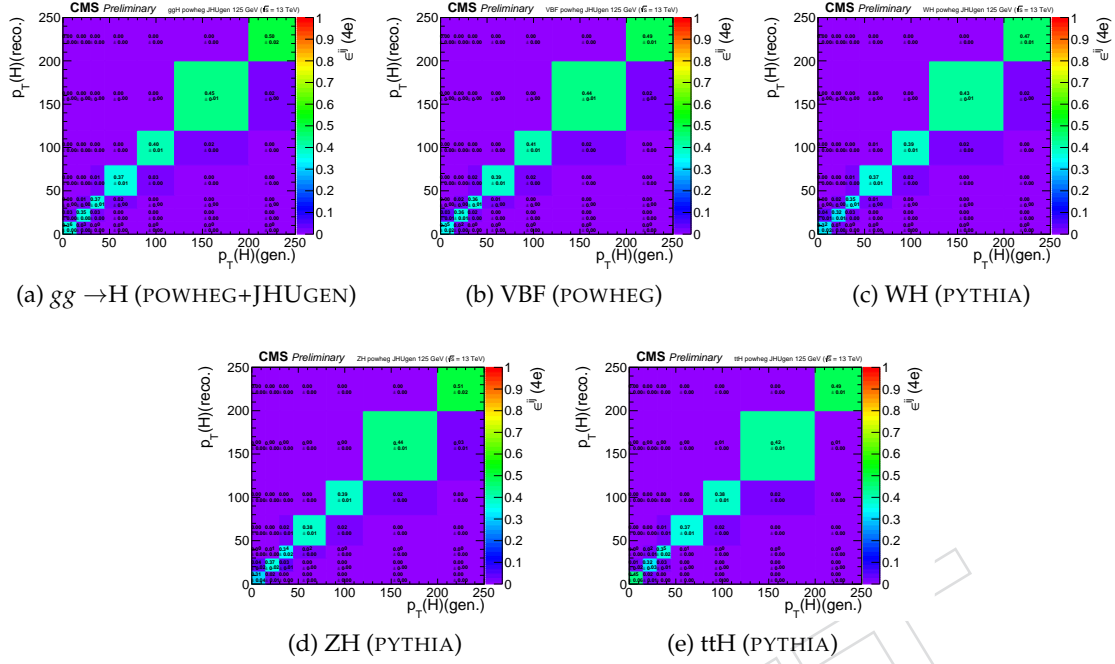


Figure 32: Efficiency matrices for  $p_T(H)$  for different SM production modes in the  $4e$  final state.

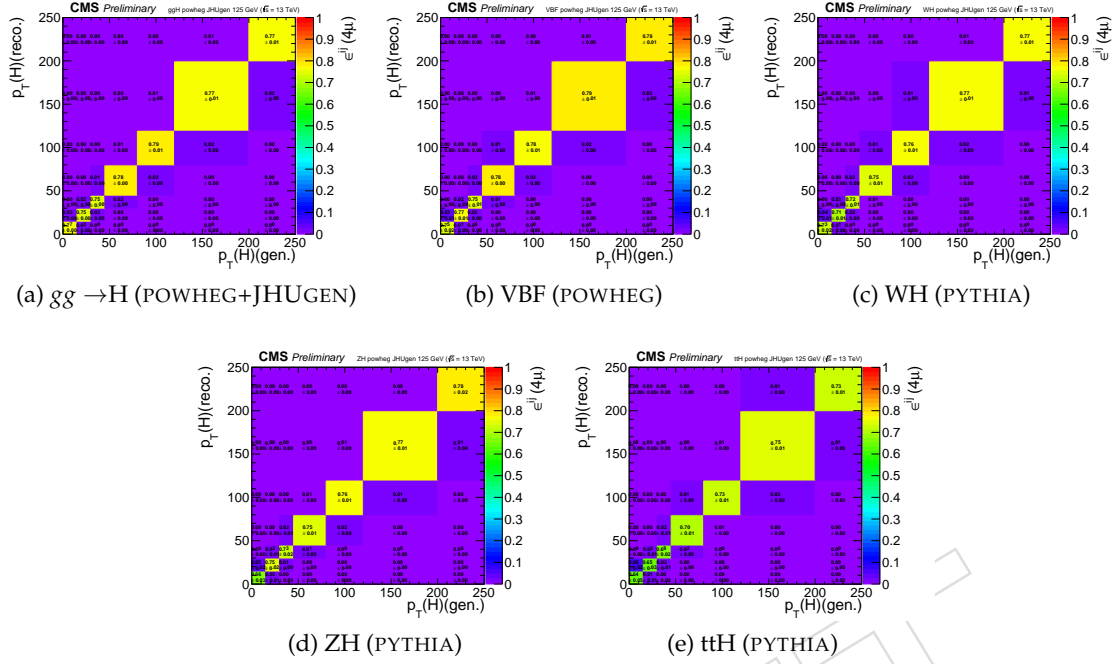


Figure 33: Efficiency matrices for  $p_T(H)$  for different SM production modes in the  $4\mu$  final state.

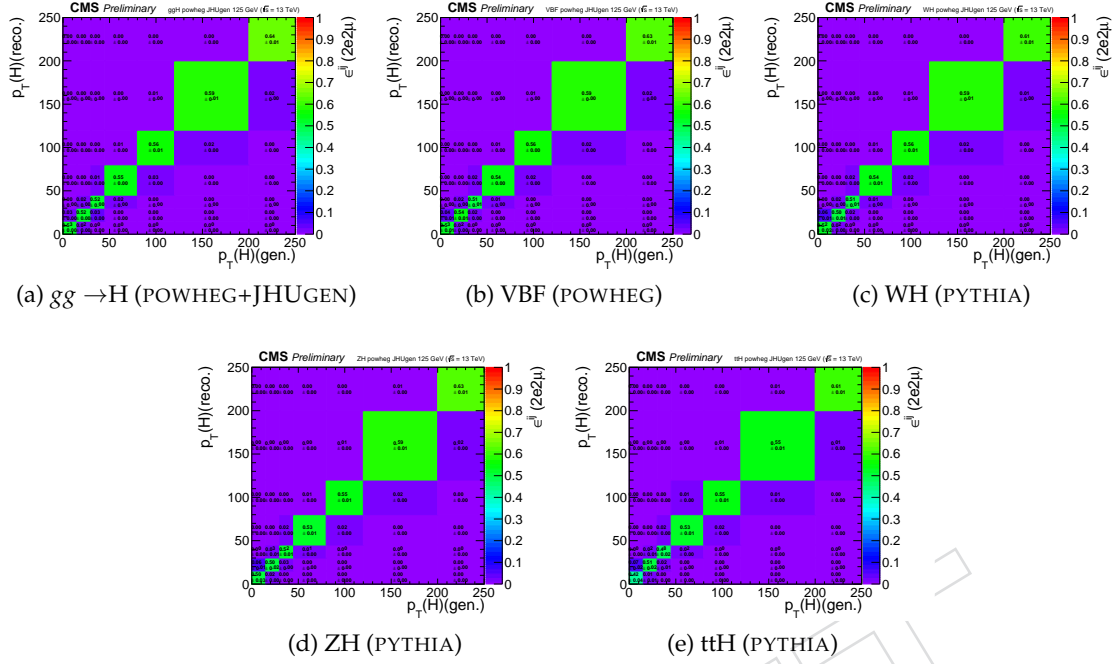
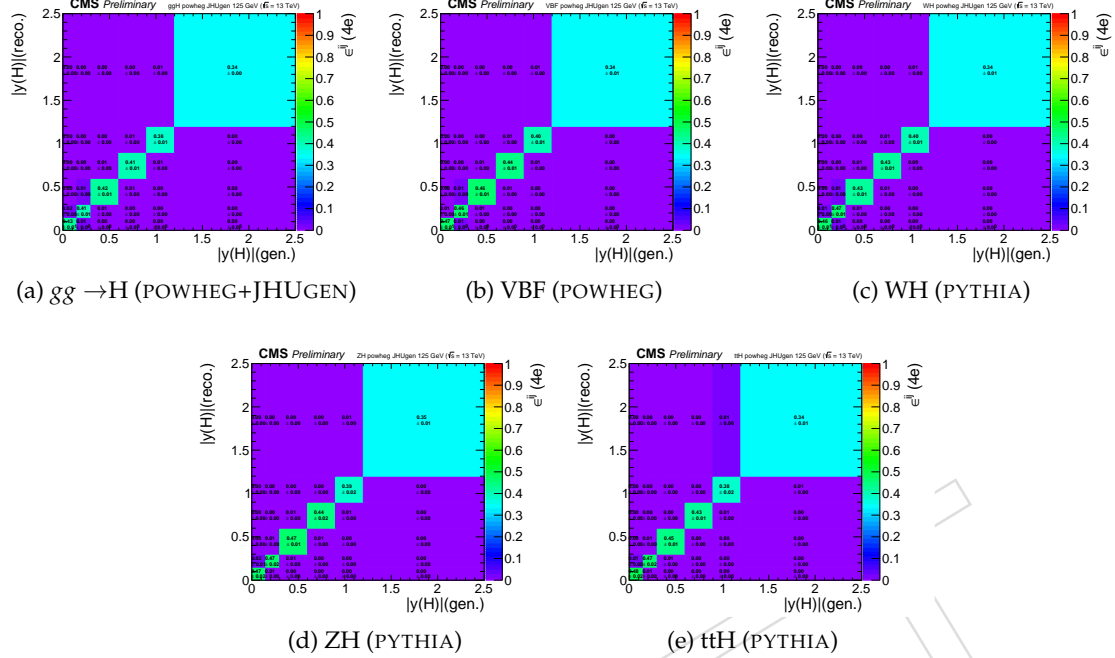


Figure 34: Efficiency matrices for  $p_T(H)$  for different SM production modes in the  $2e2\mu$  final state.

554 A.2 Signal inputs in different bins of  $|y(H)|$ Figure 35: Efficiency matrices for  $|y(H)|$  for different SM production modes in the  $4e$  final state.

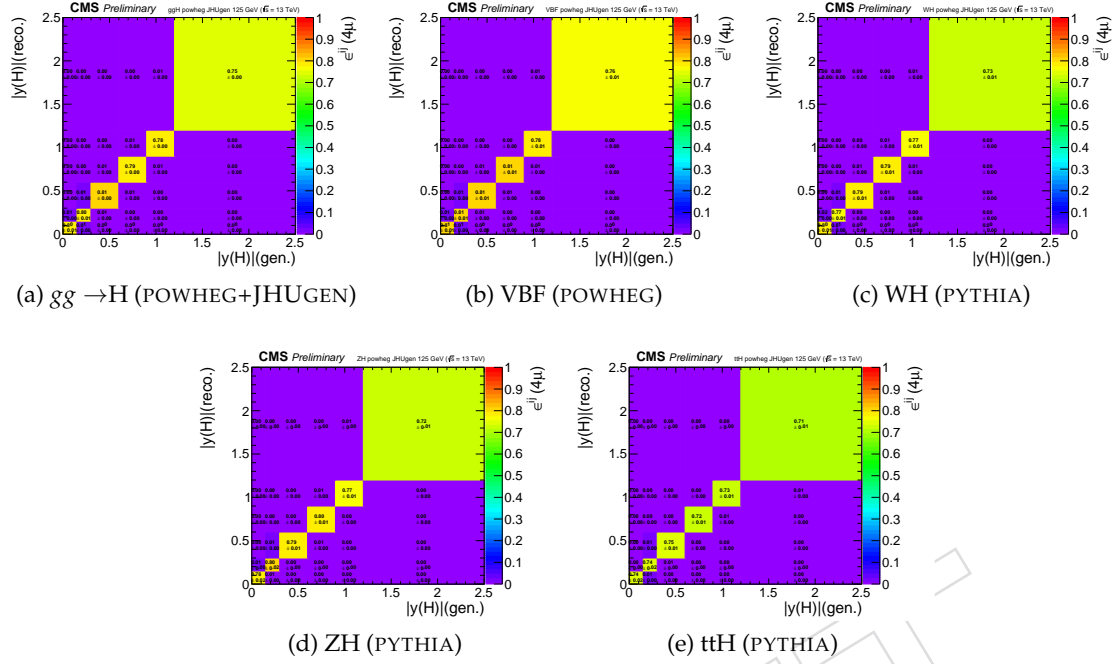


Figure 36: Efficiency matrices for  $|y(H)|$  for different SM production modes in the  $4\mu$  final state.

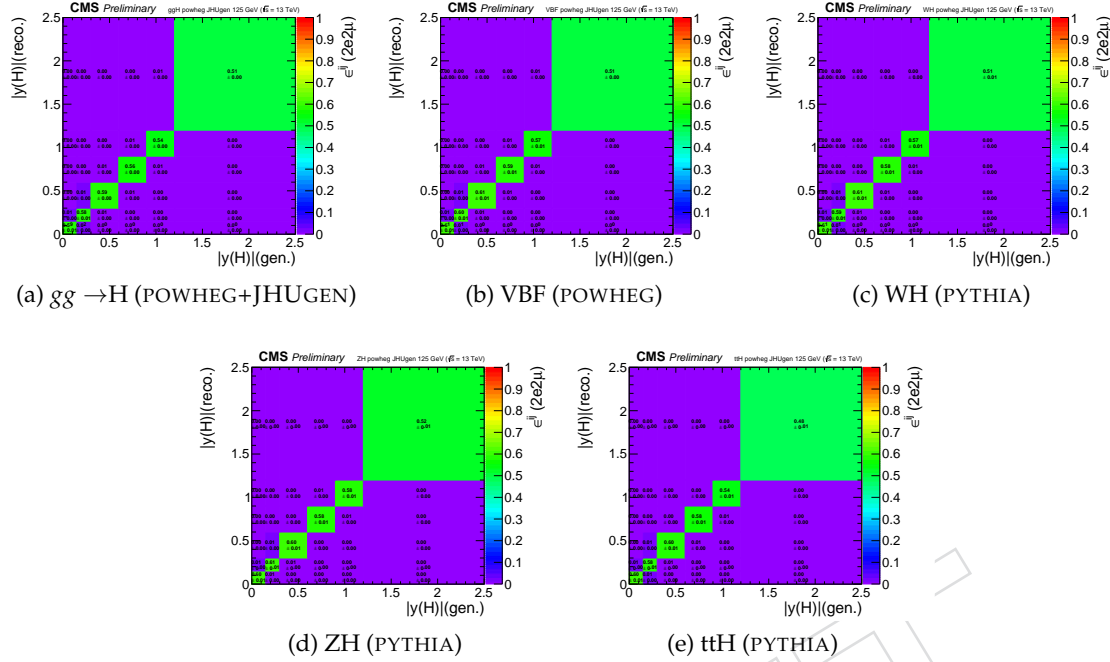


Figure 37: Efficiency matrices for  $|y(H)|$  for different SM production modes in the  $2e2\mu$  final state.

555 **A.3 Fits in different bins of N(jets)**

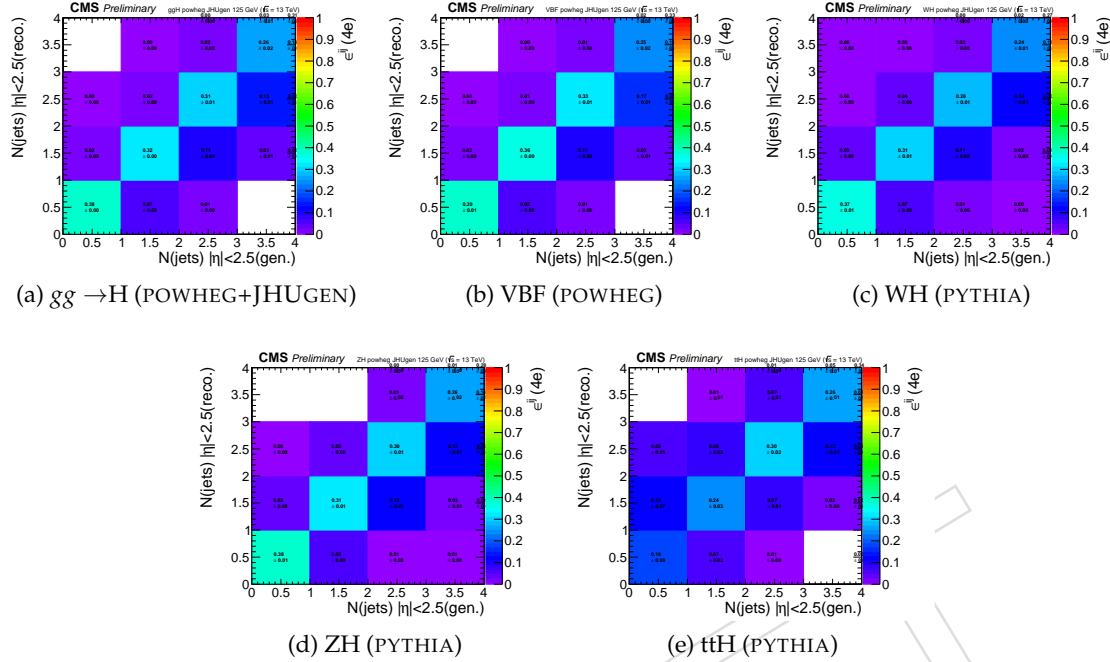


Figure 38: Efficiency matrices for  $N(\text{jets})$  for different SM production modes in the  $4e$  final state.

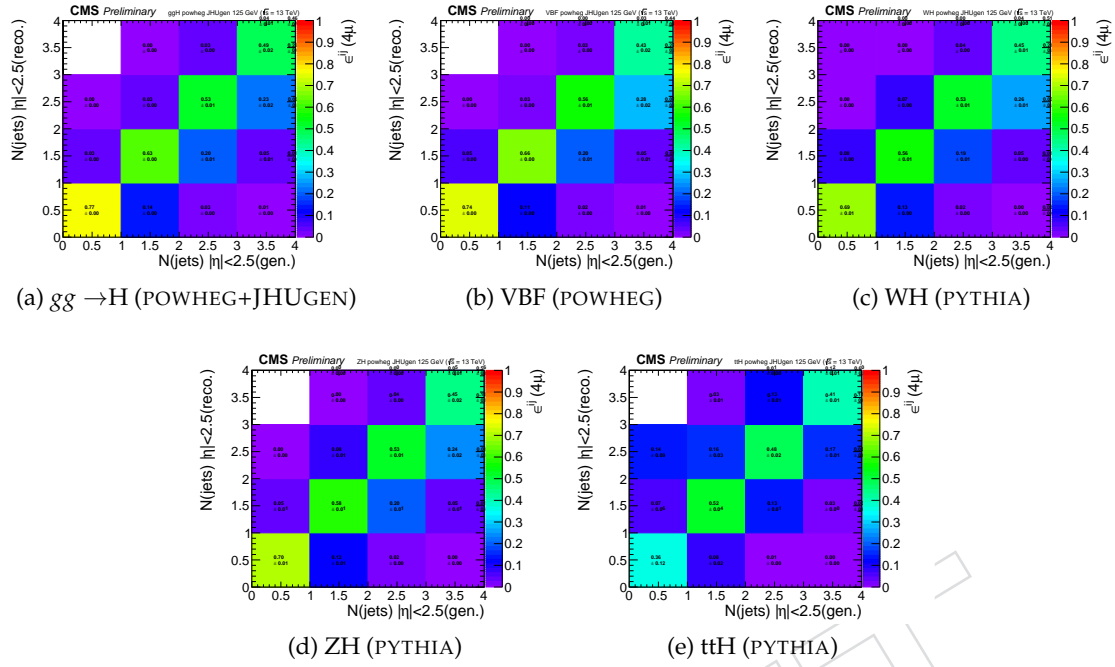


Figure 39: Efficiency matrices for  $N(\text{jets})$  for different SM production modes in the  $4\mu$  final state.

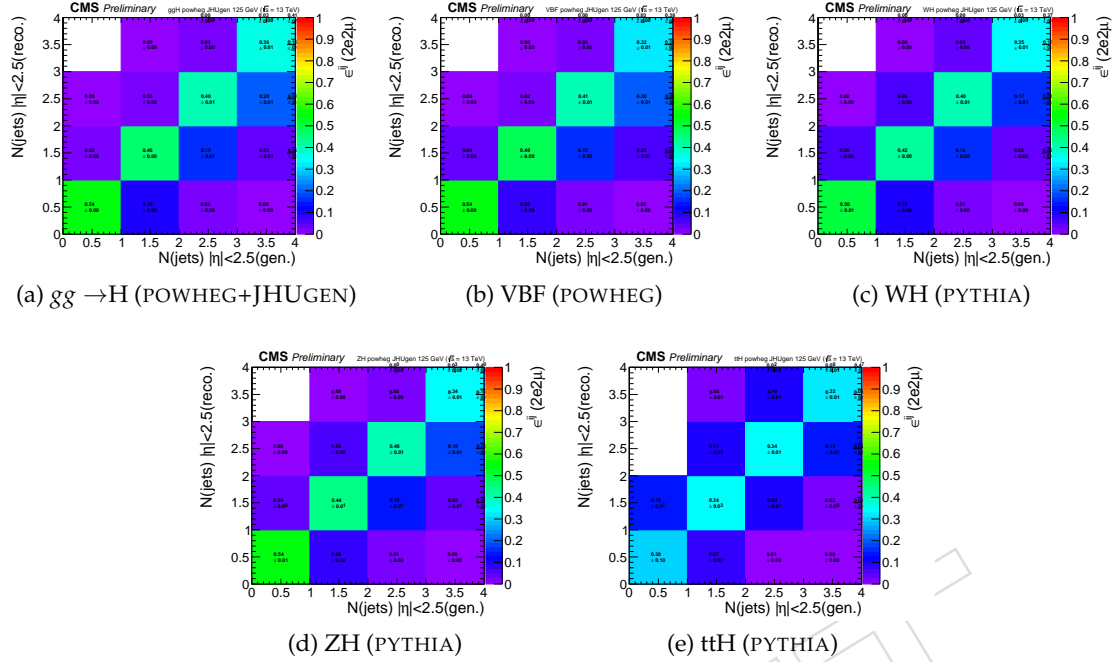


Figure 40: Efficiency matrices for  $N(\text{jets})$  for different SM production modes in the  $2e2\mu$  final state.

## 556 References

- 557 [1] CMS Collaboration, "Observation of a new boson at a mass of 125 GeV with the CMS  
558 experiment at the LHC", *Phys. Lett. B* **716** (2012) 30,  
559 doi:10.1016/j.physletb.2012.08.021, arXiv:1207.7235.
- 560 [2] ATLAS Collaboration, "Observation of a new particle in the search for the Standard  
561 Model Higgs boson with the ATLAS detector at the LHC", *Phys. Lett. B* **716** (2012) 1,  
562 doi:10.1016/j.physletb.2012.08.020, arXiv:1207.7214.
- 563 [3] F. Englert and R. Brout, "Broken Symmetry and the Mass of Gauge Vector Mesons",  
564 *Phys. Rev. Lett.* **13** (1964) 321, doi:10.1103/PhysRevLett.13.321.
- 565 [4] P. W. Higgs, "Broken symmetries, massless particles and gauge fields", *Phys. Lett.* **12**  
566 (1964) 132, doi:10.1016/0031-9163(64)91136-9.
- 567 [5] P. W. Higgs, "Broken Symmetries and the Masses of Gauge Bosons", *Phys. Rev. Lett.* **13**  
568 (1964) 508, doi:10.1103/PhysRevLett.13.508.
- 569 [6] G. Guralnik, C. Hagen, and T. Kibble, "Global Conservation Laws and Massless  
570 Particles", *Phys. Rev. Lett.* **13** (1964) 585, doi:10.1103/PhysRevLett.13.585.
- 571 [7] P. W. Higgs, "Spontaneous Symmetry Breakdown without Massless Bosons", *Phys. Rev.* **145**  
572 (1966) 1156, doi:10.1103/PhysRev.145.1156.
- 573 [8] T. Kibble, "Symmetry breaking in nonAbelian gauge theories", *Phys. Rev.* **155** (1967)  
574 1554, doi:10.1103/PhysRev.155.1554.
- 575 [9] CMS Collaboration, "Precise determination of the mass of the Higgs boson and tests of  
576 compatibility of its couplings with the standard model predictions using proton  
577 collisions at 7 and 8 TeV", *Eur. Phys. J. C* **75** (2015) 212,  
578 doi:10.1140/epjc/s10052-015-3351-7, arXiv:1412.8662.
- 579 [10] ATLAS Collaboration, "Measurements of the Higgs boson production and decay rates  
580 and coupling strengths using  $pp$  collision data at  $\sqrt{s} = 7$  and 8 TeV in the ATLAS  
581 experiment", *Eur. Phys. J. C* **76** (2016) doi:10.1140/epjc/s10052-015-3769-y,  
582 arXiv:1507.04548.
- 583 [11] ATLAS, CMS Collaboration, "Combined Measurement of the Higgs Boson Mass in  $pp$   
584 Collisions at  $\sqrt{s} = 7$  and 8 TeV with the ATLAS and CMS Experiments", *Phys. Rev. Lett.*  
585 **114** (2015) 191803, doi:10.1103/PhysRevLett.114.191803, arXiv:1503.07589.
- 586 [12] CMS Collaboration, "Measurements of the Higgs boson production and decay rates and  
587 constraints on its couplings from a combined ATLAS and CMS analysis of the LHC  $pp$   
588 collision data at  $\sqrt{s} = 7$  and 8 TeV", CMS Physics Analysis Summary  
589 CMS-PAS-HIG-15-002, 2015.
- 590 [13] CMS Collaboration, "Measurement of the properties of a Higgs boson in the four-lepton  
591 final state", *Phys. Rev. D* **89** (2014) 092007, doi:10.1103/PhysRevD.89.092007,  
592 arXiv:1312.5353.
- 593 [14] CMS Collaboration, "Study of the Mass and Spin-Parity of the Higgs Boson Candidate  
594 via Its Decays to Z Boson Pairs", *Phys. Rev. Lett.* **110** (2013) 081803,  
595 doi:10.1103/PhysRevLett.110.081803, arXiv:1212.6639.

- [596] [15] CMS Collaboration, “Constraints on the spin-parity and anomalous HVV couplings of  
 597 the Higgs boson in proton collisions at 7 and 8 TeV”, *Phys. Rev. D* **92** (2015) 012004,  
 598 doi:10.1103/PhysRevD.92.012004, arXiv:1411.3441.
- [599] [16] CMS Collaboration, “Constraints on the Higgs boson width from off-shell production  
 600 and decay to Z-boson pairs”, *Phys. Lett. B* **736** (2014) 64,  
 601 doi:10.1016/j.physletb.2014.06.077, arXiv:1405.3455.
- [602] [17] CMS Collaboration, “Limits on the Higgs boson lifetime and width from its decay to four  
 603 charged leptons”, *Phys. Rev. D* **92** (2015) 072010,  
 604 doi:10.1103/PhysRevD.92.072010, arXiv:1507.06656.
- [605] [18] CMS Collaboration, “Measurement of differential and integrated fiducial cross sections  
 606 for higgs boson production in the four-lepton decay channel in pp collisions at  $\sqrt{s} = 7$   
 607 and 8 tev”, arXiv:1512.08377.
- [608] [19] CMS Collaboration, “Measurements of properties of the higgs boson in the four-lepton  
 609 final state at  $\sqrt{s}=13$  tev with full run ii data”, CMS Physics Analysis Summary  
 610 CMS-PAS-HIG-19-001, 2019.
- [611] [20] I. Brivio, Y. Jiang, and M. Trott, “The SMEFTsim package, theory and tools”, *JHEP* **12**  
 612 (2017) 070, doi:10.1007/JHEP12(2017)070, arXiv:1709.06492.
- [613] [21] J. Aebischer et al., “WCxf: an exchange format for Wilson coefficients beyond the  
 614 Standard Model”, *Comput. Phys. Commun.* **232** (2018) 71–83,  
 615 doi:10.1016/j.cpc.2018.05.022, arXiv:1712.05298.
- [616] [22] S. Alioli, P. Nason, C. Oleari, and E. Re, “NLO vector-boson production matched with  
 617 shower in POWHEG”, *JHEP* **07** (2008) 060,  
 618 doi:10.1088/1126-6708/2008/07/060, arXiv:0805.4802.
- [619] [23] P. Nason, “A new method for combining NLO QCD with shower Monte Carlo  
 620 algorithms”, *JHEP* **11** (2004) 040, doi:10.1088/1126-6708/2004/11/040,  
 621 arXiv:hep-ph/0409146.
- [622] [24] S. Frixione, P. Nason, and C. Oleari, “Matching NLO QCD computations with parton  
 623 shower simulations: the POWHEG method”, *JHEP* **11** (2007) 070,  
 624 doi:10.1088/1126-6708/2007/11/070, arXiv:0709.2092.
- [625] [25] E. Bagnaschi, G. Degrassi, P. Slavich, and A. Vicini, “Higgs production via gluon fusion  
 626 in the POWHEG approach in the SM and in the MSSM”, *JHEP* **02** (2012) 088,  
 627 doi:10.1007/JHEP02(2012)088, arXiv:1111.2854.
- [628] [26] P. Nason and C. Oleari, “NLO Higgs boson production via vector-boson fusion matched  
 629 with shower in POWHEG”, *JHEP* **02** (2010) 037, doi:10.1007/JHEP02(2010)037,  
 630 arXiv:0911.5299.
- [631] [27] H. B. Hartanto, B. Jager, L. Reina, and D. Wackerlo, “Higgs boson production in  
 632 association with top quarks in the POWHEG BOX”, *Phys. Rev. D* **91** (2015), no. 9, 094003,  
 633 doi:10.1103/PhysRevD.91.094003, arXiv:1501.04498.
- [634] [28] K. Hamilton, P. Nason, E. Re, and G. Zanderighi, “NNLOPS simulation of Higgs boson  
 635 production”, *JHEP* **10** (2013) 222, doi:10.1007/JHEP10(2013)222,  
 636 arXiv:1309.0017.

- [29] G. Luisoni, P. Nason, C. Oleari, and F. Tramontano, “ $HW^\pm/\text{HZ} + 0$  and 1 jet at NLO with the POWHEG BOX interfaced to GoSam and their merging within MiNLO”, *JHEP* **10** (2013) 083, doi:10.1007/JHEP10(2013)083, arXiv:1306.2542.
- [30] Y. Gao et al., “Spin determination of single-produced resonances at hadron colliders”, *Phys. Rev. D* **81** (2010) 075022, doi:10.1103/PhysRevD.81.075022, arXiv:1001.3396. [Erratum: doi:10.1103/PhysRevD.81.079905].
- [31] NNPDF Collaboration, “Parton distributions for the LHC Run II”, *JHEP* **04** (2015) 040, doi:10.1007/JHEP04(2015)040, arXiv:1410.8849.
- [32] P. Nason and G. Zanderighi, “ $W^+W^-$ ,  $WZ$  and  $ZZ$  production in the POWHEG-BOX-V2”, *Eur. Phys. J.* **C74** (2014), no. 1, 2702, doi:10.1140/epjc/s10052-013-2702-5, arXiv:1311.1365.
- [33] J. M. Campbell and R. K. Ellis, “MCFM for the Tevatron and the LHC”, *Nucl. Phys. Proc. Suppl.* **205** (2010) 10, doi:10.1016/j.nuclphysbps.2010.08.011, arXiv:1007.3492.
- [34] J. M. Campbell, R. K. Ellis, and C. Williams, “Bounding the Higgs width at the LHC using full analytic results for  $gg \rightarrow e^-e^+\mu^-\mu^+$ ”, *JHEP* **04** (2014) 060, doi:10.1007/JHEP04(2014)060, arXiv:1311.3589.
- [35] J. Alwall et al., “The automated computation of tree-level and next-to-leading order differential cross sections, and their matching to parton shower simulations”, *JHEP* **07** (2014) 079, doi:10.1007/JHEP07(2014)079, arXiv:1405.0301.
- [36] CMS Collaboration, “Measurements of properties of the higgs boson in the four-lepton final state in proton-proton collisions at  $\sqrt{s} = 13$  TeV”, *CMS-PAS-HIG-19-001* (2019).
- [37] CMS Collaboration, “Measurement of the properties of the Higgs boson in the four-lepton final state at  $\sqrt{s} = 13$  TeV”, CMS Physics Analysis Note CMS-AN-15-277, 2016.
- [38] CMS Collaboration, “Measurement of the properties of the higgs boson in the four-lepton final state at  $\sqrt{s} = 13$  tev”, CMS Physics Analysis Note CMS-AN-15-277, 2016.
- [39] CMS Collaboration, “Measurement of differential cross sections for Higgs boson production in the diphoton decay channel in pp collisions at  $\sqrt{s}=8$  TeV”, *Eur. Phys. J. C* **76** (2015) 13, doi:10.1140/epjc/s10052-015-3853-3, arXiv:1508.07819.
- [40] ATLAS and CMS Collaborations, LHC Higgs Combination Group, “Procedure for the lhc higgs boson search combination in summer 2011”, ATL-PHYS-PUB/CMS NOTE 2011-11, 2011/005, CERN, 2011.
- [41] G. Cowan, K. Cranmer, E. Gross, and O. Vitells, “Asymptotic formulae for likelihood-based tests of new physics”, *Eur. Phys. J. C* **71** (2011) 1554, doi:10.1140/epjc/s10052-011-1554-0, 10.1140/epjc/s10052-013-2501-z, arXiv:1007.1727.